

Thomas Ganner, BSc

Enzymatic cellulose degradation via atomic force microscopy in liquid environments

MASTER THESIS

For obtaining the academic degree
Diplom-Ingenieur

Master Programme of
Technical Physics



Graz University of Technology

Supervisor:

Ao.-Univ.-Prof. Dipl.-Ing. Dr. techn. Gerald Kothleitner

Co-supervisor:

Dipl.-Ing. Dr. techn. Harald Plank

Institute for Electron Microscopy and Fine Structure Research

Graz, May 2012

Deutsche Fassung:
Beschluss der Curricula-Kommission für Bachelor-, Master- und Diplomstudien vom 10.11.2008
Genehmigung des Senates am 1.12.2008

EIDESSTÄTTLICHE ERKLÄRUNG

Ich erkläre an Eides statt, dass ich die vorliegende Arbeit selbstständig verfasst, andere als die angegebenen Quellen/Hilfsmittel nicht benutzt, und die den benutzten Quellen wörtlich und inhaltlich entnommene Stellen als solche kenntlich gemacht habe.

Graz, am

.....
(Unterschrift)

Englische Fassung:

STATUTORY DECLARATION

I declare that I have authored this thesis independently, that I have not used other than the declared sources / resources, and that I have explicitly marked all material which has been quoted either literally or by content from the used sources.

.....
date

.....
(signature)

Abstract

Fuels from biological feedstock may play an important role and be a crucial factor on our way to a better handling of our climate and earth. The aim today lays on Second Generation biofuels, fabricated from biological non-food feedstock from grass or wood. Until now great progress has been made on this wide and highly interesting field by identifying and characterizing several microorganisms capable of digesting cellulose by the use of so called cellulases. These cellulases are proteins and they can be seen as small chemical machines, using a catalytic core to hydrolyze cellulose in the presence of water. In this thesis we aim our view on exactly this process of hydrolysis by a cellulase system of the fungus *Trichoderma Reesei*. We will use the technique of liquid environment Atomic Force Microscopy (AFM) to investigate this highly complex process on a novel substrate. The substrate is a special combination of cellulosic material in different allomorphs, where the most content is of crystalline cellulose II allomorph embedded in amorphous cellulosic material. Natural cellulose resources often show crystalline cellulose embedded in amorphous material which makes our substrate the ideal candidate for investigations of enzymatic hydrolysis. A special enzyme solution from *Trichoderma Reesei* with two exo-1,4- β -glucanase or cellobiohydrolases (CBH 1 and CBH 2) as well as a endo-1,4- β -glucosidase or endoglucanase (EG 1) is used for this study. It is well known in literature that these ([1], [2]) enzymes show strong cooperative action among each other also referred as synergism. This synergism can be explained in the following way: the sum of single enzyme activity cannot compete with the combined activity at the same concentration. We will show that this effect has a striking effect on the hydrolysis rate and we are going to identify the roles of the individual enzymes in this constellation. Novel results are presented in this thesis on the hydrolysis activity of CBH 2 which will lead to a new understanding of this type of enzyme. The term exo-glucanase for the enzyme CBH 2 should be reconsidered after the results obtained in this thesis. For new measurements a special procedure will be designed, with the construction of a special liquid cell as well as a heating aperture for sample heating. The designs are optimized on our requirements for this experiment and will serve as basis for future investigations. This work is based on the work of Judith Dohr (2011) [3] where the basic principle of the cellulase action was investigated by conventional AFM techniques in ambient conditions.

Kurzfassung

Kraftstoffe aus biologischen Abfällen könnten für die Zukunft des Menschen und des Klimas der Erde von großer Bedeutung sein. Diese sogenannten Second Generation Biokraftstoffe werden nicht aus Nahrungsmittelpflanzen gewonnen, sondern vielmehr aus Holz, Gras und anderen Zellulose beinhaltenden Abfällen. Bis heute konnte ein bemerkenswerter Fortschritt auf dem Weg zur effizienten Herstellung dieser Kraftstoffe erzielt werden, indem eine Vielzahl von Mikroorganismen identifiziert und charakterisiert wurde. Diese wandeln mit so genannten Zellulasen Zellulose in Zucker um und nutzen diesen als Energiequelle. Zellulasen sind Proteine und können als chemische Mikromaschinen angesehen werden, die mit der Hilfe eines katalytischen Mechanismus die Zellulose in Gegenwart von Wasser hydrolisieren. In dieser Arbeit werden genau diese Prozesse anhand eines Zellulase-Systems des Bodenpilzes *Trichoderma Reesei* untersucht. Wir werden zeigen, dass die Methode und Technik der Rasterkraftmikroskopie in flüssiger Umgebung für diese Untersuchungen geeignet ist um diesen hochkomplexen Vorgang auf molekularer Ebene zu analysieren. Um den Anforderungen der Rasterkraftmikroskopie gerecht zu werden, wird von uns ein neuartiges Substrat vorgestellt mit folgender Zusammensetzung: nano-kristalline Cellulose des Typs 2 ist in einer Matrix aus amorpher Zellulose eingebettet. Dies ist charakteristisch für natürliche Zellulose die als Bestandteil von Zellwänden in Pflanzenzellen genau diesen amorph/kristallin Aufbau zeigt. Daher ist dieses Substrat ideal geeignet für die in dieser Arbeit vorgestellten Untersuchungen. Für diese Experimente wird eine spezielle Lösung aus Zellulasen verwendet, bestehend aus zwei kristallin-affinen exo-Zellulasen (auch Cellobiohydrolases CBH 1/2) und einer amorph-affinen endo-Zellulase oder auch Endoglucanase (EG 1). Es ist seit langem bekannt ([1], [2]), dass Zellulasesysteme starke kooperative Aktivitätsmuster zeigen, auch Synergie genannt. Dies ist damit zu erklären, dass die Einzelaktivität verschiedener Enzyme bei weitem nicht an die Aktivität im Verbund heran reicht. Wir werden zeigen, dass dies von größter Wichtigkeit für eine effiziente Hydrolyse von Zellulose ist. Die Rollen der verschiedenen Einzelenzyme in diesem System werden von uns analysiert und identifiziert werden. Neue Resultate in Bezug auf das Enzym CBH 2 werden präsentiert werden und eine Überprüfung des Terms exo-glucanase (den Ketten entlang wanderndes Enzym) nötig machen. Für diese neuartigen Messungen wird ein neues strategisches Konzept sowie ein mechanisches Design für eine Liquid-cell mit eingebauter Temperaturkontrolle vorgestellt. Die Designs sind für dieses Experiment optimiert und sollen als Ausgangspunkt für neuartige Messverfahren in der Zukunft dienen. Die Arbeit basiert auf den Untersuchungen von [3] wo die grundsätzliche Funktion des Zelluloseabbaus mit Hilfe von konventioneller Rasterkraftmikroskopie (an Luft) vorgestellt wurde.

Acknowledgment

A thesis like this wouldn't be possible without the help of several people and colleagues. I herein want to give my acknowledgments to the people who supported me and helped me with this thesis. First of all I want to thank Dr. Harald Plank for his kind support and his help during all appearing problems, may they be of technical or personal nature. Gratitude is owed to my supervisor Dr. Gerald Kothleitner for his support and supervision of this thesis as well for his open door for all kind of problems. To Claudia Mayerhofer I owe special thanks for her work with the substrate preparation and her kind and helping nature. Gratitude is owned to Gerhard Birnstingel and Markus Sittsam, which did great work on the fabrication of the different mechanical parts and offered there help whenever needed. Special thanks have to be given to the Center of Electron Microscopy and the Head of the Institute Dr. Ferdinand Hofer for the financial support during my work. Further acknowledgments have to be given to the whole Felmi-ZFE staff for a great working environment and team spirit. Special thanks have to be dedicated to my colleagues Manuel Eibinger and Patricia Bubner for helping me during the experiments. I owe special thanks to Bernd Nidetzky as the head of the biotechnology institute for fruitful discussions and the possibility to work in a pleasant team atmosphere.

This thesis is the result of a 6 year long academic study and wouldn't be possible without the help and support from family and friends. Gratitude has to be given to my parents Peter Paul and Margarethe, for their financial support to study freely without any thoughts about my financial situation. They have always supported me and I am proud to be their son. I also want to thank my sister and brother who are very important to me and have always supported me when needed. I also want to thank all my friends for their kind company during this time. Most of all I want to thank my girlfriend Verena which was my personal and mental backup during my study. She helped me through tough times and was always there for me, nevertheless, which problem appeared. For this reason I want to dedicate this work to her and our relationship. May it stay this way for the rest of our lives.

Table of Contents

1	Introduction	1
2	Fundamentals.....	3
2.1	Biology and Chemistry.....	3
2.1.1	Cellulose.....	3
2.1.1.1	Structure	3
2.1.1.2	Physiological Function	5
2.1.2	Cellulases	5
2.1.2.1	Cellobiohydrolase 1 (CBH 1).....	6
2.1.2.2	Cellobiohydrolase 2 (CBH 2).....	7
2.1.2.3	Endoglucanase (EG)	7
2.1.2.4	Hydrolysis.....	8
2.1.3	Ionic Liquids (IL).....	10
2.2	The Atomic Force Microscope (AFM).....	11
2.2.1	Components.....	12
2.2.1.1	Tip-Cantilever System	12
2.2.1.2	Detection System	13
2.2.1.3	Motion System	14
2.2.1.4	Feedback Loop and Image Processing Unit.....	15
2.2.2	Contact Mode AFM	15
2.2.3	Tapping and Phase Mode AFM	16
2.2.4	Nanoscale Forces.....	18
2.2.5	Theoretical Description of AM-AFM.....	20
2.2.5.1	The Point-Mass Model Described by a Harmonic Oscillator.....	21
2.2.6	The AM-AFM in Liquid Environments.....	23
2.3	Ultramicrotomy	25
3	Experimental Concept & Requirements	27
4	Designs & Problem Solutions	28
4.1	Mechanics.....	28

4.1.1	Sample Holder.....	28
4.1.2	Fixation for Ultramicrotomy	29
4.1.3	Liquid Cell.....	30
4.1.4	Temperature Unit & Stage Fixation.....	31
4.1.5	Complete Setup.....	32
4.2	Electronics	33
4.2.1	Requirements & Specifications	33
4.2.2	Controller Board.....	34
4.2.2.1	LoC Amplifier	35
4.2.2.2	Microprocessor Unit.....	36
4.2.2.3	HC Amplifier	37
4.3	Software	38
4.3.1	Main Program	38
4.3.2	Menu	39
4.3.3	GetTemp	40
4.3.4	PI Control	41
5	The Substrate	41
5.1	Fabrication.....	42
5.2	Preparation of AFM Suited Samples	44
6	Liquid Cell Implementation	46
6.1	Setup	47
6.2	First Investigations	48
6.3	Tip Considerations	50
6.3.1	Conclusion.....	51
7	Biological Experiments.....	51
7.1	Experimental Outline & Setup.....	52
7.1.1	Working Procedure	53
7.2	Supernatant of Trichoderma Reesei	54
7.2.1	Overview Imaging.....	54
7.2.2	High Resolution Imaging.....	58

7.3	Cellobiohydrolase 1 (CBH 1)	61
7.4	Cellobiohydrolase 2 (CBH 2)	64
7.4.1	Overview Imaging	64
7.4.2	High Resolution Imaging	68
7.5	Endoglucanase 1 (EG 1)	71
7.6	Summary of Single Component Experiments	76
7.7	Synergism	76
8	Summary	81
9	Outlook	87
10	List of Figures	88
11	Bibliography	92
	I. Appendix A	96

1 Introduction

In a world with sustained growth of human population, the need for renewable energy sources is becoming more and more a global issue. Although there are many new renewable energy technologies known today, the efficient fabrication of Second Generation biofuels from cellulose stays a challenge. Cellulose is an important natural material, being part of terrestrial plants as structure providing biopolymer in the cell wall. Cellulose consists of thousands of sugar molecules, linked together, building up long chains. By cracking these bonds and using the sugar as a resource of energy, biological waste can be used to fabricate biofuel. In its natural form, cellulose is mostly combined with lignin and other polysaccharides (so called hemicelluloses) with cellulose-contents ranging from Coir (32 - 43 %) up to Cotton (95 %) [4]. Plants generate cellulose by photosynthesis with CO₂ as a carbon source and it is estimated, that by this process annual 10¹¹ – 10¹² [4] tons of mostly pure cellulose are synthesized. This makes cellulose the most available and abundant biopolymer on earth.

Mankind has used cellulose from wood and other plants for thousands of years as fire, building substance, clothing, or paper. The discovery of the cellulose degrading microorganism *Trichoderma Reesei* (anamorph of *Hypocrea jecorina*) by the U.S. Army during World War Two [1] indicated a major step in using cellulosic material for human kind. In the years after the discovery a huge amount of effort was put into the investigation of these microorganisms and their cellulose degrading enzymes, called cellulases. Cellulose in its natural form can be classified in two forms, an amorphous form and a crystalline form, mostly combined together in the cell wall. On the molecular level these different allomorphs show different properties (molecular binding, strength and stiffness) requiring different types of cellulases for efficient degradation. This is the reason why cellulose degrading organisms produce a complete cellulase system, where each enzyme fulfills a certain task. These systems show usually strong cooperative action also referred to as synergism. It describes the effect, that the combination of different cellulases yields a higher hydrolysis rate than the sum of the individual enzymes. The understanding of this process is the key for an efficient hydrolysis of cellulose, thus also for biofuel fabrication.

Although researchers have succeeded in the production of biofuel by the usage of cellulases, the efficiency of the process is still way too low to be a competitive source of fossil energy resources as petroleum or natural gas. There are versatile reasons for this low efficiency, where the main reason is the structure of natural cellulose itself. Plants use other components, as lignin, other hemicelluloses as well as proteins to build their cell walls with cellulose. This usually happens in a form where pure cellulose is covered with lignin and other components. By using different combinations of these materials, the plant is able to tune the stiffness and elasticity of its structure. This makes it difficult for cellulases to efficiently degrade natural cellulosic material as the cellulose core is covered with other hemicelluloses, inhibiting the enzymes to work on the cellulose. Cellulases are highly specialized and

work inefficiently on lignin and hemicelluloses. This stays a major problem in biofuel production, independent of the amount or type of cellulase used. To overcome these problems the precise understanding of the degradation process on the molecular level is of essential importance.

There are many methods to measure the hydrolysis empirically with biochemical methods. Although these methods can show degradation velocity and sugar yield, they fail to give site specific information on the nano or molecular level. Nowadays there are many microscopic methods known, which provide adequate spatial resolution. Among these methods Atomic Force Microscopy (AFM) stays the only technique which can measure biological samples in their natural environmental conditions with respect to pressure (ambient) and humidity (up to liquid conditions).

In this thesis we will use the method of liquid cell-AFM to investigate the complex process of enzymatic hydrolysis. The substrates for AFM have to be nano-flat, since a maximum height-variation of about 6 μm is allowed for the used instrument. For this we fabricated a novel substrate consisting of crystalline cellulose embedded in an amorphous matrix of cellulose, which was recently developed at the FELMI together with the Institute for Biotechnology and Bioprocess-Technology [3]. This multi-state character makes this material the ideal candidate for such investigations since natural cellulose is of the same microscopic structure where crystalline regions are embedded in amorphous areas. Therefore this substrate can be seen as a close to nature model material. We will present a technique to produce reproducible and nano-flat cellulose substrates for the investigations with the AFM.

The cellulase system used in this study is part of the fungus *Trichoderma Reesei* consisting of two exo-glucanases also called Cellobiohydrolases (CBH 1 & 2), one endo-glucanase (EG 1) as well as one Beta-glucosidase. Cellulose degradation is investigated in situ by the complete enzyme system and by the individual components. The cooperative activity of this particular enzyme system is analyzed with respect to individual enzyme activities. Since measurements are done in situ and continuous, time resolved evidence for enzymatic activity can be given and activities on the molecular level are resolved.

Furthermore to have controlled conditions in the liquid cell, new mechanical designs where required with a variable temperature controlled stage (+4 to +50 °C). Mechanical and electrical designs are self-constructed and will also be presented in this thesis. They should serve as a basis for dynamic measurements in future studies.

2 Fundamentals

2.1 Biology and Chemistry

2.1.1 Cellulose

Cellulose is a biopolymer and used by terrestrial plants as stability providing element in plant cell walls synthesized in mostly pure form from CO₂ with worldwide annual estimated 10¹⁰ – 10¹² dry tons [4]. This makes cellulose to the most available and abundant biopolymer on earth, found in all kinds of woody plants combined with lignin and other polysaccharides, so called hemi-celluloses. The content is ranging from 32-43% cellulose for Coir to 95% for Cotton [4]. Cellulose as part of wood has been known for many centuries by mankind, as building material, paper, fire and clothing. Nowadays it is known as an adequate material for chemical conversions or the production of so called Second Generation biofuel. The interest into this technique has constantly risen as a result of the growing threat of climate change. Cellulose degradation is difficult, as in its typical form a cellulose core is covered with other polymers such as lignin and hemi-celluloses, making the accessibility and thus efficient degradation difficult.

2.1.1.1 Structure

Cellulose forms chains of β-1,4 glycosidic linked β-D-glycopyranose units (also called cellobiose or anhydroglucose units [AGU]) consisting of hundreds to several thousand units (see Figure 1). The glucose units are 6-membered rings (also called pyranoses) with fixed stereochemistry at carbons 2,3,4 and 5. Glucose can form two stereoisomers at the asymmetric carbon C1 with the hydroxyl group in equatorial (β-glucose) or axial position (α-glucose) [5]. Depending which stereoisomer is used a chain (cellulose) or coil (starch) is formed when polymerizing glucose. The C4 hydroxyl group of one glucose unit can form a bond to the C1 hydroxyl group of another glucose unit forming the 1-4 glycosidic bond, leaving behind one molecule of H₂O. This is done by enzymatic synthesis in plant cells or bacteria by the formation of long chains of linked β-D-glucose units. The preferred chain architecture is the reason for strong intramolecular H-bonding of different cellulose chains, forming a cellulosic crystal. The chain itself has two different ends, one with the C4, C3 hydroxyl groups and one with C1-hydroxyl group. These end groups are called non-reducing and reducing end, respectively. This is important, because different processive enzymes (e.g. CBH 1 and CBH 2) are starting their action at different ends of the chain, where CBH 1 needs a reducing end to start hydrolysis and CBH 2 a non-reducing end.

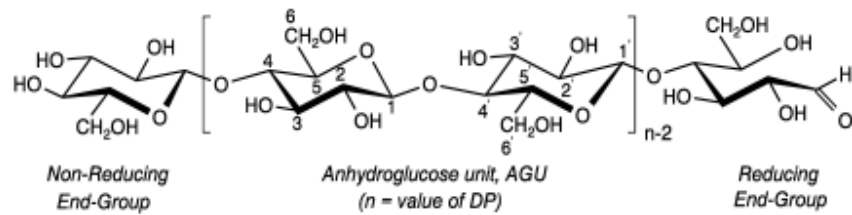


Figure 1: Cellulose chain with reducing and non-reducing end [4].

The morphology of cellulose is defined in a well-organized architecture of fibrillar elements. The elementary fibril is the smallest morphological unit with a diameter of 3.5 nm being assembled out of 36 single cellulose chains [6] (see Figure 2). This assembly is driven by intermolecular Hydrogen bonding, giving these fibrils a high strength and stiffness. These fibrils are covered and partly infiltrated by other hemicelluloses, mostly lignin, additionally stabilizing the structure (see Figure 2). These elementary fibrils assemble then into microfibrils with a diameter ranging from 4 to 30 nm (see Table 1)

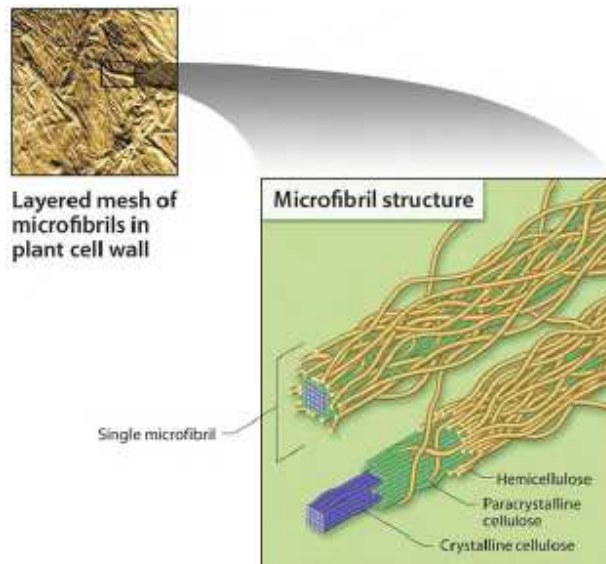


Figure 2: Microfiber [7].

Table 1: Range of microfibril diameter of various cellulose samples [4].

Sample	Microfibril diameter (nm)
Bacterial cellulose	4-7
Cotton linters	7-9
Ramie	10-15
Dissolving pulp	10-30
Avicel [8]	4

2.1.1.2 Physiological Function

The morphology of the plant cell is defined by their fibrillar structure and the size, shape and position of the individual cell. Even dead cells, still containing cellulose, are crucial for the plants life, as for example the bark, which is completely made up of dead cells. During the cells life the primary cell wall is first rare in cellulosic components, with the result that these structures show little strength and stiffness. Later on the cell walls are stabilized with cellulose by associating into crystal structures (fibers), bringing high stability [4]. The crystals are stabilized by hydrogen bonds between the single cellulose chains giving this structure a high stiffness and stability. Stiffness and other parameters can be tuned by implementing other molecules into the cellulosic structure, like proteins, lignin and other hemicelluloses. The structural arrangement of the cellulose fibers plays an important role for the stiffness and strength of a plants cell. In Figure 3 one can see that the microfibrils in the subsequent layers are winded in contrary direction with a certain angle. This improves the strength against tensile strain, where in the secondary wall main body all fibrils show parallel alignment to the growing direction, improving the strength against compressive stress. The biosynthesis of cellulose and it's alignment in the cell wall is not yet completely elucidated [4], but it is believed that the microtubules of the cell play an important role during biosynthesis.

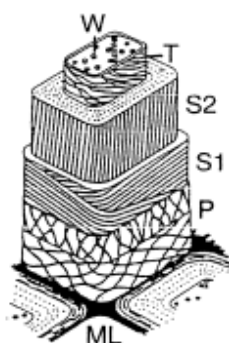


Figure 3: Scheme of the morphological architecture of a delignified wood fiber. W – wart layer; T – tertiary wall; S2-secondary wall (main body); S1 – secondary wall (winding layer); P – primary wall.

2.1.2 Cellulases

Cellulases are a class of enzymes capable of decomposing cellulose, producing free sugar, cellobiose and other oligosaccharides depending on the type of cellulase. They first have been identified indirectly by the U.S. Army during World War Two, due to their problems with the fast denaturation of their cellulosic materials, like tents, sandbags and clothing [1]. The army identified the fungus *Trichoderma Reesei* on a tent residue as the reason for their problems. This event induced high research activity on this field until today, where a variety of other cellulase producing organisms have been identified. These organisms are fungal organisms, anaerobe and aerobe bacteria and even some higher animal as termites and crayfish, which also seem to be able to producing cellulases [9]. The organisms always use

a system or complex of cellulases, for an efficient degradation of cellulosic material. Since *Trichoderma Reesei* is producing high amounts of cellulases, the fungus is still subject of extensive investigations and considered as a good candidate for biofuel fabrication.

Cellulases are, as all other enzyme proteins, produced by the organism from a triplet code on the DNA. In the code itself the sequence of amino acids for the protein is stored. This code is written to a messenger-RNA (m-RNA) strand and transported to the Ribosomes where the enzyme is produced. The Protein is folded after the expression and is now capable to catalyze a certain chemical reaction in the catalytic core of the enzyme (see Figure 10 for the catalytic core of TrCel7A).

Cellulases hydrolyze cellulose in presence of water to cellobiose and other oligosaccharides (see chapter 2.1.2.4). It is important to note that the reaction occurs in the absence of enzymes, with a very low probability at room temperature. The enzymes catalyze the reaction without changing the reaction equilibrium, which holds for all enzymes. The ability of hydrolyzing the cellulose β -1,4-glucosidic bonds distinguish cellulases from other glycosidic hydrolases [9]. Beside the catalytic core, cellulases often have binding domains which enhances the binding to cellulose, thus making the degradation more efficient. The CBDs (Cellulose Binding Domain) task is to stick to the cellulose substrate, thus giving the catalytic domain (CD) time to work. This is may be most important for processive enzymes like CBH 1 and 2 where the enzyme has to move along the chain and stay on track.

It is known for cellulase systems, that the sum of enzyme activity is higher in the collective than for the individual enzymes, which is called synergism. There are 3 Types of synergisms: 1) the endo-exo synergy, 2) the exo-exo synergy; and 3) the synergy between exoglucanases and β -glucosidases.

In this thesis we are aiming our research on *Trichoderma Reesei* by using its cellulase system, consisting of 2 exoglucanases (Cellobiohydrolase 1 & 2) and endoglucanases (e.g EG 1). Additional there is a β -glucanase which is decomposing cellobiose to pure sugar. Cellobiose as a molecule has an inhibiting character on CBH. To exclude this factor from measurements, the addition of β -glucanase was necessary.

2.1.2.1 Cellobiohydrolase 1 (CBH 1)

The 1,4- β -D-glucan cellobiohydrolase 1 (EC 3.2.1.91) or CBH 1 is a exo-glucanase, being capable to degrade the cellulose chain starting from the reducing end. The structure of the enzyme was determined by X-ray scattering where the shape was found to be a tadpole like structure with an isotropic head and a long flexible tail which contains the binding domain (Figure 4) [1]. The cellulose is carried through a tunnel where the catalytic core is located.

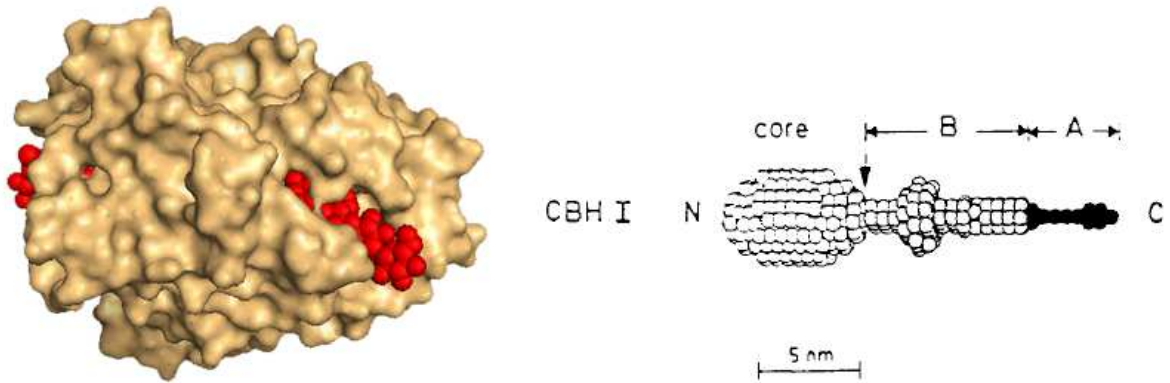


Figure 4: Left: Catalytic CBH 1 core in a side view, loaded with a cellulose chain (red) in the 50 Å long tunnel. Right: Schematic shape of the whole CBH 1 enzyme with the binding domain (A), linker region (B) and the CBD (C) [1].

2.1.2.2 Cellobiohydrolase 2 (CBH 2)

The 1,4-β-D-glucan cellobiohydrolase 2 or CBH 2 is also an exo-glucanase, capable to degrade the cellulose chain from the non-reducing end. According to X-ray investigations, it exhibits a tadpole like shape with a long tail containing the binding domain as shown in Figure 5.

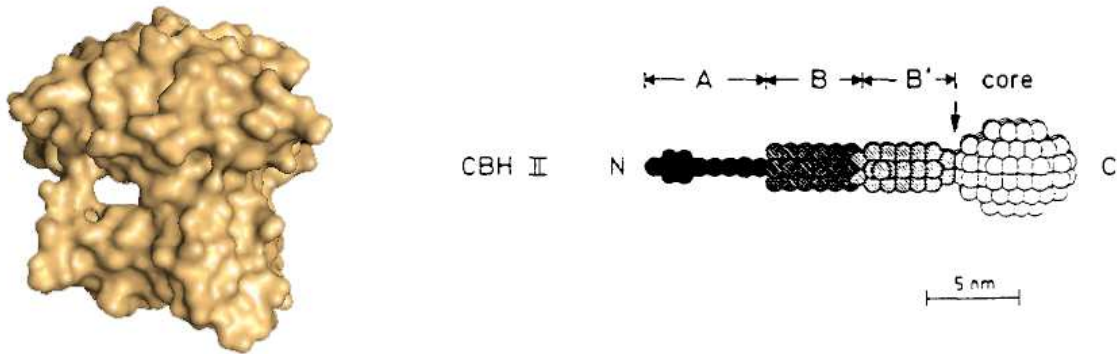


Figure 5: Left: catalytic domain of CBH 2 in front view with tunnel, where the cellulose is transported and cleaved. Right: schematic shape of the whole enzyme with the binding domain (A), linker region (B) and CBD (C) [1].

2.1.2.3 Endoglucanase (EG)

This enzyme is cleaving the cellulose chain randomly by grapping the chain with its special shape. This is producing more reducing and non-reducing ends, which is allowing the CBH's to work more sufficient due to more binding positions. The enzyme has no tunnel where the cellulose is passed through. Its structure is similar to a grabber with a trench in the middle of the enzyme, where the cellulose is

attacked (See Figure 6). Due to geometrical restrictions it works best on amorphous regions of the cellulose.

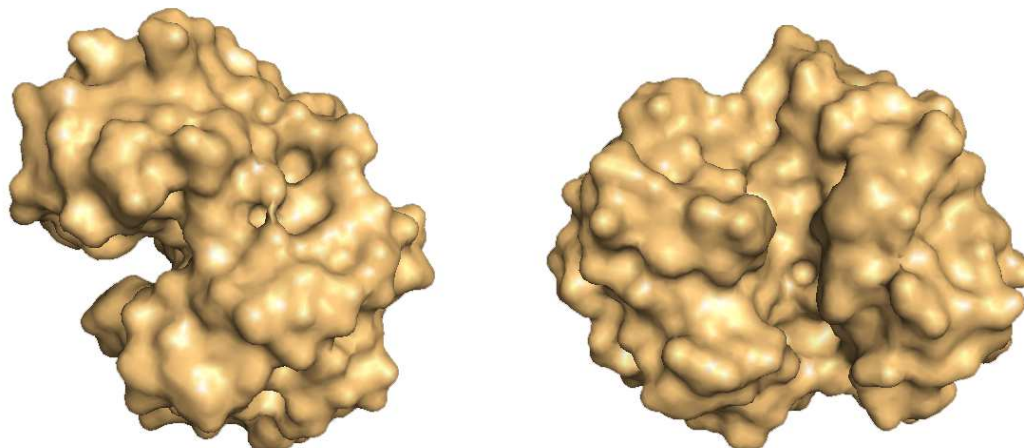


Figure 6: Endo-glucanase 3 (EG 3) from *Trichoderma Reesei*. The enzyme is shown from the side and from below, which reveals clearly the grabbing trench.

2.1.2.4 Hydrolysis

The enzyme system consisting of CBH 1, CBH 2 and EG 1 is believed to work in different steps: 1) endo-glucanases open chains at amorphous and crystalline regions producing more chain ends 2) CBH 1 and CBH 2 bind to this chain ends and degrade crystalline cellulose with their processive activity 3) The new opening is again accessed by EG to further open the gab and the cycle begins again (See Figure 7).

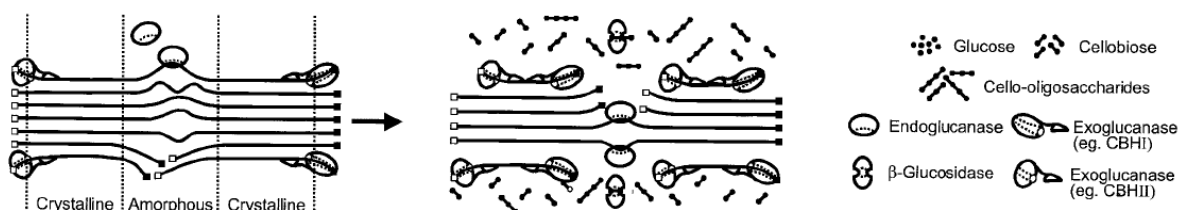


Figure 7: Schematic representation of the hydrolysis of amorphous and microcrystalline cellulose [9].

Briefly, there are two mechanisms possible in the hydrolysis of a glycosidic bond: The *retaining glycoside hydrolase* (see Figure 8) mechanism uses a two-step procedure and the *inverting mechanism* (see Figure 9) which uses one direct step. Which mechanism is implemented in the enzyme is depending on the microorganism.

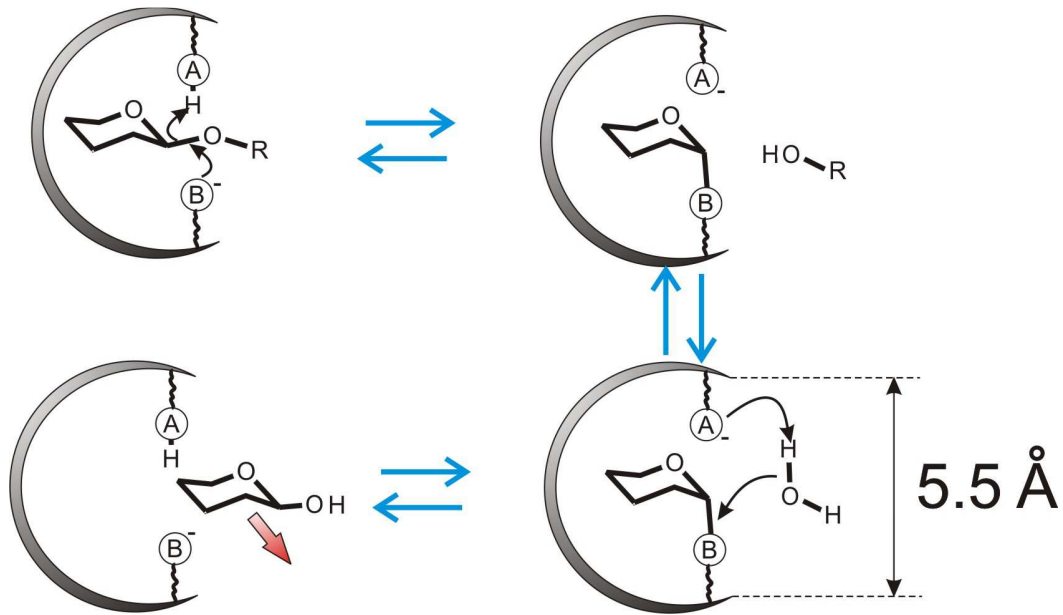


Figure 8: The retaining mechanism of glycosidic hydrolysis.

In the retaining mechanism (Figure 8) the electron of the base undergoes a binding with the C 1 carbon of the sugar, cracking the chain and leaving the Oxygen with an O^- configuration. This is energetic unfavorable and the acid A is deprotonated to form an energetic more favorable OH group. Now the sugar molecule is bound to the base carboxyl group. When a nucleophile (H_2O) is nearby, the nucleophile gives an hydrogen atom to the acid leaving OH^- . The oxygen of the OH^- molecule gives one electron for a new binding to the bound sugar molecule therefore cracking the binding to the base and releasing a sugar molecule. The reaction is also working vice versa and is used by other enzymes to build up cellulose chains.

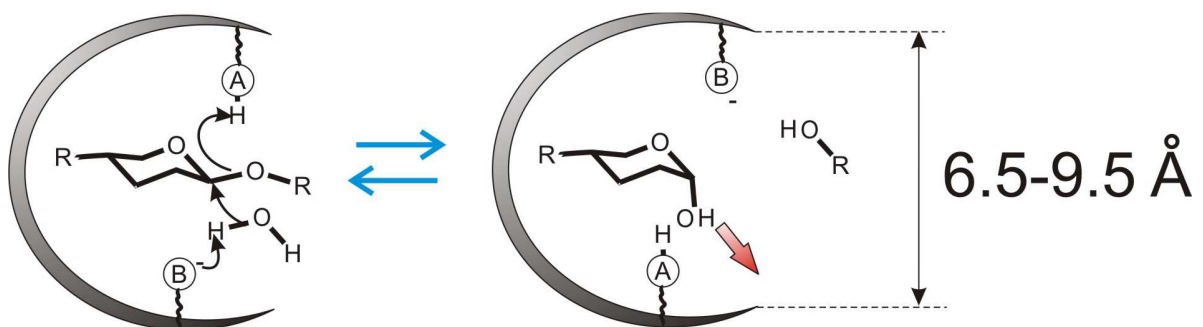


Figure 9: The inverting mechanism of glycosidic hydrolysis.

The inverted mechanism (Figure 9) works in a similar way to the retaining mechanism, where all steps are done at once and the enzyme catalytic side is inverted. The nucleophile H_2O is giving on Hydrogen atom to the base making it acidic. The oxygen in the O^- (OH) configuration gives his electron to a new

binding to the sugar molecule leaving the rest of the chain again with an O^- configuration. This is again unfavorable and the acid is deprotonated, now acting as a base. With this the catalytic center is inverted and the next sugar molecule can be cleaved.

In summary, both mechanisms are used by cellulases to hydrolyze cellulose, where the enzymes usually use two enzyme-born carboxylates acting as base (B) and acid (A) depending on the configuration. The acid catalysis a leaving group departure and the base activates the incoming nucleophile H_2O . These two mechanisms together break the bond, thus releasing a sugar molecule. As indicated in Figure 8 and Figure 9 the two different mechanisms have a different opening distance, with the smaller one for the retaining mechanism.

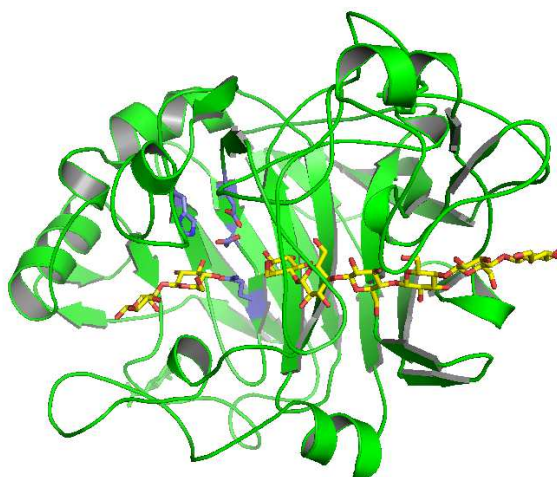


Figure 10: Cel7A (CBH 1) with the catalytic core (blue)¹.

The catalytic core basically formed by two amino groups is small compared to the complete enzyme complex. The complexity of the whole enzyme can be described by the folding to bring the catalytic units close together and the fact that the whole enzyme is producing a favorable reaction environment with his charge distribution. Furthermore, other components are also implemented in the enzyme as the binding domain (CBD) and a mechanism to detect if cellulose is loaded or not. This combination makes the enzyme to a chemical micro-machine highly specialized and very effective. Figure 10 shows the complete CBH 1 catalytic unit in the band model.

2.1.3 Ionic Liquids (IL)

An ionic liquid is a salt in its liquid state, where the temperature overcomes the strong ionic bond between the cations and anions of the salt. For normal inorganic salts these energies range from 8.2 eV for NaCl [10] to 40 eV [11] for MgO where NaCl is dissolved at a temperature of 801°C. Today the term ionic liquid is mostly used for organic salts with a comparable low melting point of 100°C and less. These

¹ With kind permission of Manuel Eibinger

liquids reveal interesting properties, such as high chemical and thermal stability, non-flammability and immeasurably low vapor pressure [13]. A few of these ionic liquids are capable of dissolving cellulose [14] which makes these solvents suitable candidates for processing cellulose in biochemistry.

In this thesis the Ionic liquid 1-butyl-3-methylimidazolium chloride (BMIMCl) is used as the cellulose solvent due to its highest solubility for cellulose of about 8-25 weight %, depending on the method of heating and stirring [14].

2.2 The Atomic Force Microscope (AFM)

The AFM is a scanning probe microscope and one of the major advances in the material sciences since 1950 [15]. The first scanning probe microscope (SPM) was the scanning tunneling microscope or STM, which uses an extremely sharp tip to measure the tunneling current between the tip edge and a conducting sample. A Feedback controller holds the current at a constant value, while the tip scans over the surface, thus recording topographic information. The need of a conducting sample and low temperatures for high resolution is a major disadvantage of this technique. A new technique which allows measuring non-conducting samples had to be invented. In 1986 Gerd Binnig, Calvin Quate and Christoph Gerber constructed an instrument which can do so, the atomic force microscope or AFM [16]. The AFM uses a sharp tip on a cantilever to scan over the surface. It measures certain physical parameters of the cantilever-sample system and controls the movement and the parameters with an feedback controller. The cantilever acts as a transducer for force measurements between tip and sample. In principle there are two ways used to do so, the static and dynamic technique. In the static AFM mode the cantilevers deflection and torsion are used for force and friction measurements, respectively. In dynamic AFM mode the cantilever is oscillated without or with intermitted contact to the sample. Force variations affect the oscillation frequency by alternating the tip sample coupling thus producing a measurable signal for feedback control. Phase lags between actuator and tip come with this method and can be measured additionally, giving information about chemical composition of the surface material. Deflection and amplitude of the oscillation are held constant by the feedback controller by moving the z-position of the tip up and down, thus following the topography of the sample which can be recorded by the computer.

2.2.1 Components

In general the AFM can be divided into five main units: the detection unit, the cantilever-tip system, the tip-sample motion unit, the feedback controller and the image processing unit and display system [15].

2.2.1.1 Tip-Cantilever System

The cantilever is a transducer which converts, in combination with laser-detection system, the forces sensed by the tip into a detection signal. The cantilever and tip are mostly made out of the same material and fabricated by Si-technology used in integrated circuits fabrication. Materials mostly used are silicon or silicon nitride, with or without special covering (gold, metal etc.). The tip shows a typical end-radius of 5-10 nm, although there are tips with a radius of 2 nm or less on the market. This can be achieved with special techniques, e.g. attaching a carbon nanotube at the end. Considerations about the tip radius are very important for the achievable resolution of the AFM. The sharper the tip, the better is the theoretical resolution. Figure 11 shows a typical rectangular and a triangular cantilever with the tip at the end used for tapping and contact modes, respectively (see 2.2.2 & 2.2.3)

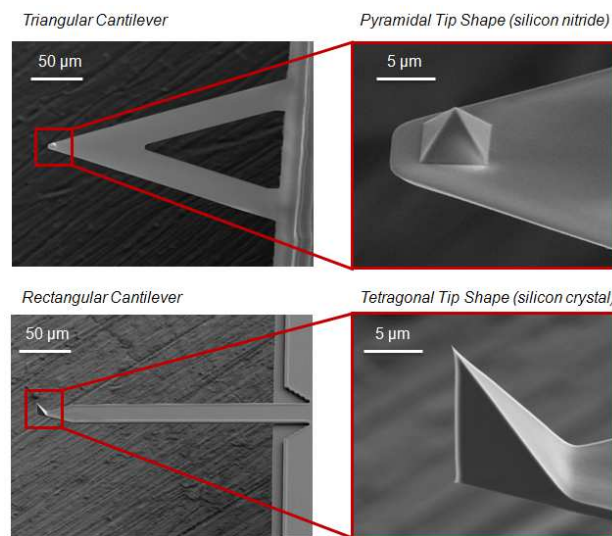


Figure 11: Typical cantilever shapes. Triangular (top) and rectangular cantilever (bottom).

Considering the tip shape (wedge) it is clear that convolution on small features plays an important role (see Figure 12). This is always a problem and has to be considered when images are analyzed. Not only tip convolution plays an important role in AFM imaging, but also particles and dirt attached to the tip, can produce convoluted and unreal signals. This makes careful image analysis essential for image interpretation.

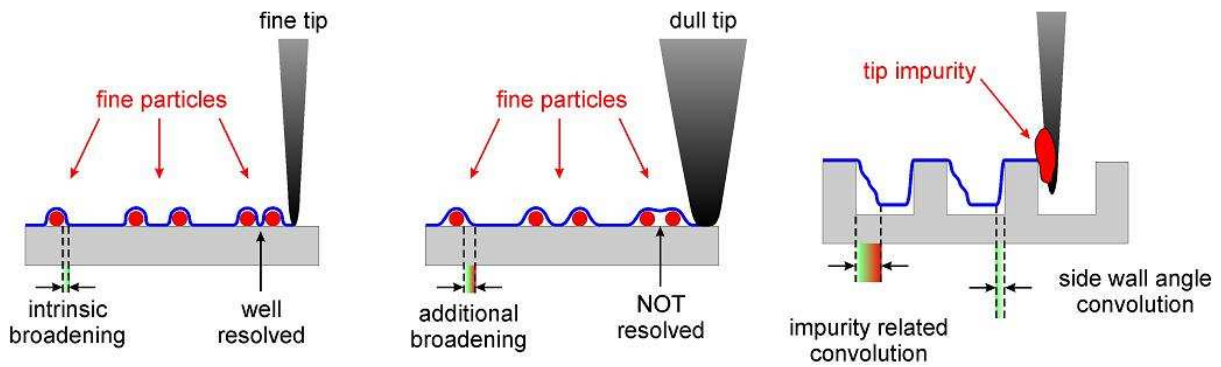


Figure 12: Tip convolution due to tip radius (right) and by tip impurity (e.g. impurities) (left).

2.2.1.2 Detection System

The detection system is sensing the cantilever movement constantly and can be considered as the eye of the AFM. For sensing deformations (bending) or oscillation changes of the cantilever during measurements, different methods have been developed. There are self-sensing methods realized by special coatings on the cantilever backside [17] or tuning fork methods [18]. The most common technique is the optical sensing method where a laser is reflected at the cantilevers backside into a four segment photodetector (PSD). This method is preferred because of its sensitivity and simplicity. If the system is properly tuned, the optical deflection method allows the detection of cantilever deflections below 0.1nm or 1Å [15]. The four segment array allows measurements of lateral and vertical distortions of the cantilever. The lateral torsion of the cantilever can give information about the friction force in contact mode AFM. The different Photodiode signals are fed to a differential amplifier, which is then giving the amplified signal to the feedback controller where the distortion of the cantilever is compensated. Figure 13 shows the detection system of the AFM with the tube scanner attached to the cantilever.

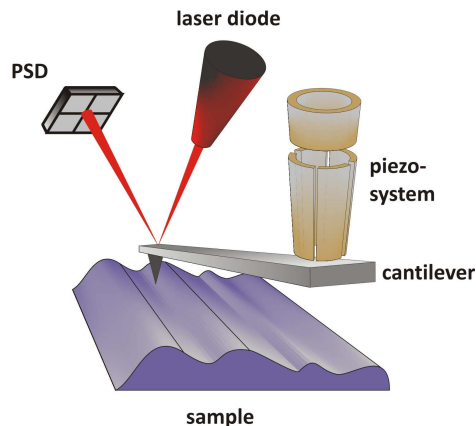


Figure 13: Principle of an AFM System: The laser is reflected at the tips backside into the four segment photodetector (PSD).

2.2.1.3 Motion System

The motion system uses piezo-electric actuators for positioning the tip on the surface in x,y and z direction. These crystals deform with high accuracy when a voltage is applied, as shown in Figure 14 A. With the voltages applied to the piezo tube scanner, the tip is scanned over the sample surface while the z-voltage in each single point is adapted via the controller. By using a calibration file, the z-voltage can be transferred into topographic information. Such motion systems are commonly used for AFM systems, covering a wide scanning range from a few nm² up to more than 100 μm². Disadvantageous for tube scanner systems is the fact that the lateral displacement is coupled with the vertical displacement coming from the conical movement of the tube scanner. The tube scanner motion system is illustrated in Figure 14 B. The piezo electric tube has 5 electrode pairs, where four are used for the motion in x and y direction and one for the displacement in the z-direction. The tube scanner is deforming its shape in x and y direction when a contrary signal is applied to the two x electrodes. With this the tube is bending to one side, following a circular orbit and moving the tip slightly away from the sample. Hence x-y movement couples with z-movement, which must be compensated by the z-piezo (see Figure 14 C).

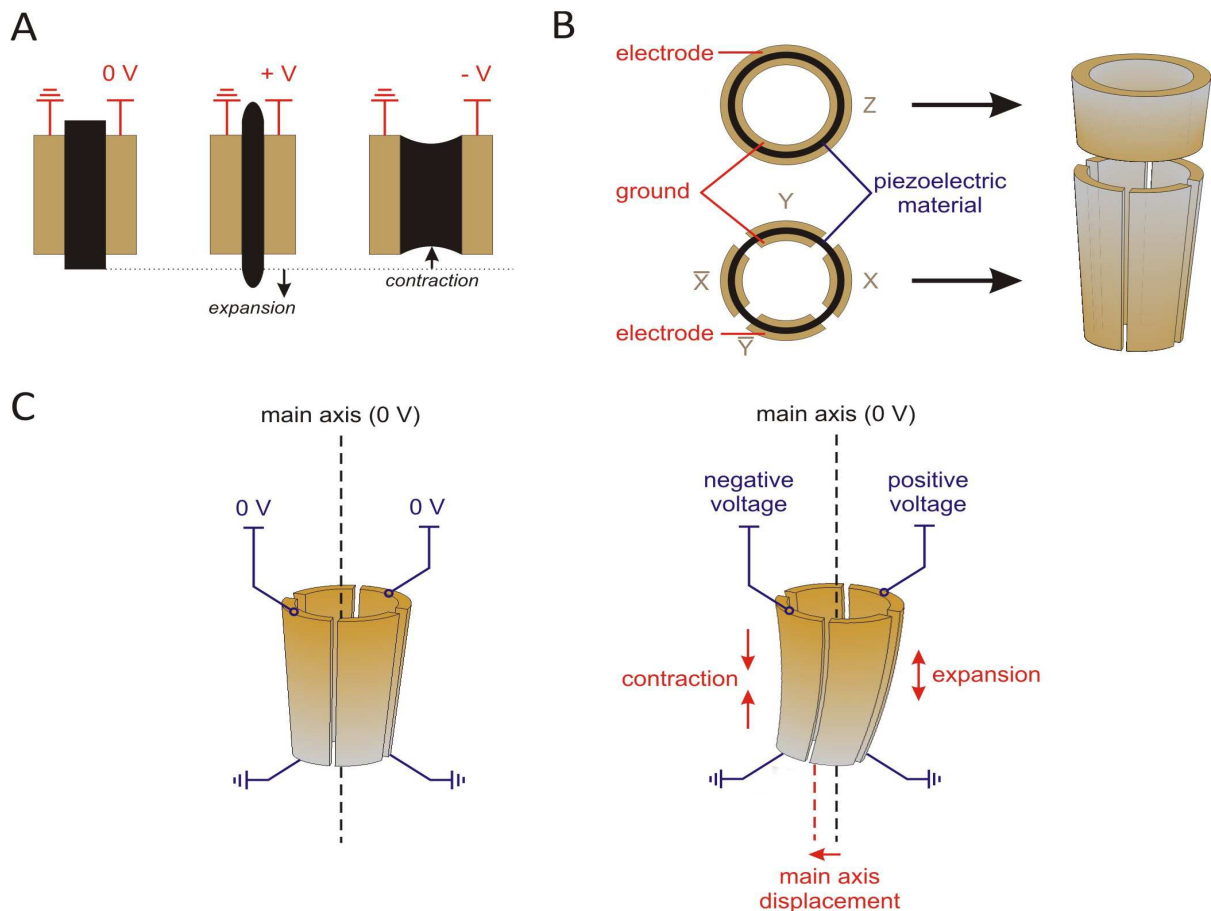


Figure 14: A: basic behavior of a piezoelectric material. B: tube scanner with the electrodes and the piezoelectric material. C: (x,y) Axis movement of the tube scanner. A contrary voltage is applied to the two electrode pairs.

2.2.1.4 Feedback Loop and Image Processing Unit

Most AFMs operated in ambient conditions use the amplitude as the detection signal and input parameter for the feedback loop. The AFM tries to maintain constant amplitude by permanently comparing the actual tip amplitude with the preset value (amplitude set-point). When operated in contact mode the AFM uses the deflection of the cantilever as the feedback parameter. By comparing a preset value (the deflection set-point) to the actual deflection of the cantilever the surface topography is scanned. This is the basic principle of the feedback loop, with the loop trying to achieve a constant value of the input parameter while scanning over the surface. Loop parameters (integral and proportional gain) controlled by the operator influence the feedback loop thus tracking the surface. By tuning these parameters the tracking of the surface by the tip can be optimized, corresponding to an optimal feedback loop. Both parameters take influence on the reaction speed of the loop to topographic changes. If the gains are set to high, thermal fluctuations may cause a noisy signal, while too long reaction times will not show small or sharp features on the surface. Hence accurate and careful adjustment of these parameters is necessary for good and artifact free images.

2.2.2 Contact Mode AFM

In this mode the tip is always in contact with the sample, without any excitation of the cantilever. The cantilevers are soft and the tip is moved onto the surface. This is manifested in a bending of the cantilever, thus moving the laser beam. When the Tip is now scanned over the surface this bending, or the position of the laser on the detector is held constant (see Figure 15).

Figure 15 shows the working principle of contact mode AFM, where the tip is moved over the surface. Figure 15-A shows the tip pressed on the surface, according to the preset deflection set-point which defines the normal force. When the tip gets to a higher feature during scanning the cantilever bending is stronger and the laser reflection is shifted at the detector (Figure 15-B). This is compensated by the feedback loop by the use of the z-piezo (see Figure 15-C). In Figure 15-D the scanning is continued and the topography for one line is finished. The topography is recorded first as the z-piezo voltage and then translated to height information via a calibration curve.

One problem of this technique is that the tip is applying a force to the sample. On very soft samples the tip can modify the sample while scanning resulting in damaging, delaminating, or material removal due to a harder and sharp tip. This can be avoided when using a non-contact AFM method, such as Amplitude Modulation AFM which will be described in the next chapter.

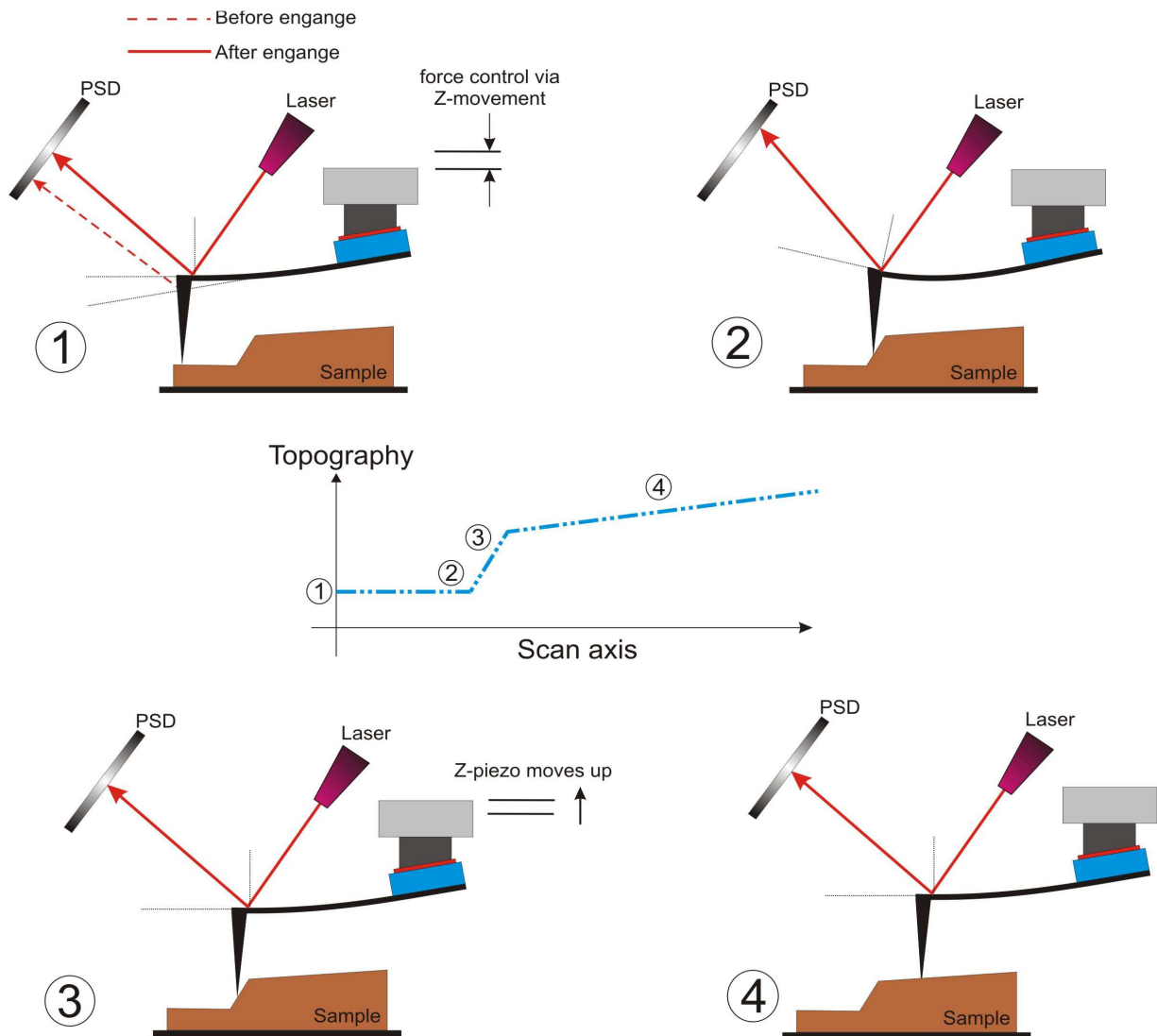


Figure 15: The principle of contact mode AFM operation. The tip is scanned over the surface while the deflection of the cantilever is kept constant.

2.2.3 Tapping and Phase Mode AFM

This principle applies to normal conditions in gaseous environment as well to liquid conditions. In this mode the tip is oscillated far away from the sample at a certain frequency, which is mostly the first mechanical resonance of the tip-cantilever system. Shape and position of the resonance peak are depending on the stiffness of the cantilever (force constant) and the quality factor (Q-factor). The Q-factor is related to the hydrodynamic damping of the cantilever in the applied environment (air, gas or liquid). The quality factor is also a quantitative measure of the peak sharpness and defined as: $Q = \frac{\omega_0}{\Delta\omega}$ with ω_0 as the resonance frequency and $\Delta\omega$ as the width of the peak at half maximum (FWHM). Hence, high Q-factors are found when the peak is narrow and sharp whereas low Q-factors show a broad peak.

In terms of sensitivity a high Q-factor is desired, where the highest Q-factors can be reached in vacuum and low Q-factors usually are present in more viscous mediums (liquids).

When the tip approaches the surface the oscillating system couples with the surface potential (the different forces can be seen in Table 2), which changes the resonance frequency and thereby amplitude. The amplitude is reduced by continuing the approach until the set-point amplitude is reached, which again is defining the “pressure” onto the sample. Lowering the amplitude set-point causes a stronger normal force of the tip onto the sample. If the tip scans across the sample surface and a height variation is present, the coupling and thus amplitude changes. This is recognized by the feedback loop and compensated via the z-piezo. Varying cantilever-sample coupling also affects the phase lag between excitation- and cantilever oscillation. A different coupling can be caused either by height variations or material differences in the sample, thus giving this technique the advantage of simultaneous detection of height and material variations. Phase Mode AFM cannot show different materials qualitatively but quantitative information about material disposition is possible. Combining both height and phase information enhances the possibilities of this technique in respect to material and surface analysis tremendously.

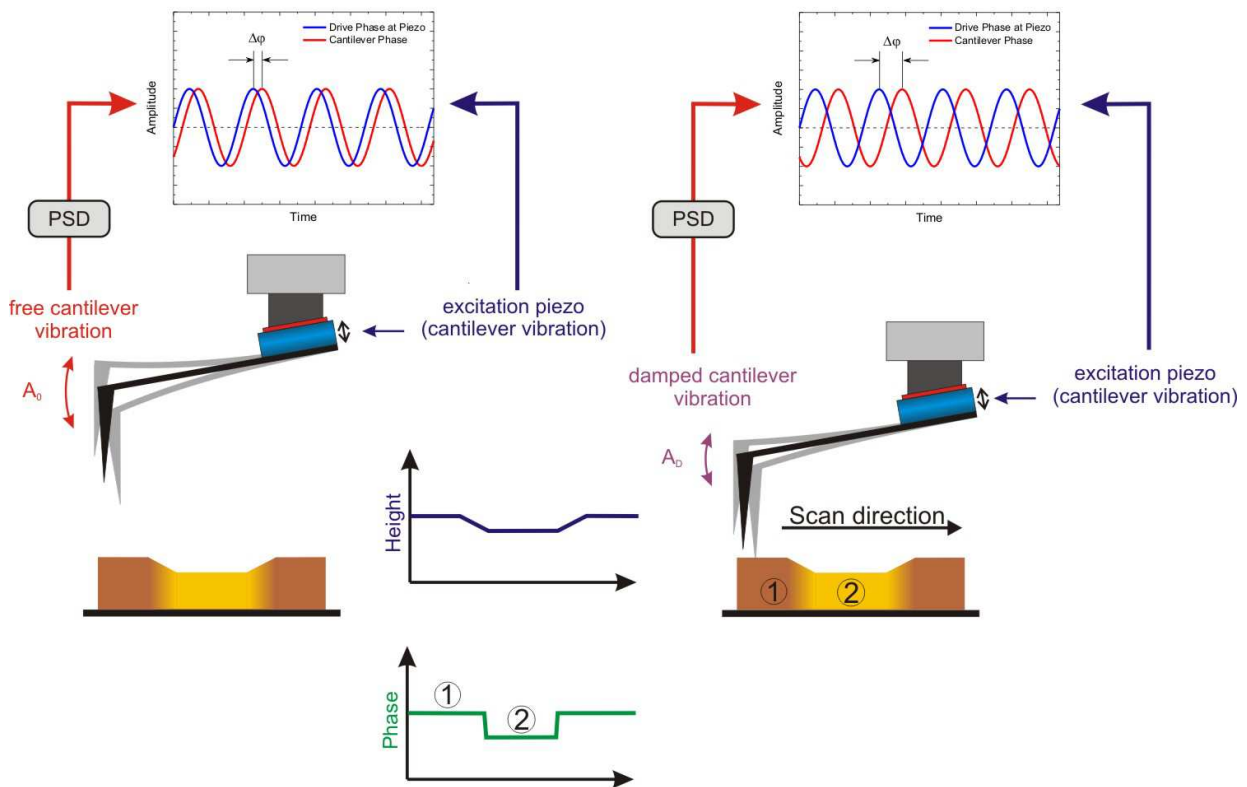


Figure 16: The basic function of AM-AFM operation. There is additional information (material contrast) in the phase lag between excitation and cantilever vibration.

There are usually two regimes where the oscillation can be driven: the overall forces can be attractive (Van der Waals) or repulsive (Pauli-forces or ion repulsion). In attractive regimes, the tip is not in physical contact with the sample. In repulsive regimes, the tip is tapping the surface which is equivalent to a higher energy input to the sample, although still less than in contact mode.

The possibility of simultaneous collection of height and phase information are the main advantages of this technique. Therefore this is the standard mode in most AFM investigations.

2.2.4 Nanoscale Forces

There are a number of different interaction forces between the tip and the substrate. This chapter gives a quick overview over the different types of Forces in gaseous and aqueous conditions. Table 2 shows a quick overview of the forces.

Table 2: tip-sample interaction forces in air and liquid conditions.

Name of Force	Interaction range	Type of Force
<i>Van der Waals</i>	<i>mid-range</i>	<i>attractive</i>
<i>Pauli repulsion</i>	<i>short range</i>	<i>repulsive</i>
<i>Ion-ion repulsion</i>	<i>long range</i>	<i>repulsive</i>
<i>Capillary force</i>	<i>long range</i>	<i>attractive</i>
<i>Electrostatic double layer force</i>	<i>long range</i>	<i>repulsive</i>
<i>Solvation force</i>	<i>long range</i>	<i>repulsive/attractive</i>
<i>electrostatic</i>	<i>very long range</i>	<i>repulsive/attractive</i>
<i>magnetic</i>	<i>very long range</i>	<i>repulsive/attractive</i>

1. Van der Waals forces

This force arises from electrostatic field fluctuations in the atomic orbital. Since electrons are not localized, the net electrostatic balance point fluctuates, which gives rise to a long range interacting force. The force for a conical mesoscopic tip with a half sphere ending is given by equation (1).

$$F_{vdw} = -\frac{H}{6} \left(\frac{R}{d^2} + \frac{\tan^2 \beta}{d + R_\beta} - \frac{R_\beta}{d(d + R_\beta)} \right) \quad (1)$$

In equation (1) H is the Hamaker constant, R is the tips Radius, d is the instantaneous tip-surface distance, β is the half angle of the cone and $R_\beta = R(1 - \sin(\beta))$ [15]. This force follows a $1/d^2$ form and is therefore of mid-range. It may be worth mentioning that the Van der Waals Force is not always attractive. In liquid the force can also be repulsive depending on the dielectric constants and reflective index [15].

2. Pauli repulsion & ion-ion repulsion

The Pauli repulsion arises from the quantum mechanical principle that two fermions with the same quantum number cannot exist in the same state of energy. When two atoms are brought together with filled orbitals they repel each other when the two orbitals start to overlap. This is a very strong force as can be estimated by the energy which is needed to bring hydrogen to fusion. (e.g. in the sun's core).

Another form of repulsion with a long-range character is formed when two ions with the same charge approach each other. Electrodynamics teaches us that ions or charges with the same charge repel each other with a force following a $1/r^2$ rule. This force is of long range and attractive when the ions or charges are of opposite sign. The tip is a bulk material not including any ions, so ions have to bind to the tip and sample surface. This requires a charged tip or surface which applies when the tip or sample is in contact with a polar liquid (e.g. water). Binding of ions to the surface liquid interface leads to charge compensation. This is forming a double layer of ions, hence leading to the electrostatic double layer force (see *Electrostatic double layer force*).

These two forces are responsible for the repulsive nature of the overall force when the tip is operated in tapping mode. The forces themselves are applied to a big number of atoms (hundreds to thousands) at the tips edge. Therefore the description with contact mechanic models is more sufficient. These models will not be discussed in this thesis, but there is a substantial description in the book from Garcia [15].

3. Capillary force

In ambient conditions a thin wetting layer on the surface of the sample is always present, even when operated in glove box conditions with below 0.1 ppm H_2O . By hitting the sample surface the tip has to penetrate this layer, thus leading to a water meniscus around the tip. If the tip wants to leave the surface, this water meniscus is leading to an attractive force which is called the capillary force. This force depends on the relative humidity and the distance between tip and sample. The problem is that the force is rather strong and can dominate all other forces in the AFM, which makes

it impossible to observe smaller objects as the meniscus. In Liquid environment this force isn't present which is an advantage.

4. Electrostatic double layer force

In a polar liquid, such as water, surfaces get charged by the liquid. This charging can either happen by ionization of surface atoms or ion adsorption from the liquid. This forms an electrostatic layer between solid surface and liquid which screens electrostatic fields from the surface. The double layer force is the result of two surfaces coming together in the liquid (Tip-Sample). Depending on the ion concentration of the liquid the layer can range from 0.2nm to hundreds of nm [15] which can influence the measurements considerably. By changing the pH value the ion concentration can be tuned, thus leading to a screening of this electrostatic force. This can be used to improve AFM measurements in liquids [19].

5. Solvation force

This kind of force arises from the fact that liquids and solid surfaces are made of discrete entities such as atoms or molecules [15]. At the interface between solid and liquid, conditions are different to the bulk liquid. This is influencing the liquid molecules and builds a different liquid-layer close to the solid surface which is different to the bulk liquid. To observe this effect organic liquids are most promising when the organic molecules builds up a self-assembled structure at the surface. If these structures are then squeezed between two surfaces (tip-sample) an oscillating force can be observed. This behavior has also been observed for water [20] but is most present in organic liquids.

2.2.5 Theoretical Description of AM-AFM

This chapter is mostly taken from the book of Ricardo Garcia, but summarized and shortened. For a more precise description see Chapter 4 and 5 in Garcia [15]. To start with a theoretical description, the equation of motion has to be found. However, for AFM this is a difficult task because it is a three dimensional problem with a complicated assembly. The cantilever exceeds the mass of the tip by magnitudes of order. Therefore, the assumption of a rectangular beam without the tip is a substantial simplification [15], as illustrated in Figure 17.

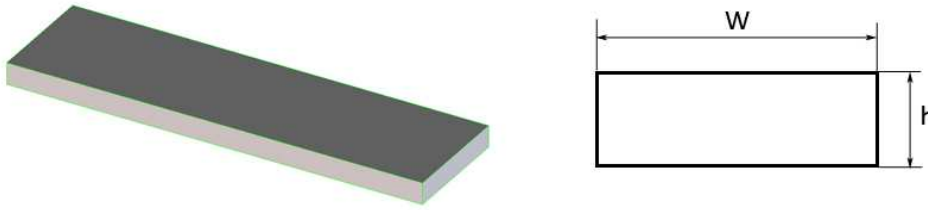


Figure 17: The assumption that the cantilever-tip shape can be simplified by a rectangular beam.

The beam is the cantilever with the tip as a single mass point at the end. This is a mechanical simplification while forces on the tip have still to be considered on the real shape of the tip. The mathematical equation (see equation (2)) of this system is a modified Euler-Bernoulli beam equation with the introduction of some dissipative elements and the tip-surface force.

$$EI \frac{\partial^4}{\partial x^4} \left(w(x, t) + a_1 \frac{\partial w}{\partial t} \right) + \rho W h \frac{\partial^2 w}{\partial t^2} = -a_0 \frac{\partial w}{\partial t} + \delta(x - L) [F_{ext}(x, t) + F_{ts}(d)] \quad (2)$$

In this equation $w(x, t)$ is the displacement of the cantilever perpendicular to its main axis. E, ρ and I are the Young modulus, mass density and the area moment of inertia, respectively. L, W and h are the dimensions of the rectangular beam. $F_{ext}(x, t)$ stays for the excitation force and $F_{ts}(d)$ implies all tip surface interaction forces. Solving this equation is a formidable and hard task where considerable mathematical skills and tools are needed [15]. So it may be more of interest to start with an easier equation in a simplified model to understand the basic behavior of such a system.

2.2.5.1 The Point-Mass Model Described by a Harmonic Oscillator

A good starting point may be the cantilever far away from the sample where no tip-surface interaction forces are present. At this point the equation of motion can be simplified as a Harmonic oscillator with sinusoidal excitation (equation (3)).

$$m\ddot{z} = -kz - \frac{m\omega_0}{Q}\dot{z} + F_0 \cos(\omega t) \quad (3)$$

This equation can easily be solved and two independent solutions can be found which can be combined to give the final solution for this problem. Further the Amplitude and the phase lag between excitation and immediate motion can be calculated. The amplitude follows a Lorentzian expression while the phase lag moves from 0° for low frequencies to 180° at high frequency with 90° phase lag at the resonance frequency of the system (Figure 18).

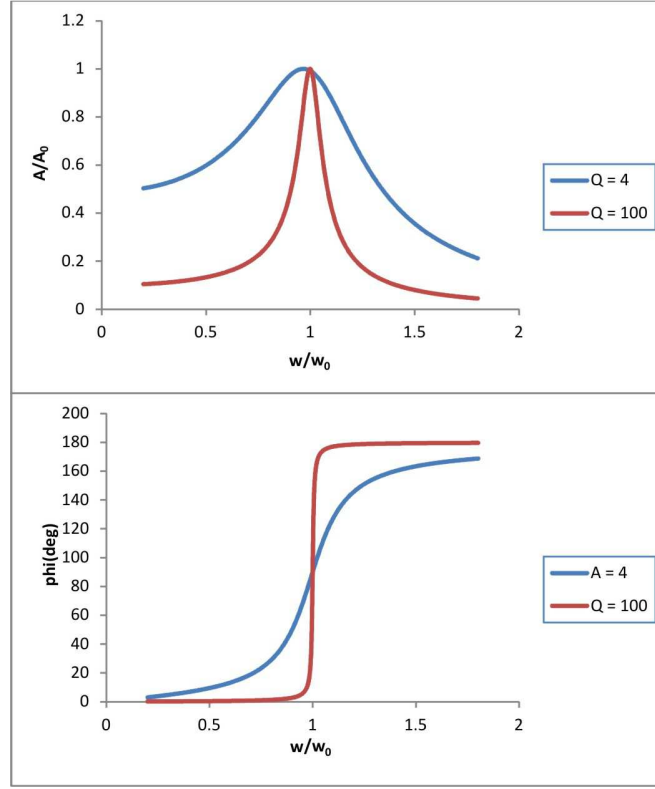


Figure 18: Amplitude resonance and phase shift diagram for a harmonic oscillator.

If the cantilever approaches the surface, the tip starts to recognize the nanoscale forces depending on the distance to the sample. In this case, equation (3) has to be adapted with an interaction force term F_{ts} (see equation (4)). However, the nonlinear character of these forces prevents an analytical solution. For small displacements, compared to the equilibrium position of the cantilever, the linearization of these forces is possible (equation (5)). Although it holds only for small displacements, it can be used to understand the basic behavior of AM-AFM.

$$m\ddot{z} = -kz - \frac{m\omega_0}{Q}\dot{z} + F_0 \cos(\omega t) + F_{ts}(z) \quad (4)$$

$$F_{ts}(z) = F_{ts}(0) + \left. \frac{dF_{ts}}{dz} \right|_0 z \quad (5)$$

In this case the equation is linear again and continued as weakly perturbed oscillator. The term $\left. \frac{dF_{ts}}{dz} \right|_0$ can be seen as an additional spring constant k_{ts} coming from the interaction with the surface [15]. This leads to the final equation (6), where $(k - k_{ts})$ can be seen as the effective spring constant k_{eff} .

$$m\ddot{z} = -(k - k_{ts})z - \frac{m\omega_0}{Q}\dot{z} + F_0 \cos(\omega t) + F_{ts}(0) \quad (6)$$

Now the solution of this problem leads to a new resonant frequency with a negative shift for attractive forces and a positive shift for repulsive forces (see Figure 19).

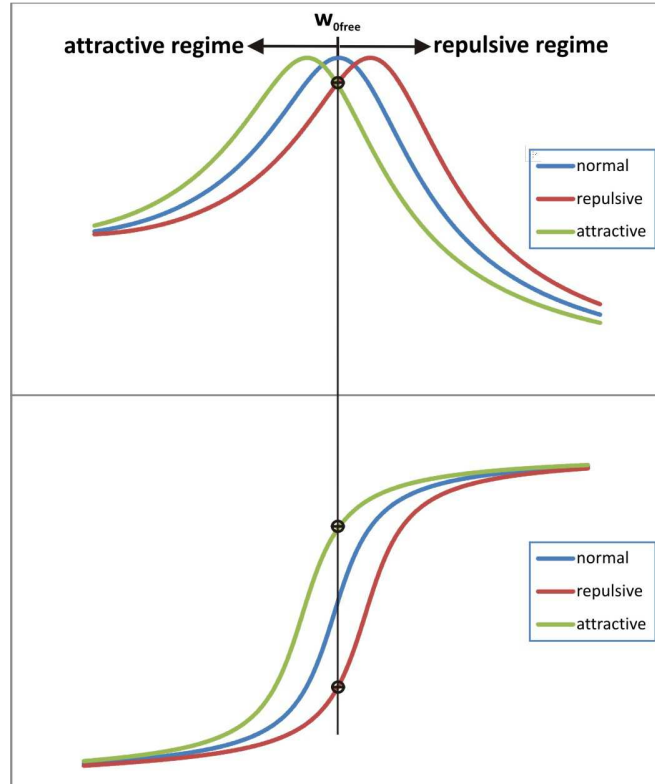


Figure 19: The weakly perturbed Harmonic Oscillator depending on the force regime.

When the tip comes into contact or near the surface, the resonance of the peak shifts and the amplitude of the free oscillation frequency is reduced (circle in Figure 19 top). However, this damping does not allow determining the working regime. Considering now the phase shift with respect to the free oscillation, it can be seen that different forces lead to a different sign of the phase shift (see Figure 19).

The amplitude damping and phase shift is detected by the photodetector, processed by the feedback loop and allows finally for imaging topography and phase contrast. This very simple introduction to the AM-AFM holds for most applications and shows the basic principle behind AFM measuring, although special phenomena will need a more precise and sophisticated description. A more advanced theory can be found in [15] which will also describe unstable solutions and occurrence of two stable oscillation regimes.

2.2.6 The AM-AFM in Liquid Environments

Operating an AFM in liquid environment is one of the most interesting and challenging application of the AM-AFM. In this environment, the behavior of the cantilever is completely different as for gaseous

conditions. The major change is induced by the high viscosity of liquids and the dramatically increased hydrodynamic damping. Furthermore new forces, with different properties are induced, like the electric double layer force. The capillary force is now missing on the sample, which can be seen as a big advantage. By looking on the dynamics far away from the surface, it is first observed, that there is a damped, broadened resonance peak of the cantilever (see Figure 20). Not only that the resonance is damped it also shifts to lower frequencies by about 3-5 times (rule of thumb). The whole frequency spectrum changes, due to additional resonances coming from water and liquid cell (LC) oscillations, which couple to the cantilever. This makes it more difficult to find stable measurement regimes. Nevertheless, this technique represents the only one, capable of measuring biological samples in their natural environmental conditions.

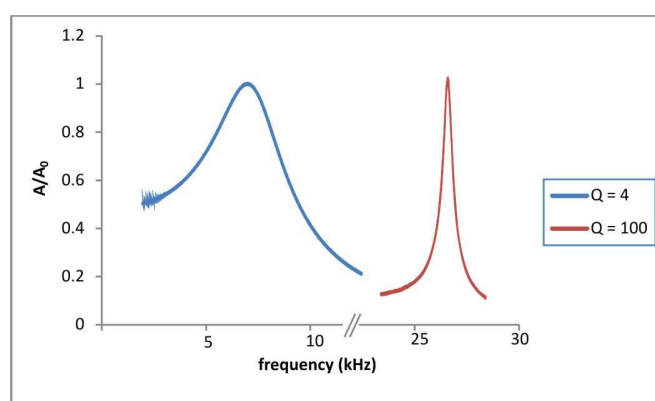


Figure 20: Schematic illustration of resonance peaks of a cantilever in air (red) and the same cantilever in liquid (blue).

When the tip is now approaching the surface, the resonance peak is broadened even more and the peak is shifted to lower frequencies [15]. This reduces the quality factor for decreasing distances, depending on the Eigenmode (resonance) and on the tilt angle of the cantilever [15]. The reason for this is, that at the solid-liquid interface a boundary layer of the liquid forms which is different from the bulk liquid (see solvation force in 2.2.4). This boundary layer is formed on the cantilever as well on the sample surface. When the gap is further decreased these layers occupy a greater fraction of the gap and gives rise to more damping from fluid shear forces [15].

Another major change is the no longer symmetric interaction of the tip with the sample (see Figure 21). At the bottom of the oscillation the distortion is more distinct, due to more eigenmodes contributing to the oscillation. This shows that the oscillation cannot be seen as a sinusoidal wave form any longer. It also shows that the theory for liquid operation is more complicated, firstly because of the higher damping and the different forces and secondly because more Eigenmodes have to be considered.

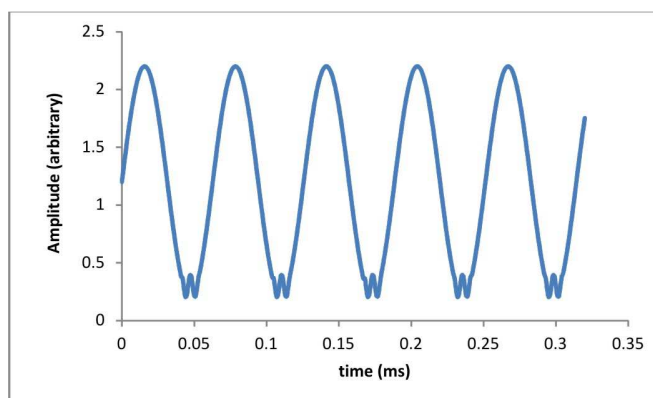


Figure 21: Schematic of the cantilever deflection waveform in aqueous conditions.

Another important change can be recognized when working with buffer solutions. The electric double layer force can be modified by the ion concentration of the buffer solution. So the pH value can be used to screen long range interaction forces and enhance the resolution of the measurement [21]. This should be kept in mind, when molecular resolution is required (see also electric double layer force in 2.2.4).

2.3 Ultramicrotomy²

The Ultramicrotome is used to prepare ultra-thin sample slices below 50nm, mostly used for TEM but also for other techniques like Raman spectroscopy. It can also be used to make sample surfaces nano-flat. The basic Ultramicrotome has 4 main components:

1. the chassis with the included feed mechanism and microscope
2. the positioning setup for slice thickness etc.,
3. the Sample fixation
4. knife fixation.

² All figures and Information are with kind permission from Claudia Mayrhofer



Figure 22: The Ultramicrotome.

The knife, which is one of the most crucial parts of the Ultramicrotome, can be fabricated out of glass or diamond (see Figure 23)). Most diamond knives have a trench behind them, which is filled with water to collect the ultra-thin lamella.



Figure 23: 3 Types of the diamond knives from left to right 35° knife with trench, 35° knife without a trench, 45° knife with trench and a glass knife.

3 Experimental Concept & Requirements

The following experiments are based on the work of Judith Dohr [3], where the preparation of nano-flat cellulose substrates of cellulosic material was one of the main goals. This thesis is the continuation of this work and is aimed on the real-time observation of cellulosic degradation by enzymes of the fungus *Trichoderma Reesei*. Dohr and coworkers used cellulosic materials, fabricated from cellulose powder (Avicell) and ionic liquids (BMIMCl), to produce a new cellulosic material. They developed a special preparation procedure for nano-flat cellulose substrates by using ultramicrotomy techniques. This method allowed the measurement of the cellulosic degradation on reproducible cellulosic materials. Dohr and coworkers performed the measurements without a LC for the AFM. The experiments have been done by a special procedure, where the samples were incubated first with enzymes, then dried for the AFM investigations. This technique is sufficient to acquire time resolved single images of the degradation process. It shows the basic behavior of the degradation process, but excludes the time in between, where the degradation takes place. Furthermore, there is a risk of damaging the sample during drying. Another problem of this approach is the stickiness and softness of the sample, due to water adsorption by cellulose. This leads to very rough measurement conditions, with high amplitudes and low set-points in the repulsive force regime. This and the assumed thick water layer on the sample are leading to capillary forces preventing high resolution imaging on the nm range. Nevertheless, they found an interesting behavior of the degradation process and proposed a new theory for this behavior, which expands the currently accepted models [22].

To expand the investigations to the nm range, we decided to implement Liquid-AFM (L-AFM) to get an insight in the dynamic behavior during the degradation process. Another requirement was the design of a mechanical setup for the special samples holder used during preparation and experiment (see Figure 26). This was necessary, because the sample has a special shape and is fixed in a sample holder which is too big to use a petri dish as water containing basin (see Figure 25 for the normally used sample holder). Additionally, it should also be possible to control the temperature of the buffer solution. Therefore following requirements had to be fulfilled for such experiments

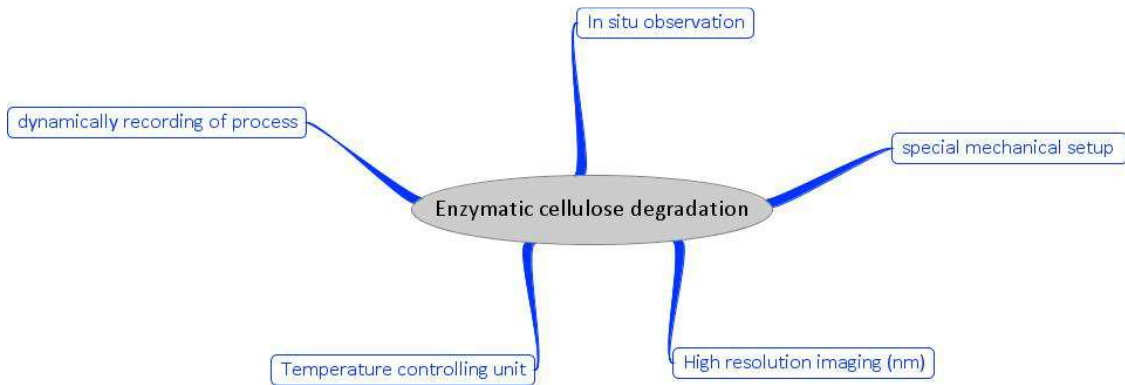


Figure 24: Requirements for the experiment. For precise description see text above. ³

Now that all requirements are defined and noted, solutions to these requirements had to be found. The following chapter presents the solutions for different requirements and shows furthermore the strategies for our dynamic experiments.

4 Designs & Problem Solutions

This chapter presents the solutions for the mechanical and electrical issues. Experimental solutions are given in the chapter 7. The solutions to mechanical and electrical problems have been supported by many colleagues and I want to give my acknowledgments to them for their support. Technical drawings can be found in Appendix A.

4.1 Mechanics

Since sample holders and samples themselves are having special shapes, a new design for the entire system had to be found. The AFM can be used in a certain z-range, where the scan-head can move (about 7 μ m). The height of the stage, the sample holder, plus the cell forced us to design a new mechanical setup which can be mounted at the side of the stage. Any other solution would exceed the maximal z-height or come too close to this limit, which prevents safe AFM operation.

4.1.1 Sample Holder

The sample holder for normal samples can be seen in Figure 25. It has a rod below the head, which is used for fixation in the ultramicrotome, as well as fixation on the AFM stage. Since we had to build a small water bath for the liquid measurements, it was no longer possible to have such a rod. Especially

³ Mindmap out of Freemind Version 0.9.0 RC 10. Author: Joerg Mueller GNU Licence

the mass of the system is a big limitation, because every gram of material has to be heated or cooled by the temperature unit.

Additionally the material of the normal sample holder is Aluminum. Although it is a cheap and light material, it has the disadvantage that it is chemically not quite stable. Solution containing salts may attack and dissolve aluminum which is contaminating the buffer-solution and much worse, may inhibit enzymatic action. To overcome these problems a new, more chemically resistant sample holder had to be designed. Stainless steel was chosen as material, since it shows no or little corrosion and is chemical stable and easy to clean. In Figure 26 the 3D design of this Sample holder can be seen, as well as a picture of the finished Sample holder.



Figure 25: Typically used sample holder. (1): fixation screw, (2): sample, (3): fixation rod for ultramicrotomy & measurement.



Figure 26: New sample holder. Left: 3D drawing of it. Right: Fabricated sample holder with sample

4.1.2 Fixation for Ultramicrotomy

Since the rod for fixation is now missing, a fixation tool for the ultramicrotome cuts had to be designed. Figure 27 shows the 3D modeling of the holder and the final form after fabrication. It has a hole in the

center to be compatible with the conventional sample holders. The used material is brass, since it is easier to handle than stainless steel.



Figure 27: Fixation part for ultramicrotome use. Left: 3D drawing. (1) is the hole for stick holders, (2) is the drilling for the fixation screw. Right: after fabrication.

This part is now compatible with the used Ultramicrotome and allows the use of the new sample holder, as well as the old sample holder. The advantage is, that the sample itself (Epoxy + cellulose fragment) stays in this sample holder for the whole time during fabrication and measurement. This guarantees that the samples are flat without a tilt in the x,y axis in the AFM measurement. Figure 28 shows the fixation tool in action.

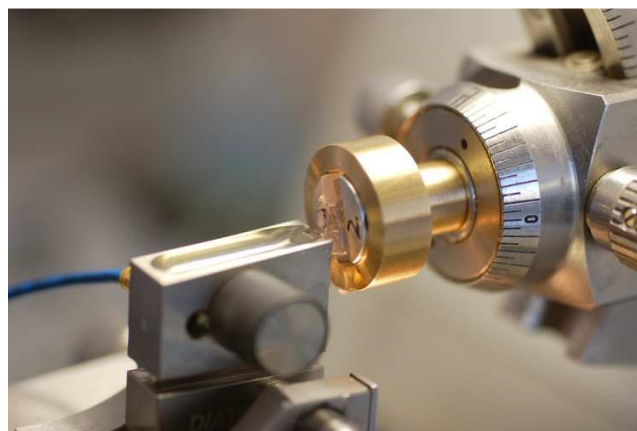


Figure 28: The Ultramicrotome with the special sample fixation tool for nano-flat preparation of the sample.

4.1.3 Liquid Cell

For the AFM measurements a basin had to be designed which should allow to fix the sample holder to heat or cool the basin and inject enzymes separately into the basin. Since the system should be temperature controlled the whole basin should be thermally conductive with a small dead weight. The fact that aluminum is not stable against most solutions led to the use of stainless steel, being a material with high stability against corrosion with an acceptable thermal conductivity. The temperature system

uses a Peltier element to heat or cool the sample. The injection system is rather simple and uses a micro tube and an adapter with a winding for fixation in the basin. The enzymes can then be simply injected by a micro nozzle. Additionally a temperature sensor for the controller unit is implemented, using the same adapter as the injection system. Figure 29 shows the 3D drawing of the basin with the final fabricated prototype form.

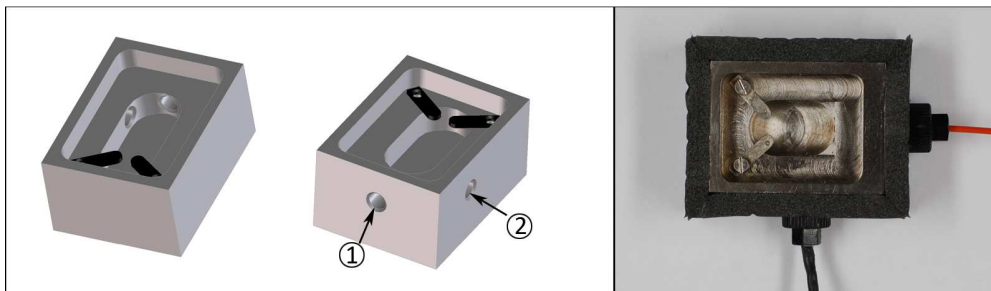


Figure 29: Right: Liquid Cell in 3D drawing. (1): Drilling for Injection system. (2): Drilling for Temperature sensor. Left: LC basin in its fabricated form with injection tube (red) and temperature sensor (black).

4.1.4 Temperature Unit & Stage Fixation

In order to move the LC with the motorized AFM stage a special adapter had to be constructed. The main requirements are a stiff fixation to the stage and the function as a heat sink for cooling or heating the sample with lowest possible overall weight. To do so the height of the components, Peltier element, separation plate (see Figure 31) and the LC had to be carefully considered, since the moveable z-range of the scan head is limited. The LC itself has a rather big height, needed for the complete coverage of the sample with fluid. This and the additional Peltier-element height required the cell to be fixed somehow on the side of the stage. The stage is shown in Figure 30. With this setup, the space between top of the LC and the maximum z-value for the scan head is sufficient.

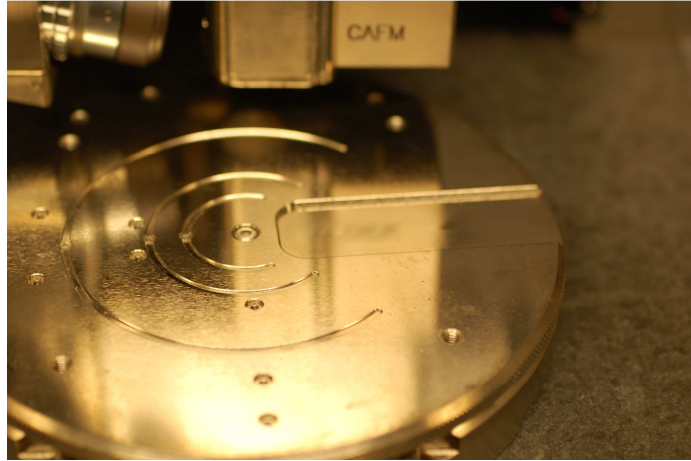


Figure 30: AFM Stage where the LC had to be mounted. Since the total height is too big for direct mounting an adapter for side mounting had to be constructed (see Figure 31).

The requirement to work as a head sink, led to the use of aluminum and brass as materials. The stage fixation and separation plate is fabricated out of brass whereas an additional cooling body is fabricated from aluminum, needed for cooling because a huge amount of heat on the warm side is produced. A couple of tests indicated that for more sophisticated cooling additional water cooling is necessary.

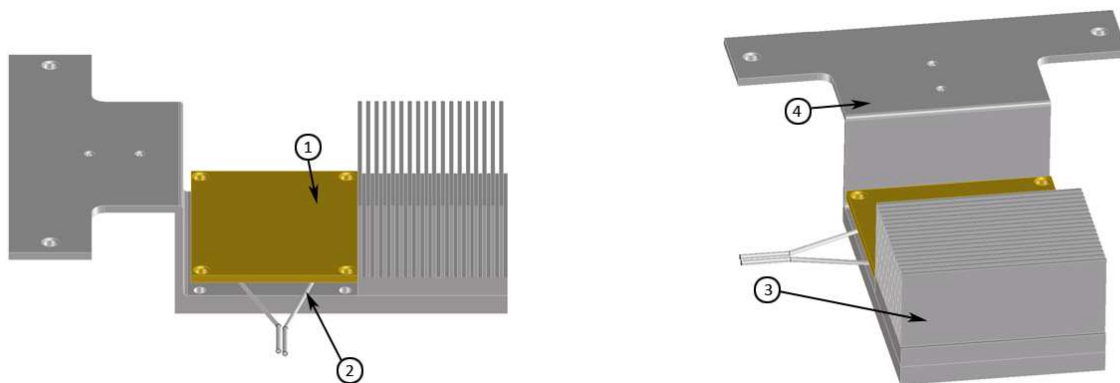


Figure 31: The stage fixation (4) with the setup needed for cooling. (1) Separation plate between LC and Peltier element. (2) Peltier element. (3) Cooling body for as a heat sink.

4.1.5 Complete Setup

The entire setup is shown in Figure 32 by a 3D drawing as well in the fabricated final form. This setup is a first prototype and has still to be improved. The basic principle should be clear and all components work as suggested with one limitation: The bottom part of this fixation is hanging free with no contact. Hence, this is acting as a form of tuning fork and this induces vibrations in the AFM which cannot be

compensated. The simple solution to this problem is, that below the stage fixation foamed plastic stripes have been added which then are in contact with the heavy granite plate. This is sufficient to damp all vibrations.

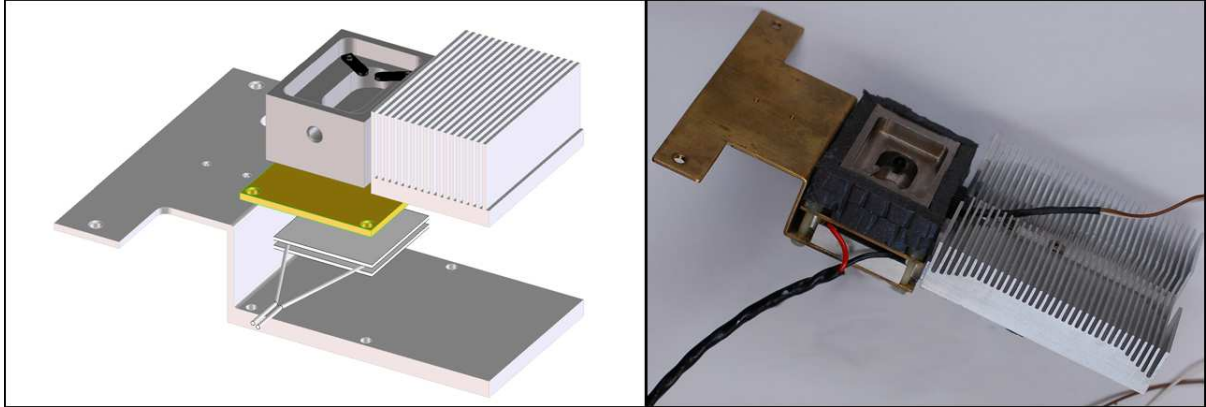


Figure 32: *The complete mechanical setup for the AFM investigations.*

4.2 Electronics

In this part the self-designed temperature controller will be presented. Construction of a temperature controller may seem odd since there are plenty of controllers on the market, but since we had special requirements to the controller we decided to do so. The controller should be specialized on Peltier-elements with a certain power of about 40 W and it should be possible to communicate with the controller via the PC to enable remote control.

4.2.1 Requirements & Specifications

The hardware has to measure the temperature of the LC via a temperature sensor, whereas the temperature sensor has to measure the temperature at least with 0.5° precision. The hardware should then amplify the measurement signal to a value where the ADC unit of the PIC can sample the temperature with highest precision. This signal has than be evaluated by the software and the current to the Peltier-element has to be adapted via another amplifier for high currents. Also the controller should hold the temperature with at least 0.5° precision. A block diagram of this is shown in Figure 33.

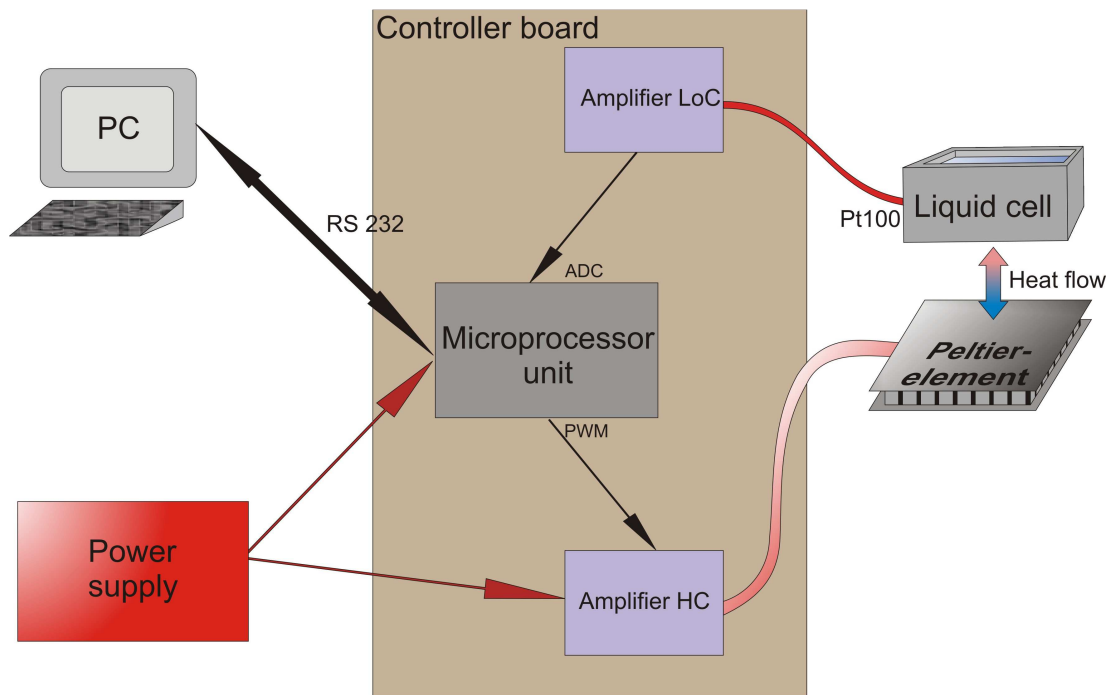


Figure 33: Block diagram of the Controller circuit.

The Peltier-element was chosen to be a 37.9 W in power with maximal voltage and current of (15.7 V / 3.9 A). To be able to operate this Peltier-element, a power supply from Toshiba for notebooks was chosen with 15 V and 5 A. As sensor element a PT100 temperature-sensor was chosen with 1.6x1.2mm in size.

The controller uses a microprocessor (PIC24FJ64GA002) to measure and control temperature in the cell, with a RS232 communication port. The development environment for the software was MPLab V 6.83 with the C-compiler C30, both from microchip as well as the processor.

Electronic simulations during development were done in LTSpice from Linear Technology and connection diagrams were drawn in Tincycad, a Software available under the GNU License.

4.2.2 Controller Board

The controller board is build-on 3 units:

1. the low current (LoC) amplifier for signal amplification of the PT 100 sensor
2. the high current (HC) amplifier for the Peltier element
3. the microcontroller unit

The HC amplifier transforms the low voltage and low current signal from the PWM to 15 V and 3.9 A for the Peltier element. The Power of the Peltier-element is controlled via Pulse Width Modulation (PWM).

The microcontroller unit is composed of all parts which ensure the correct function of the microcontroller as well as the communication port for the RS 232. The LoC amplifier should amplify the signal from a PT100 to a value that the full range of the ADC unit can be used which allows highest accuracy. The amplifier uses a Weatson bridge with an OPV as amplifying element. In Figure 34 to Figure 36 the different connection diagrams are shown.

4.2.2.1 LoC Amplifier

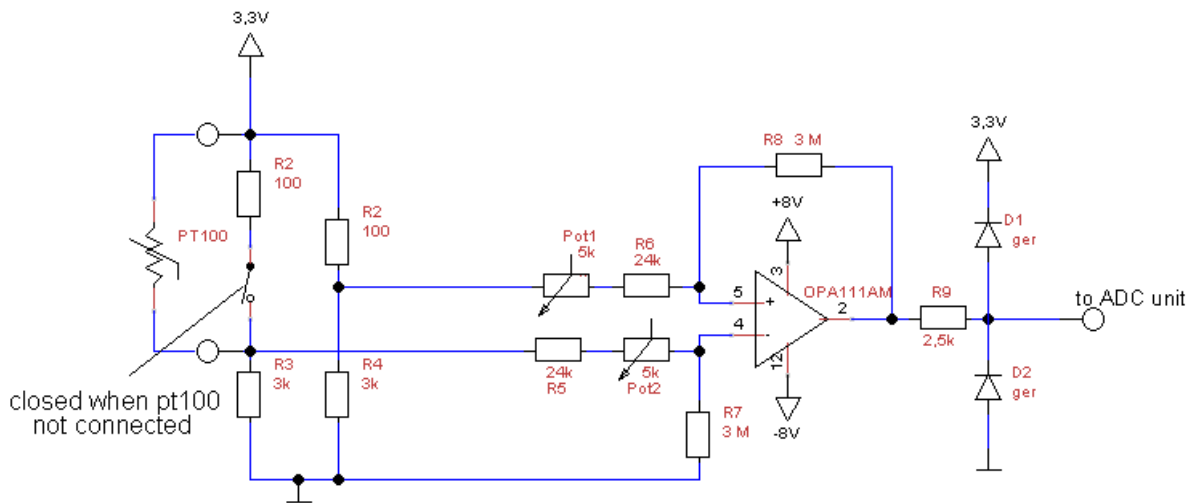


Figure 34: LC Amplifier with Weatson bridge.

This amplifier uses a PT 100 sensor and a Weatson bridge to measure the voltage difference between the potential at the PT100. When 0 °C is present, the PT100 and R2 have the same values and no voltage difference is measurable. At 100 °C the PT 100 has about 138 Ohms which leads to a voltage difference of 55mV at the entrance of the amplifier. The operation regime is in between 0°C to 50°C which gives about 28mV of voltage difference. So an amplifying factor of 120 should be reached which is done by the use of 3 MΩ (R8, R7) and about 24-29kΩ at (Pot1 + R6, Pot2 + R5). The Potentiometers are implemented to change amplification and zero point slightly. The power supply for the OPV comes from the MAX232 chip used for serial communication.

4.2.2.2 Microprocessor Unit

The microprocessor unit contains all components needed for correct operation of the microprocessor as well as all voltage supplies for other components.

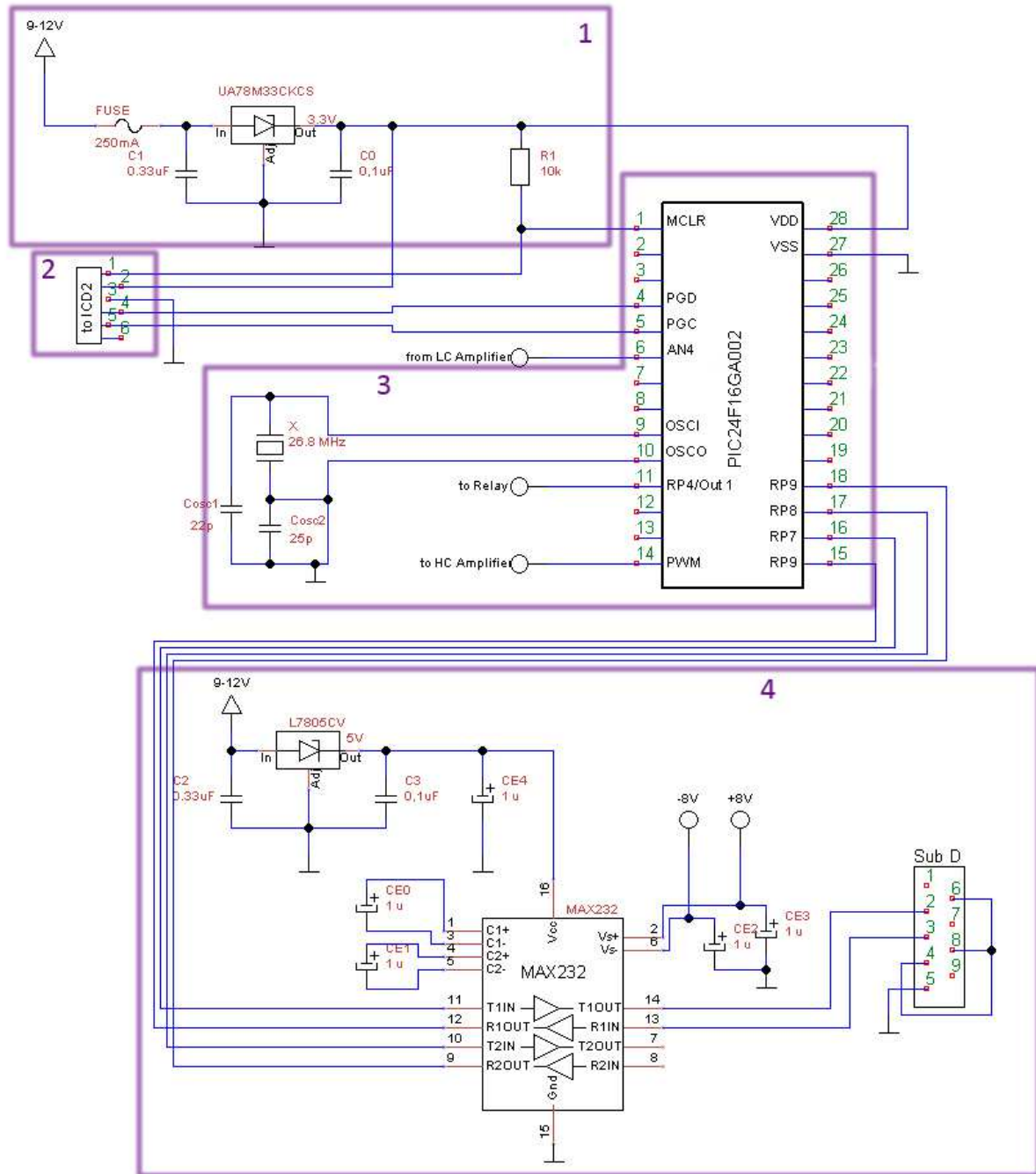


Figure 35: The microcontroller unit with RS 232 port (Description of blocks is below).

The microprocessor unit is basically build on 4 parts:

1. The power supply
2. The connection to the in circuit debugger unit (ICD) which allows direct programming and debugging
3. The oscillator with the PIC
4. The RS 232 unit.

The peltier power is controlled by the PWM unit of the PIC. Port Pin 4 (Out 1) is used to toggle the relay and control the current flow to the peltier. This decides whether the element is heating the cell or cooling it. The controller is driven by a 26.8 Mhz quartz oscillator and uses a 3.3 voltage regulator as input. This low power PIC has no logic level voltages (5V) so another voltage regulator is built in (L7805CV) which drives the MAX 232 chip for serial communication.

4.2.2.3 HC Amplifier

This unit has the function to transform the low voltage input by the PWM to a high current output for the peltier element. Additionally, a current reverse function had to be implemented to switch between heating and cooling. This is done by a relay which is controlled by the PIC.

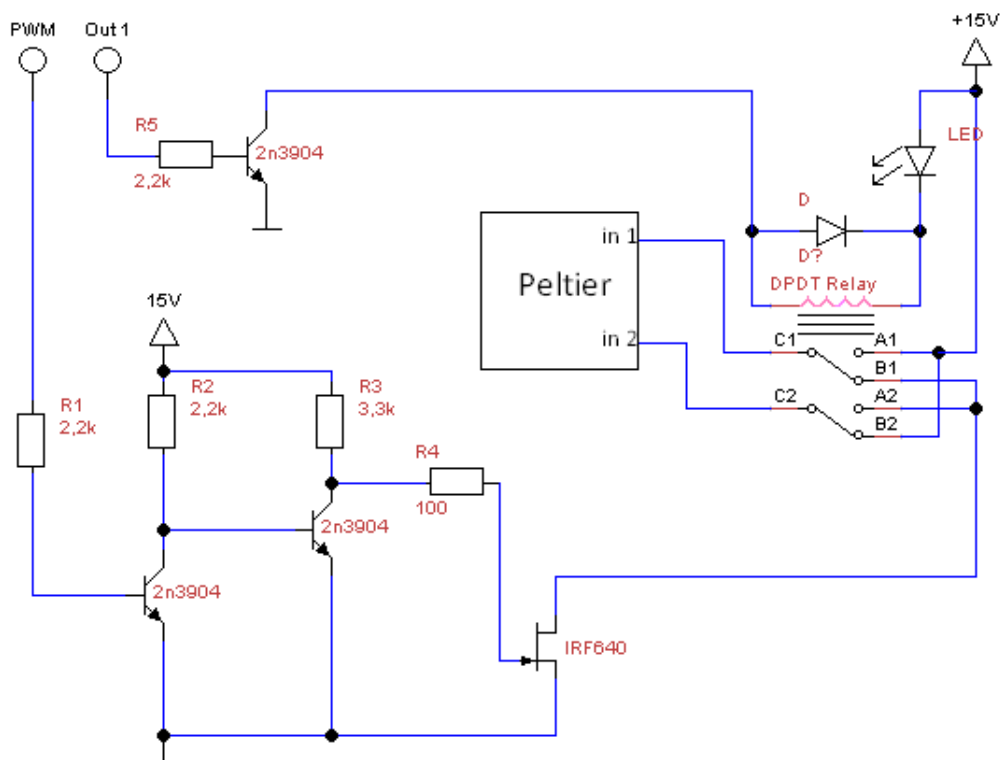


Figure 36: HC amplifier with a high power n-MOS-FET.

The high current amplifier uses two normal npn transistors to drive a high power n-channel MOS-FET which is clocking the 15 V from the power supply to ground in the PWM Waveform. Another npn is used to drive the Double Pole Double Throw (DPDT) relay. When the led glows, the current is flowing in the other direction and this is indicating that the controller is currently cooling.

4.3 Software

This algorithm was designed to operate the controller board and the temperature stage. First there was a lot of trial and error to finally get the board to its final stage and also the algorithm was rewritten for optimization.

To communicate with the board the platform HyperTerminal was chosen. This is the reason why the program is rather big since the communication has to be done by the PIC and not the PC. The PC is in this case the slave which is waiting for commands from the processor.

Figure 37 shows the flow charts of the main program and functions. The program is added on a CD in the back side of this diploma thesis.

4.3.1 Main Program

In the main routine, first all variables are initialized and the different functions of the PIC are started, like the serial communication port (UART) or the analog-digital converter (ADC). After this the routine enters an endless loop which can only be left by pressing the reset button on the controller board. In the endless loop it is checked if the variable cooling is set. This can only be done by first entering the function Menu() which is first reached when any button on the keyboard is pressed. After this the cooling routine can start and it is checked if the Peltier has to cool or heat the LC. This is controlled by the Pin RP4 or Out 1 (see Figure 35). The PWM duty cycle is set in the subroutine PI_control(..) whereas controlling can be stopped by pressing any key. If nothing is done and cooling is false the PIC sends continuously the temperature to the PC.

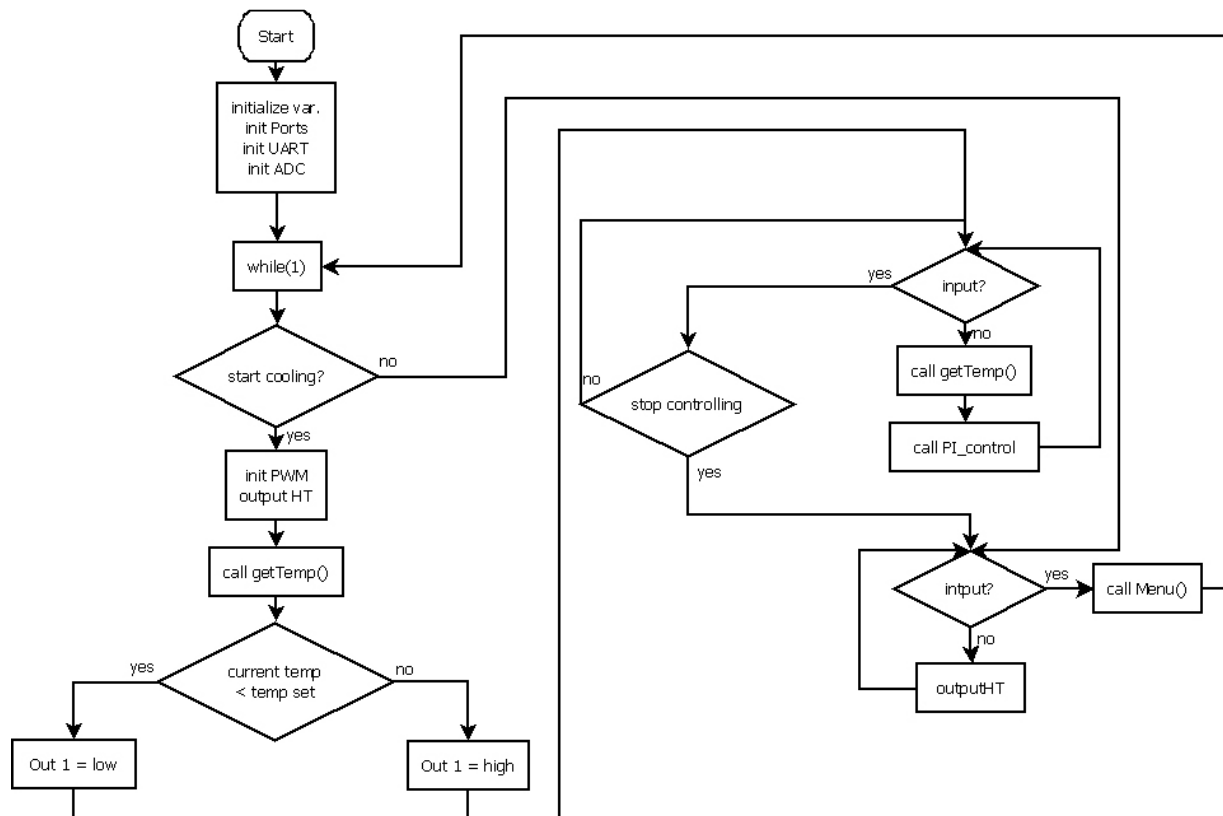


Figure 37: Main routine.

4.3.2 Menu

In this routine the user can enter a specific command to change for instance the temperature setting. This temperature is then the new temperature point, which the controller tries to reach. In typing a command always the character “-” has to be in front to explicitly mark the following character as a command. With “-h” the user gets a list of commands which can be used. The menu routine is leaved when dataready is set to one. In the case that “-t” is typed, the program set after a correct input e.g. 20 for 20°C the variable cooling to one and the controlling process starts in the main routine (see 4.3.1)

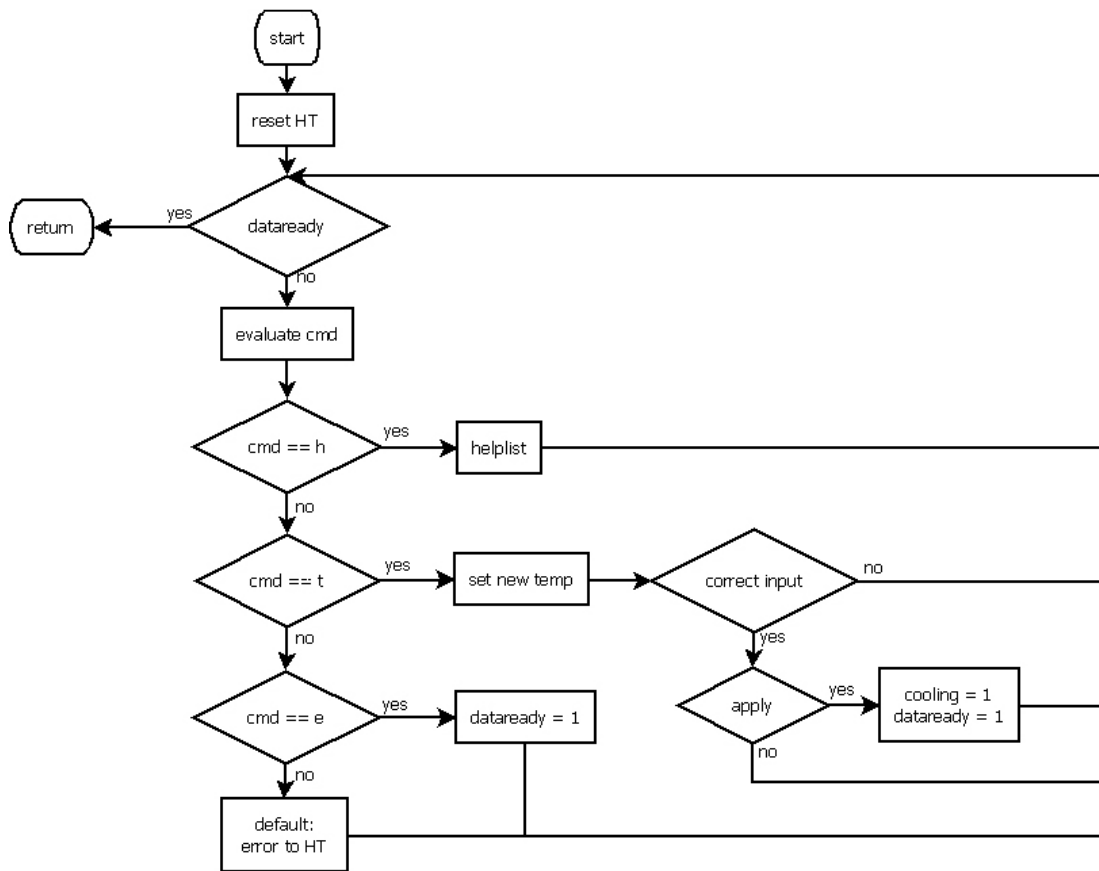


Figure 38: The menu routine.

4.3.3 GetTemp

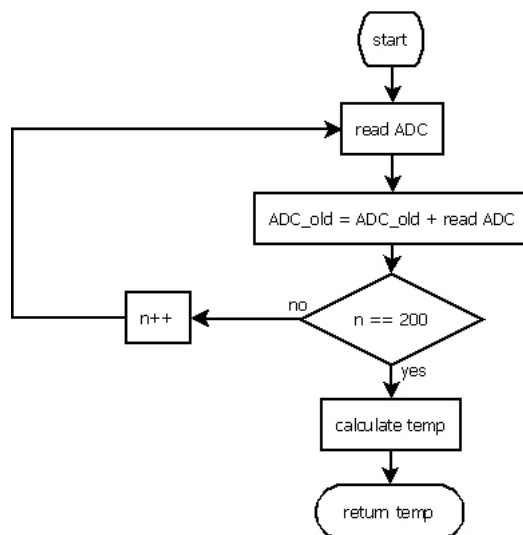


Figure 39: The get temperature routine

This routine samples the analog input on the analog digital converter and calculates the temperature. In the routine a *for* loop over 200 iterations is used to overcome noise at the input. After this the temperature is calculated via a calibration curve.

4.3.4 PI Control

This subroutine is simply a PID controller (Proportional/Integral/Differential) which uses equation (7) to set the new duty cycle for the PWM. The routine has a mechanism to hold the Integral part below a certain limit. Otherwise the controller starts to get unstable. The controller has only been optimized via trial and error. All information about PID-controllers have been taken from [23]

$$duty\ cycle = K_p * e + e_{sum} * K_i * T_a + \frac{K_d}{T_a} * (e - e_{alt}) \quad (7)$$

Here K_p , K_i and K_d are the controlling parameters for the proportional, the integral and the differential part. e is the difference between current temperature and the temperature setting and e_{sum} is the sum over these differences or better the integration over a period of time when T_a , the sample time, is added. This is basically the algorithm which is easy to use.

It has to be mentioned that the complete program is much more detailed and is not discussed in this thesis. This chapter should give only an idea how the program has been developed and be a guiding help for later applications and improvements which definitely have to be done. Also the algorithm is not yet perfect and with mechanical improvements also the controlling speed and accuracy can be improved.

5 The Substrate

Since the experiments are done via AFM, surface properties play a major role. The most important property is definitely the flatness of the substrate. Firstly because small variations during degradation can be only recognized if the substrate is flat and secondly, there is a low accessible z-range of about 7 μm during measurement.

Cellulases need a cellulosic surface to act plus for the experiments the substrate should be reproducible. Cellulose in its natural form shows unfavorable properties (see chapter 2.1.1), thus a model substrate had to be designed.

Dohr and coworkers produced a substrate based on [24] and [25], showing promising behavior for our experiment. The process of production and preparation will be discussed in this chapter.

5.1 Fabrication

Kadokawa et al (2008) [24] used the IL 1-Butyl-3-Methylimidazolium chloride (BMIMCl) to dissolve Avicel cellulose. As already mentioned in chapter 2.1.3 the ionic liquid BMIMCl is capable of dissolving cellulose. The liquid can dissolve cellulose up to 8-15 wt. %, if heated and steered. The solubility limit depends on the temperature and steering method as well on the humidity. Other groups claimed [13] that cellulose contents up to 25% in the solution are possible when the IL is heated via microwaves. Nevertheless, we decided to use a content of 15% cellulose which is close to the solubility limit for this system when heated conventionally.

The production is rather simple. The IL is heated to 100° C and steered with a magnetic stick, whereas crystalline cellulose is added slowly to the glass petri dish. This usually is done for about an hour. After that, all of the cellulose should be dissolved and steering is continued for 24 h to reach a point where the liquid is homogeneous. At that point the gel is further denoted as primary gel (PG) where a small drop is taken and brought onto a glass slide. Immediately afterwards another glass slide is pressed from the top which forms the droplet to a circular shape. Two smaller glass slides act as a spacer (see Figure 40) in between to provide always the same thickness. The IL is held in this state for 1 week, where most of the IL leaves the sample. Such gels are further denoted as secondary gel (SG), still containing some content of IL. However, since this IL is highly unwanted in the experiments another drying procedure had to be applied.

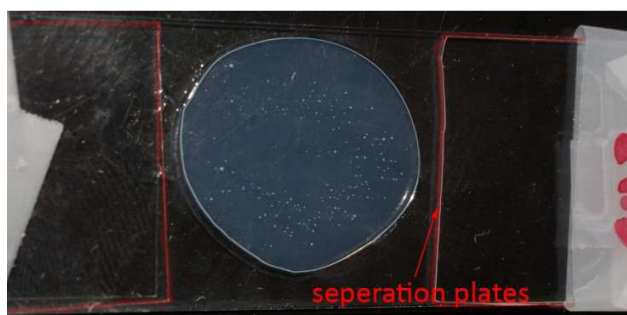


Figure 40: GL between glass plates.

Dohr and coworkers tried a variety of drying procedures with ethanol and acetone, also used by Kadokawa et al. (2008) [24], to reduce the content of IL in the sample to a minimum. First a direct solvent exchange with ethanol was applied, with the result that only the border regions of the gel lost all their IL. In the center of the SG IL residues had been found, which required a different drying procedure. They first reduced the thickness of the sample by using less spacer glass plates. Furthermore, the procedure was changed from direct to fractional solvent exchange, as often used for biological samples. Table 3 shows the precise procedure of this method.

Table 3: Fractioned drying procedure.

Ethanol concentration	Fragment exchange time
30 % EtOH	15 min
50 % EtOH	15 min
70 % EtOH	30 min
70 % EtOH	30 min
80 % EtOH	30 min
90 % EtOH	30 min
100 % EtOH	30 min
100 % EtOH	30 min

This approach led to significant better results, without any visible crystalline residues and encapsulations. The observed fragments are hard and milky (see Figure 41).



Figure 41: Dried cellulose fragments.

To get evidence that the IL is entirely removed, simultaneous thermal analysis (STA) and mass spectroscopy was performed. STA as a combined method of TGA (Thermogravimetric analysis) and DSC (Differential scanning calorimetry) and was performed with a *Netzsch STA 449C (Netzsch Gerätebau GmbH, Selb, Germany)* with a heating rate of 10°C/min under a constant helium flow (50.0 mL min⁻¹) [22].

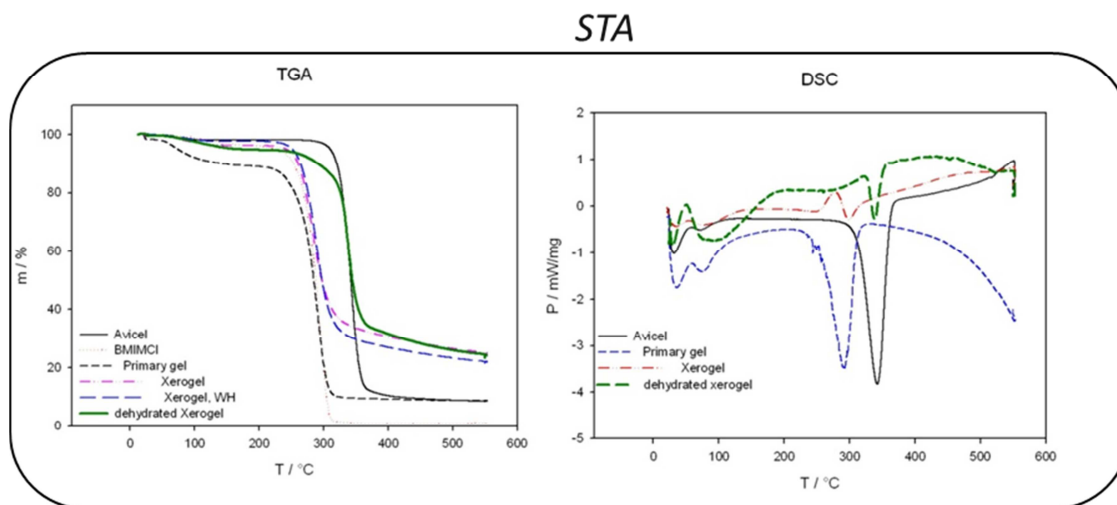
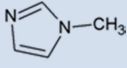
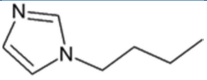


Figure 42: Results of the simultaneous thermal analysis. Left: Thermogravimetric analysis TGA. Right: Differential scanning calorimetry

Both TGA and DSC showed that the gel fragments are comparable to the Avicel cellulose. The Avicel curve (black) is similar to the dehydrated gel curve (green). The evaporation starts at the same point and the phase change is also similar for DSC. All other curves are done on intermediate products of the process, such as the PG, the Xerogel or Secondary Gel (SG) and on pure BMIMCl. Additional mass spectroscopy (MS) was done to search for the fragments of the IL. MS results are given in Table 4, showing that in the finished cellulose substrate (CS) IL content is below detection limit.

Table 4: Mass spectroscopy results on the fragments of BMIMCl. (+) shows that a signal was observed. (-) indicates that the amount is below the detection limit.

m/z	fragment	chem. name	M_r [g/mol]	Avicel	BMIMCl	PG	SC	CS
82		1-methylimidazole	82.1	-	+	+	+	-
124		1-butylimidazole	124.2	-	+	+	-	-

5.2 Preparation of AFM Suited Samples

The finally prepared cellulose fragments are free of any detectable fragments of the IL and ready for final preparation. A schematic illustration of the preparation is given in Figure 43. The fragments are embedded in epoxy resin (*Specifix-40 from Struers*) with a drying duration of 4 hours at 40°C. After this the samples are fixated in the special sample holder (Figure 26) and a precut is done by razor blades. With this, dispensable epoxy resin on top is removed, which alleviates the cutting procedure. In the next

step, the sample is put into buffer solution for swelling to achieve a volumetric constant state of the cellulose [3]. To prevent volumetric changes in the liquid cell, this procedure was defined with one hour swelling duration, which proved to be sufficient for preparation. The used ultramicrotome is a Leica Ultracut UCT with an oscillating knife (ultrasonic 35°) [3].

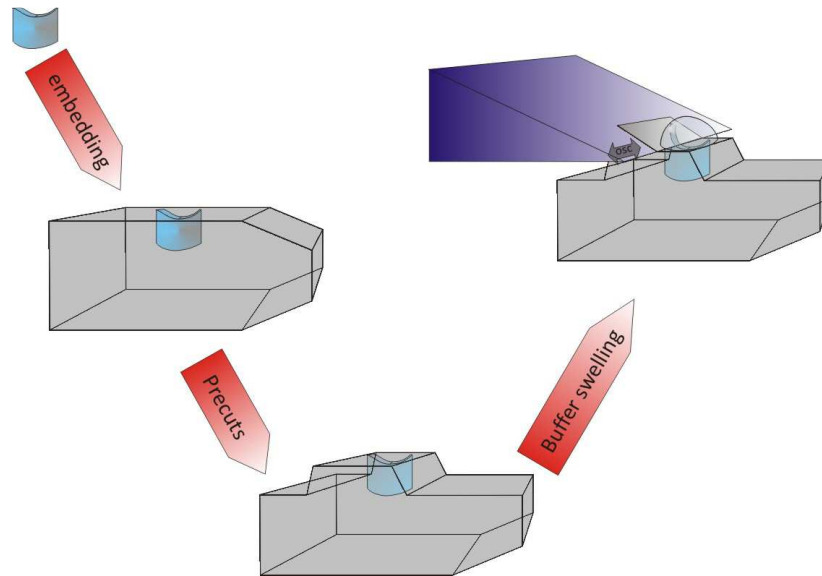


Figure 43: Preparation procedure of the cellulose sample.

The final cut is still done in moist conditions to keep the sample saturated with buffer solution. Optical microscopy of the sample is used to see if the results are satisfying. Otherwise the final cut is repeated until the results are satisfying. A typical and good cross-section is shown in Figure 44.

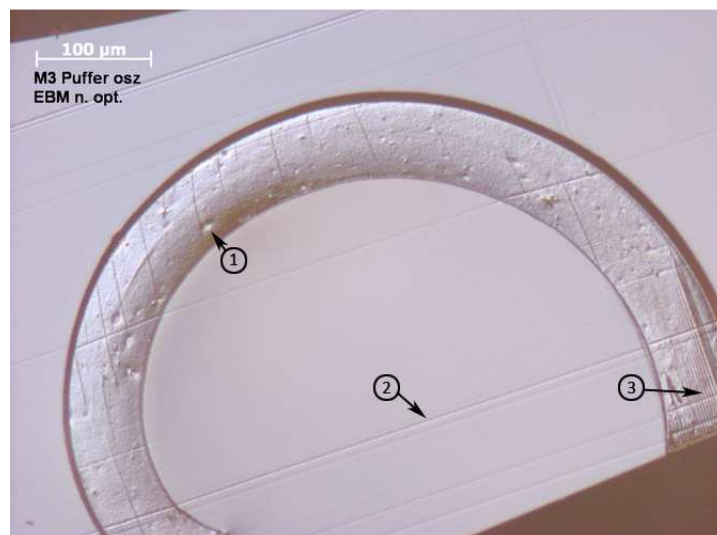


Figure 44: Cross-section of a typical sample. (1) Avicel residues which haven't been dissolved completely. (2) knife striations (knife is damaged and produces striations and scratches). (3) knife shatter (appearing on hard samples when the knife doesn't move smoothly).

A sample as shown in Figure 44 can then be used for analysis in the AFM, as shown in Figure 45 by a 20 x 20 μm height overview.

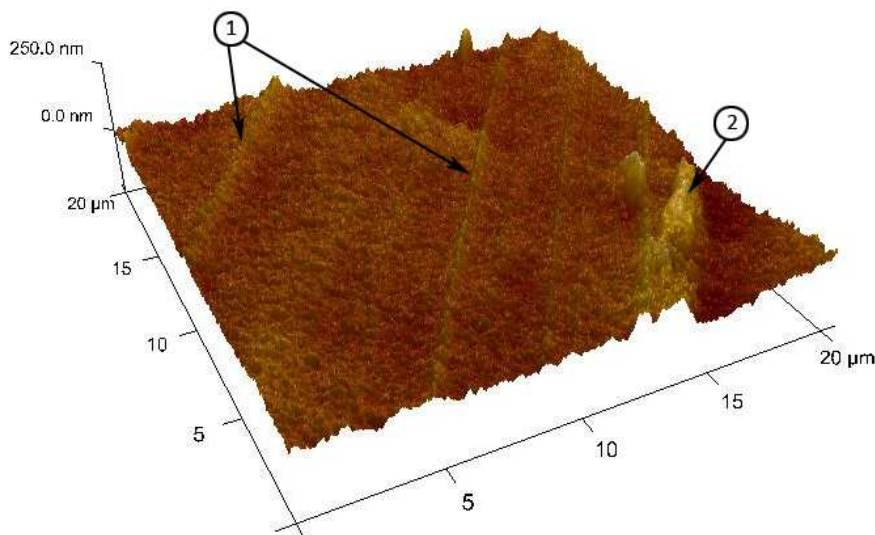


Figure 45: AFM Image of a CS cross-section. The root mean square is about 15 nm excluding the crystalline Avicel residue (2). (1) Knife marks.

Dohr and coworkers achieved RMS roughness of less than 10 nm in contrary to our 15 nm, whereas the reason for this slightly increased results are unclear yet. It may be the fabrication process, which is critical to humidity and ambient temperature. The sample seems to be a bit softer which leads to more problems during cutting, thus producing higher height-features on the sample. It is believed that the knife smears a little bit over the sample leading to more artifacts.

6 Liquid Cell Implementation

LC and constructed elements have not been used before at the institute, hence, experience and knowledge were widely missing at the beginning. Thus, it was necessary to first make measurements with the cell on different and defined substrates to get a better understanding of the peculiarities of this technique. This chapter should be guidance for other operators at the AFM, to improve the understanding of the L-AFM, with important rules for successive operation under aqueous conditions.

6.1 Setup

The setup for L-AFM is simply a special probe holder (see Figure 46) which is specially designed for liquid operation. It is not allowed to use the normal probe holder since this would cause water and humidity flow to the piezos of the scan head, further leading to a short circuit and destroying of the piezo electronic.



Figure 46: The probe holder for liquid applications. (1) The fixation and trench for the probe. (2) Fixation spring. (3) Electronic circuit and fixation contacts. (4) Glass window for the optical laser. The shiny red rectangle is the build in piezo for cantilever oscillation.

This plastic probe holder contains a piezo for the direct cantilever excitation in contrast to old liquid probe holders, where the z-piezo of the scan head induces oscillation by fluid excitation. This works in a way that the z-piezo is acting on the fluid as oscillating medium, whereas the cantilever is passive and excited due to the fluid oscillations. This gives a more complex spectrum and a higher difficulty in finding the ideal measurement resonance.

Z-piezo excitation was tried several times with the result that it is possible to use this technique, however, it is not recommended since also the piezo in the probe holder is excited and the oscillations may interact or damp each other. To use z-piezo excitation, the option z-modulation in the parameter view must be used.

The probe holder is mounted in the same way as the normal probe holder (see Figure 47). Additionally, a protection can be mounted on top of the probe holder to prevent spill damage of the scan head. However, in normal operation and with little precautions this isn't required.

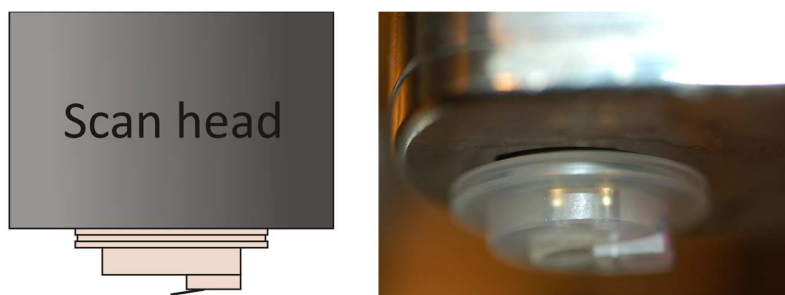


Figure 47: The scan head with the mounted liquid probe holder (right) and a schematic side view (left).

This and a petrie dish is basically all what is needed, if liquid operation is aspired. The probe can, if sufficiently small and flat imaged under a droplet of liquid. This has been used in the first investigations with this new setup and technique.

6.2 First Investigations

A glass petrie dish was chosen to act as a container for the liquid and as sample at the same time. The scan head with the tip approached the glass surface of the petrie dish and a drop of water was added. An important fact now is, that when the droplet is entered, the optical path length of light changes, which affects the laser light as well as the optical focus of the build in microscope. So this has to be considered when a sample is watched in liquid conditions. The optical focus of the AFM under gaseous conditions lies at 1 mm above the sample. When using the AFM in liquid this focus is now lying at 1.3mm, hence it is a problem if the automatic approach is used which moves about 1mm towards the sample, when starting a measurement. Thus the optical focus has to be searched and afterwards the tip has to be moved 300 μm towards the surface and away from the focus. This has to be done after the tip is newly focused in the liquid. Furthermore, the laser beam also has to be adjusted again. Summarizing this, following steps must be done when measuring under liquid conditions:

- Use the liquid probe holder only
- Refocus the tip when immersed in liquid
- Readjust the laser and detector
- Focus the surface and move 300 μm below this point

The glass petrie dish was not modified by any means during first investigations. It was cleaned with ethanol and a droplet of deionized water was put onto the glass. As tip a standard rectangular soft cantilever from Olympus probes (Type: OMCL-AC240-TS) was used with a stiffness of ~ 2 N/m. This proved to work for a certain period of time. The tip works well and images can be taken without any problems but after some time the measurement gets unstable and the tracking is lost. In Figure 48 the surface of the glass petrie dish can be seen with a scratch going from the right lower corner to the left upper one.

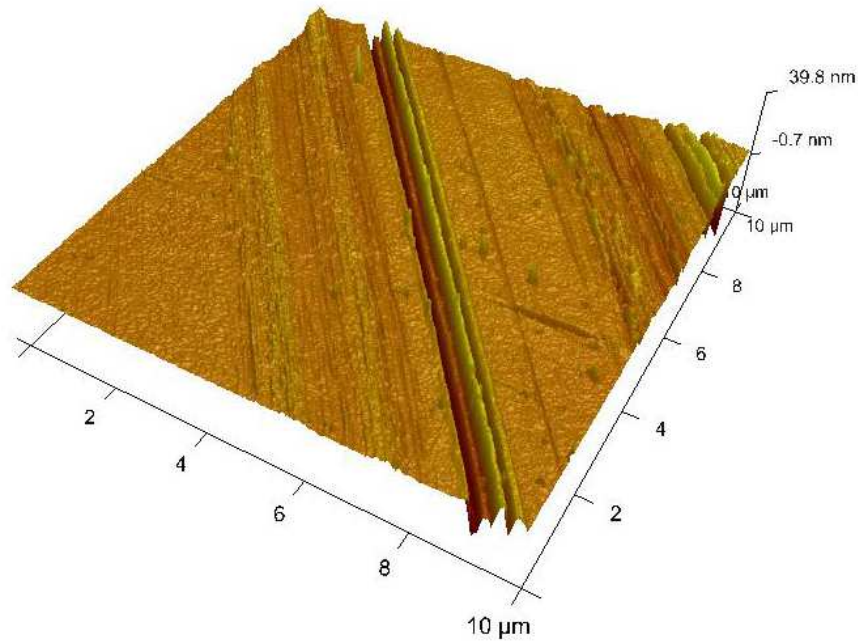


Figure 48: Glass surface of a standard petrie dish under a droplet of liquid.

The phase image shows a slightly steady shift of the phase to more positive values during time. This is a typical indication for the instability of the probe (see Figure 49). This usually happens when an inappropriate tip is chosen. These first experiments revealed that tip selection is crucial for stable operation in liquid conditions.

However, there is another problem with this investigation. The used liquid was deionized water, lacking any ions capable to screen electrostatic interaction between probe and sample leading to instability. It is recommended by the supplier of the liquid probe holder to never use deionized water. Instead, buffer solution should be used or in any case normal water.

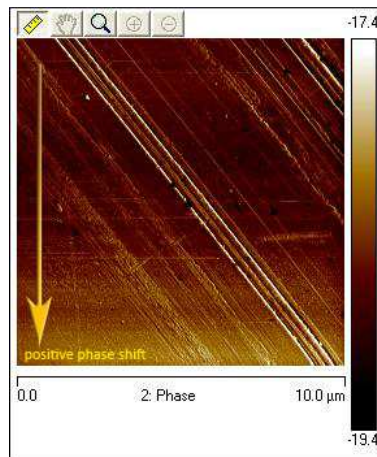


Figure 49: Phase image of the glass surface with a slightly increasing phase signal from top to bottom.

6.3 Tip Considerations

As already mentioned, cantilever selection seem to be very important for the liquid operation. Therefore, we put some effort into this topic and tested different cantilevers from different suppliers. Cantilevers are fabricated from different materials, like silicon or silicon nitride (see 2.2.1.1), often also containing a reflective gold backside and fabricated with different shapes, mainly rectangular and triangular cantilevers. The cantilevers for liquids should be not too stiff (good rule of thumb is 0.1 N/m) and most of them are triangular leading to better behavior when oscillated. When using contact mode AFM, cantilevers with even lower stiffness can be used (0.01 N/m). It appeared for this thesis that tips from Olympus of the type: TR400PSA work best for this application. Especially, when looking at cellulose substrates the results are very good and reproducible. The cantilevers of this type have shown good stability and behavior.

It may be necessary to search for new cantilevers when using the liquid AFM in another application but as a rule of thumb soft cantilevers seem to work good so far. We also tried to measure with stiffer cantilevers and different types but the results were never as good as for the TR400PSA cantilevers. Cantilevers of the type RC800PSA have proved to work in buffer solution well, but problems occur when enzymes are added. Whether this is a result of the enzymes or the surface change of the cellulose substrate couldn't be determined. To show the good compatibility of these tips with aqueous environments a standard sample was watched first in gaseous conditions and second in liquid. (see Figure 50 & Figure 51).

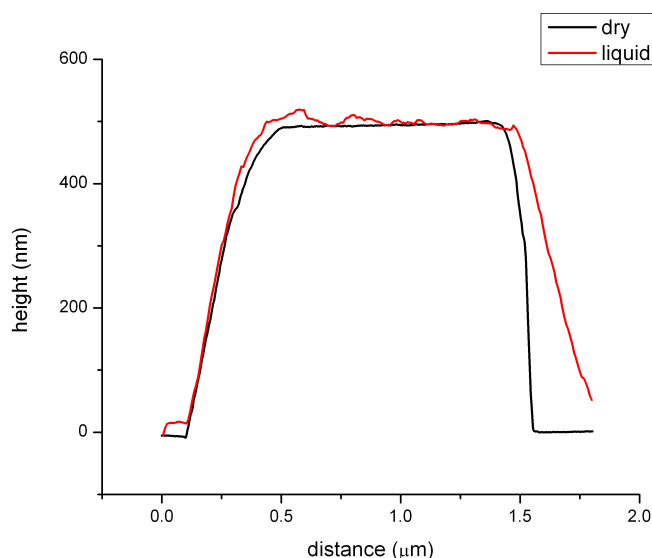


Figure 50: Sections from a standard sample. Slight differences are due to solvent residues and the different measuring positions.

This experiment showed that both techniques bring similar results on a standard sample, nevertheless, imaging position is different due to changing the probe holder and repositioning. The phase of this sample show different images, but it seems clear that solvent residues are looking different in gaseous conditions then in aqueous.

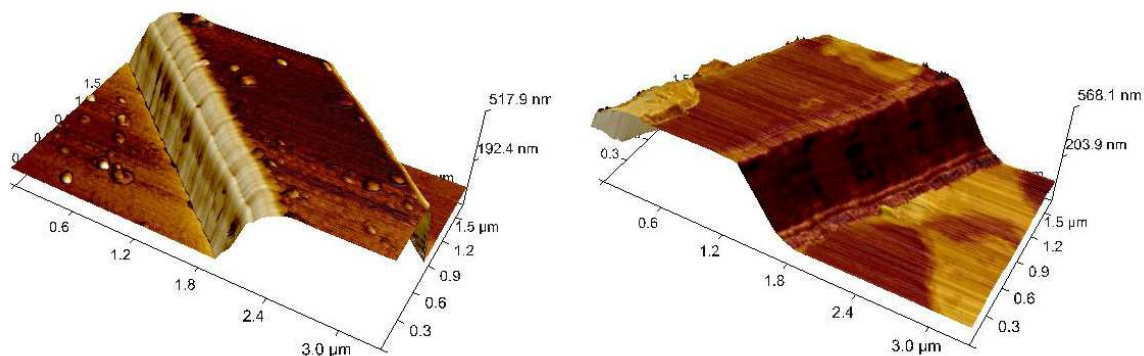


Figure 51: Standard sample in dry (right) and fluid (left) conditions. The height image is colored with phase information.

6.3.1 Conclusion

The investigations showed that the measurement in liquid shows similar and good results with different phase images. The best type of cantilever we found so far was the TR400PSA from Olympus Probes. The TR400PSA is build up from to triangular cantilever whereas the smaller one can be used for liquid measurements. The longer cantilever has a too low stiffness to work with liquid in AC Mode, but can be used well in contact mode. To operate the tip in AM-AFM a measurement frequency must be chosen, which turned out to be challenging in liquid conditions. Normal operations frequencies and resonances lie in the range of 10 kHz in liquid. This turned out to work not for our LC and we found, that measurement conditions are optimal at frequencies around 34 kHz which is the 3rd mechanical harmonic.

7 Biological Experiments

All parts have been described and testes extensively prior to the following experiments. The optimal cantilever has been found and the main experiment could be started. This chapter is describing all experiments done by me and my colleague Manuel Eibinger from the institute of Biotechnology and Bioprocess-Technology. He prepared all enzyme solutions for the different experiments and joined at all experiments. He also did controlling and contributing chemical analyses of the degradation process and laid the fundament for the analysis of the AFM data.

7.1 Experimental Outline & Setup

The experiments have been done on an AFM of the following type:

AFM Specifications

System	Dimension 3100 (Digital Instruments, VEECO)
Scan head	Hybrid X-Y-Z closed loop
Controller	Nanoscope 4a
Possible sample dimension	about 150 mm (x,y) and 15 mm (z)
Stage	motorized x-y stage
Stage accuracy	$\pm 3 \mu\text{m}$ from each position, $\sim 1 \mu\text{m}$ unidirectional
Maximum lateral scan area	100x100 μm
Maximum vertical scan area	about 6.7 μm
Maximum number of pixel	hor. 4096 /ver. 1024
Resolution	< 3nm lateral (Tapping/Phase mode) < 0.2 nm vertical

For the experiments, the mechanical setup for liquid measurements was mounted on the stage and the sample was put into the LC. In all cases buffer solution was filled in before the sample was added to the LC to prevent drying of the cellulose substrate. Afterwards the setup was positioned below the tip and the measurement could start. The tip approach procedure is described in chapter 6.2.

The measurement itself was performed in an air conditioned room at 22° Celsius. Sample and enzyme solution were usually cooled at 4° C before the measurement, so all components for the measurement have been held at room temperature for a few minutes to led them assimilate to the temperature.

First measurements were done without any enzymes in the cell to find a spot with adequate morphological properties. In the first measurements it was detected that not all Avicel particles have been dissolved by the dissolving process. However, this is probably a result of our decision to go to a content of 15% cellulose in the IL, which is the dissolution limit for this system. This was found to be advantageous for the measurement, as this can act as a surface marker for the measurement. These large crystalline parts are degraded very slowly during enzyme attack. Therefore, this crystallites show the surface position before enzyme incubation.

The enzymes where injected after several reference images with a micropipette because the injection system was missing. The enzyme solution which was usually a few μl was injected carefully during the measurements at the side of the cell. This was usually visible in the AFM Image and so the precise time of injection could be recorded in the image.

Cooling or heating was not implemented for these first measurements, because the system is in a prototype state and has to be modified to work correctly. Hence, all measurements have been done at the room temperature of 22°C (air-conditioned).

To support our measurements and vice versa, Manuel Eibinger and Patricia Bubner did biochemical measurements on the substrate and the enzymes. They mainly used spectroscopic tests, as for instance the DNS-Test, to follow the degradation process via observing the amount of saccharides or oligosaccharides released by the cellulases. In this thesis only the supporting results of these measurements are presented.

7.1.1 Working Procedure

The following steps were always performed when measurements with enzymes were done. First the substrate was put into the LC, where the LC was prefilled with buffer solution. The CS was quickly added with tweezers to prevent a drying of the substrate. This was followed by the aligning procedure of the AFM and the approach of the tip to the surface. Following this procedure an adequate measurement spot was searched with the requirements, that a crystalline residue should be present as marker. After collecting a few reference images the enzyme was injected at the beginning of a picture via a micropipette. The amount of enzyme solution added was typically a few μl , which doesn't change the liquid volume dramatically (usually 4 ml). After this, a capture movie operation recorded subsequent pictures of the degradation process. So summarizing following steps were performed:

- Filling the LC with buffer solution
- Adding the substrate to the LC
- Aligning the AFM for the measurement
- Searching for an adequate measurement position (crystalline residue & flatness)
- Making reference images of the relevant spot
- Adding the enzyme via a pipette
- Taking pictures during degradation continuously (usually capture movie)

To get an insight in both, the low resolution imaging with a large overview (μm) and the high resolution imaging with nm resolution, usually two observation series have typically been done.

7.2 Supernatant of *Trichoderma Reesei*

To get clear results at the temperature of 22 °C we decided to use the highest concentration of enzymes used by Dohr and coworkers. They had an incubation chamber and used a temperature of about 50 °C. This would mean that the reaction is working at a speed of about 8 times faster as at 22°. Dohr and coworkers observed at this concentration strong RMS change after about 10 to 30 min which would mean 80 to 240 min in our case.

7.2.1 Overview Imaging

In this experiment a crystalline residue was found on the sample where a picture size of 5 μm was chosen. Figure 52 shows the surface without enzymes present in the solution.

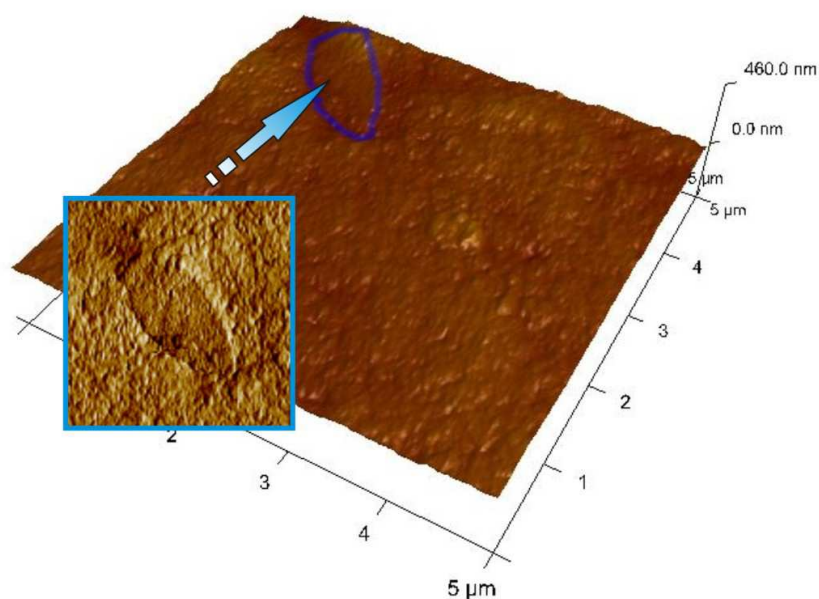


Figure 52: The substrate in 3D and the corresponding phase image. The blue arrow and blue border indicates the crystalline residue. It is clearly visible in the phase image (inset).

The crystalline residue is clearly visible and acts as a surface marker due to our observation that the crystalline residue is degraded way slower than surrounding multiphase cellulose substrate. After we took the above shown reference image, the measurement could start and we added 0.18 mg enzyme solution per 5 mg substrate. This is the highest concentration used by Dohr and coworkers [3]. Figure 53 shows the results of this measurement over a time

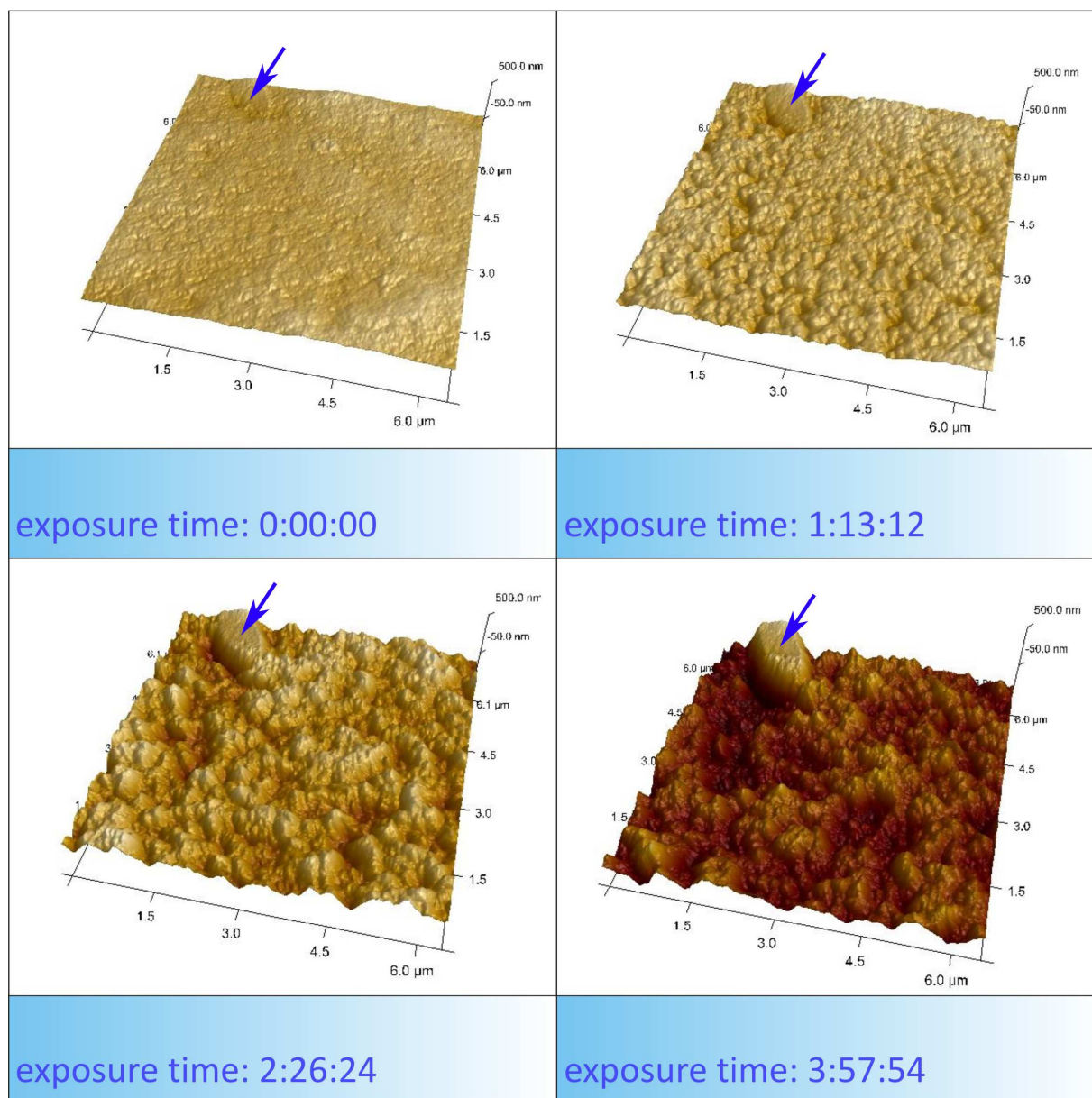


Figure 53: The results of the degradation process over a time of 4 hours with the supernatant of the fungus *Trichoderma Reesei*.

In Figure 53 it is obvious that the surface suffers massive degradation by the enzyme system. It is visible that the substrate which is containing mostly amorphous cellulosic material is degraded way faster than the crystalline residue as indicated by the arrow. The degradation can also be followed by looking at a section profile over the crystalline cellulose particle (see Figure 54).

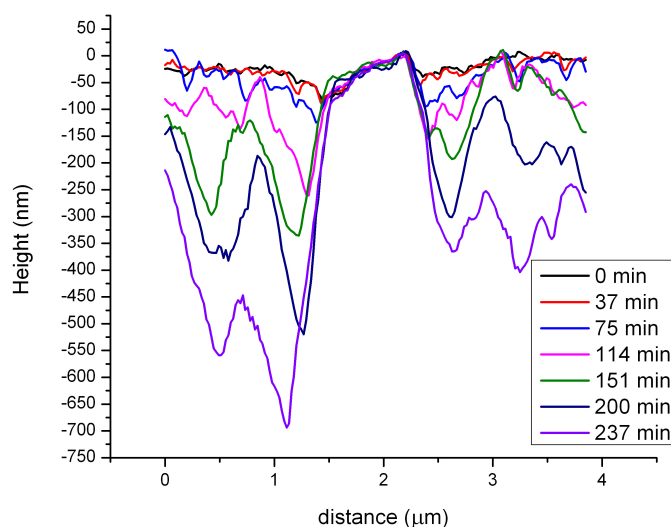


Figure 54: Chapter profiles after certain incubation time. It shows that after about 4 hours 300-400 nm substrate is degraded by the enzymes.

By looking at the sections one can see that a local degradation of about 300 nm over a time period of 4 h is achieved. The sections show also, that the residue is not really attacked by the enzyme system in this time. Now by taking a look at the biochemical experiments, these results are in good comparison to the AFM-Pictures. The supernatant with the notation MG 2279 showed about 90% conversion in 80 h (see Figure 55). So a high conversion is given in the biochemical experiments too. Since timescales and temperatures are different, a direct comparison between these results is difficult. Nevertheless, both results showed strong hydrolysis activity on our multiphase substrate.

Hydrolysis rate and evolution may be visible in an RMS evolution which was performed for the above substrate and shown in Figure 56. Looking at the data, the RMS starts to increase about an hour after enzyme incubation. We attribute this delay time to diffusion of the enzymes because the enzyme solution is added about 1 cm away from the sample and diffusion is low at 22 °C, delaying the enzymatic attack.

While, for this case, this may be a good way to see the starting point of hydrolysis, RMS investigations could lead to misinterpretations when hydrolysis is equivalent on each point of the substrate. In this case no RMS increase would be visible, although hydrolysis is strong. As for this case the multiphase nature of the substrate seems to induce different velocities in degradation (as already observed by [3]), thus RMS considerations seems to be reasonably and reliable.

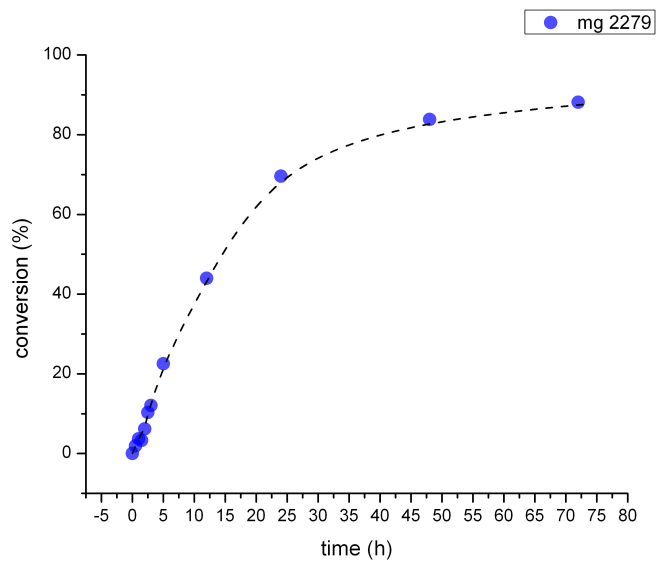


Figure 55: Biochemical hydrolysis experiment with the supernatant on the cellulose substrate. The supernatant is referred to as mg 2279.

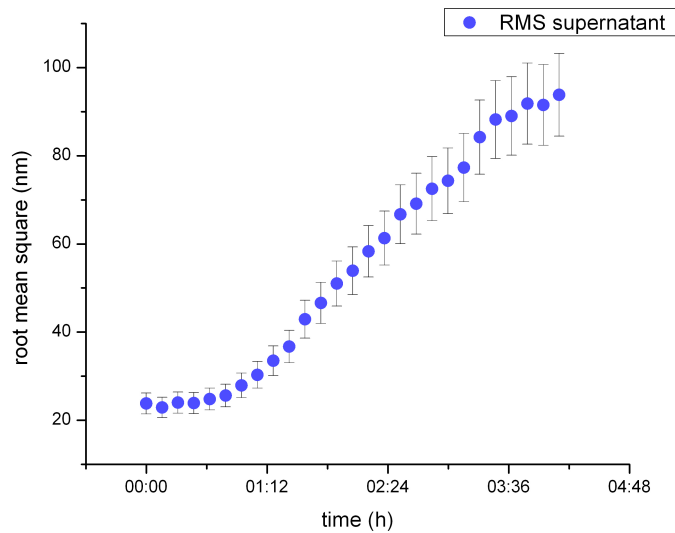


Figure 56: RMS evolution. Hydrolysis seems to start at about 1 hour after incubation rising constantly. Deep trenches and holes are formed during this period as a result of different degradation velocities. The error was estimated with 10% coming from drift problems and flattening errors.

7.2.2 High Resolution Imaging

As already mentioned, we also wanted to see what is happening on the nano-scale. After a few measurements we found that $500 \times 500 \text{ nm}^2$ scan areas are possible in liquid and show well resolved features. What is shown in Figure 57 is a 3D image of our measurement area, where we found clearly visible microfibrils with diameters of about 10 nm as indicated by the arrows.

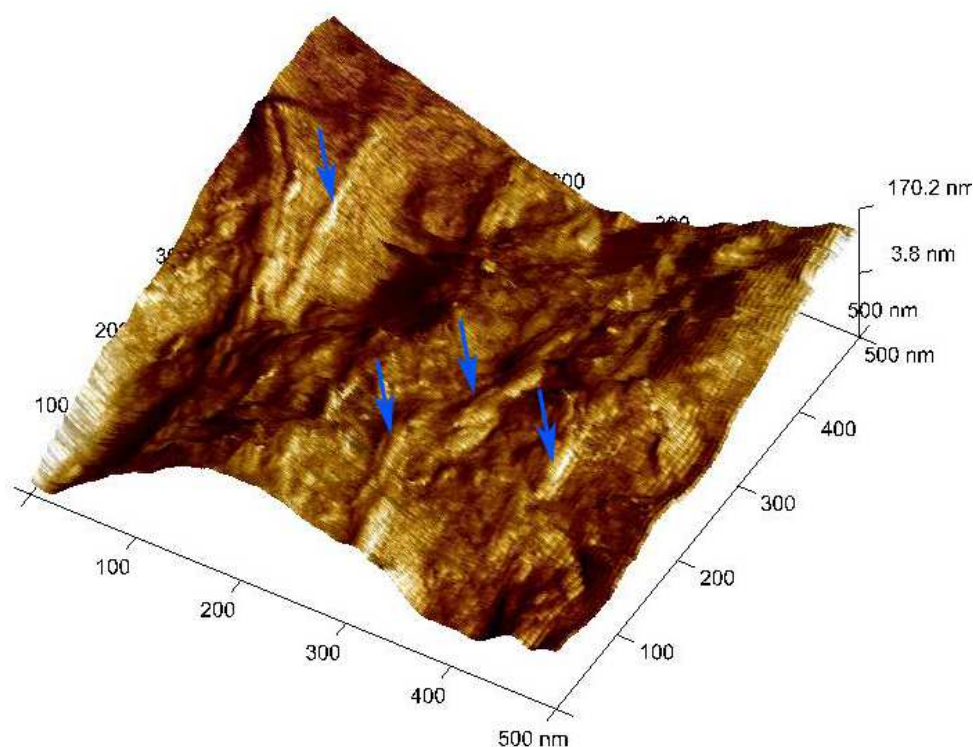


Figure 57: 3D Image of the substrate surface with clearly resolved microfibrils. The picture is colored with amplitude information to enhance contrast.

By looking at the data from the measurement, where we also looked at the sample for 1 hour, we could observe these microfibrils coming out of the surface and vanish again. It seems that the surrounding area with no features is an amorphous cellulose matrix crossed by microfibrillar structures. This again reveals the multiphase nature of our substrate, showing crystalline as well as amorphous areas in the substrate. These different regions seem to be degraded at different velocities, leading to the already mentioned holes and trenches also observed by [3]. In Figure 58 a series of pictures is shown with microfibrils appearing at the surface and vanishing again.

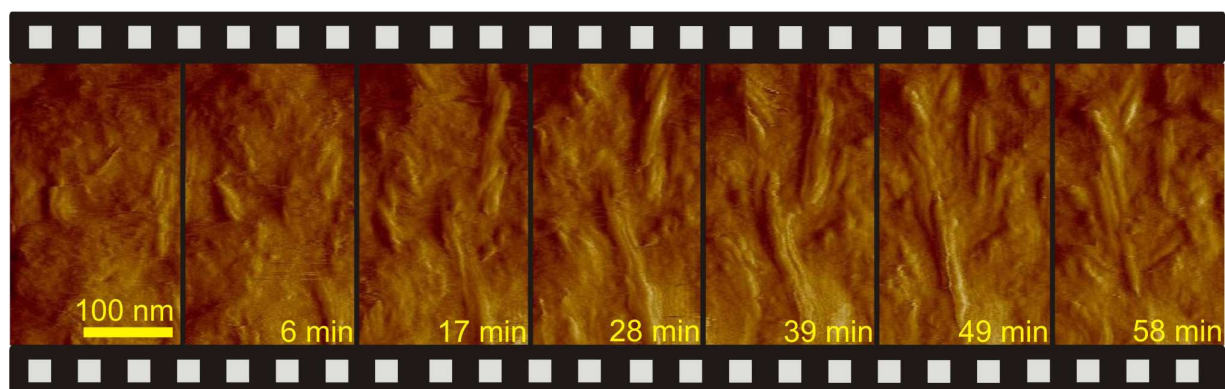


Figure 58: Picture series over about 45 min of degradation. Clearly visible are two microfibrillar structures which first appear and vanish after some time again.

These pictures show impressively how well L-AFM can resolve even smallest features like the microfibrils of cellulose with diameters of about 7-13 nm which is typically found in cellulose (see chapter 2.1.1).

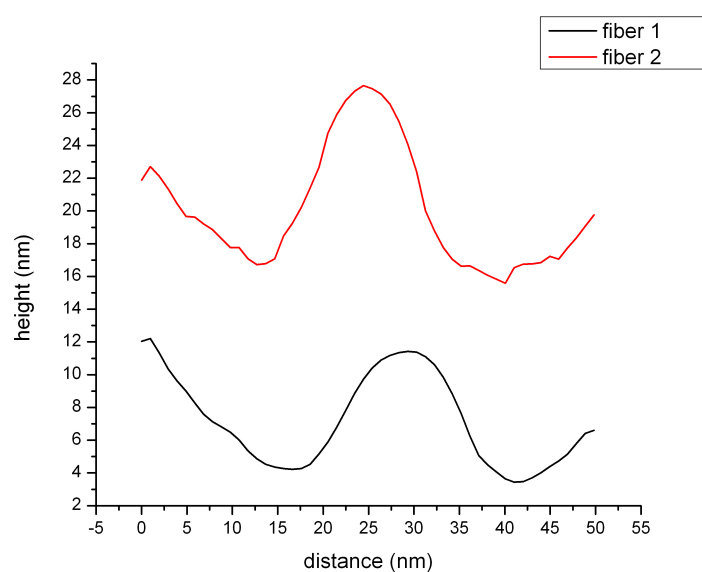


Figure 59: Chapter over two arbitrary chosen microfibrils. Fiber 2 has a height offset for better visualization.

The fibrils have a height of 5 to 15 nm and are often found in bundles, probably forming the so called macrofibrils (see chapter 2.1.1).

By taking closer looks at the degradation, different rates are found during hydrolysis. 10 points (see Figure 60) were investigated on 18 subsequent images, forming a dataset of 180 points. The depth evolution of these points was recorded, showing the velocity of hydrolysis on our substrate. In Figure 60 two points have been used to illustrate these two different velocities. By taking the difference between

each point a degradation speed per image or per minute can be recorded. This was done for 180 points forming a statistical distributed set of degradation velocities. A pronounced statistical analysis gives the evidence for this before suggested two velocity system (see Figure 61).

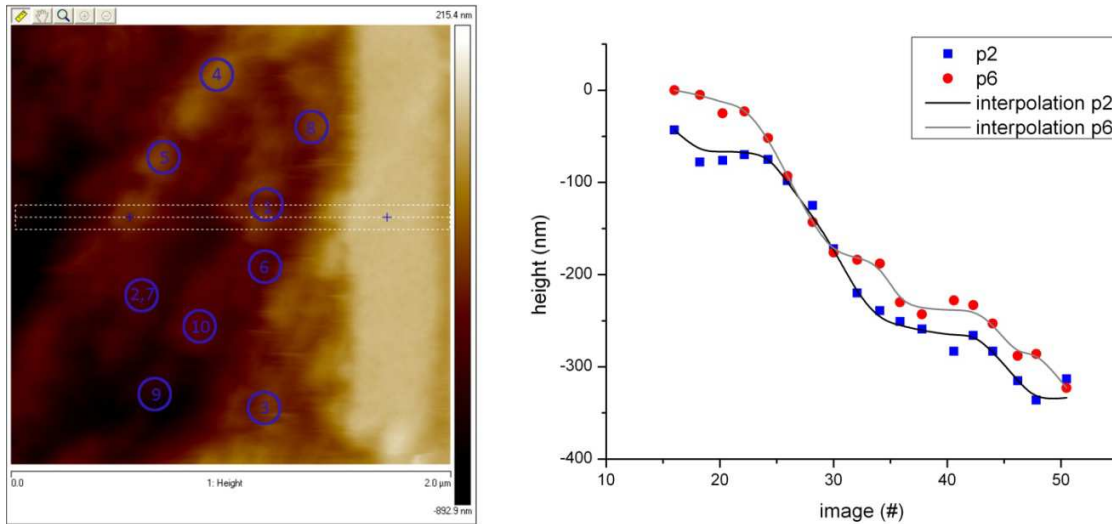


Figure 60: Depth evolution of two points on the substrate.

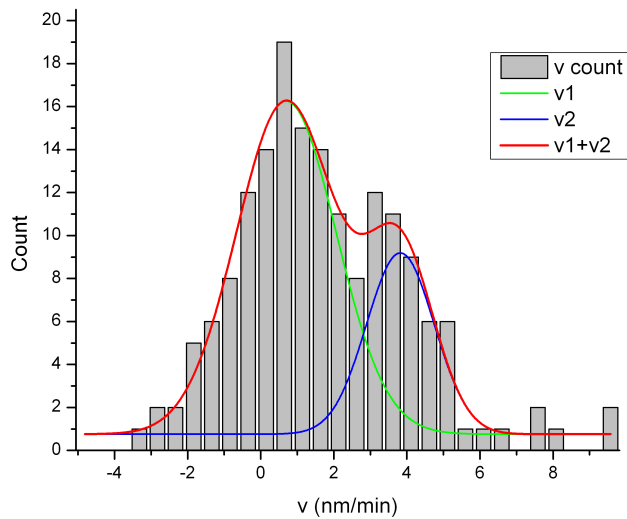


Figure 61: Statistical analysis of degradation rates per minute. Two distinct velocities are visible and fit results give $v_1 = 0.7 \pm 0.1$ nm/min and $v_2 = 3.8 \pm 0.2$ nm/min with a fit quality of $R^2 = 96\%$.

These results show impressively how the cellulose substrate is degraded by a whole system of enzymes. It is known that these enzymes work in a cooperative way (synergism), which means that when split up

in its components the sum of single enzyme degradation rates stay below the cooperative degradation rate. This makes the interpretation, without knowing the single component results very difficult. Hence, in the following chapters all the components of our cellulase system, are investigated separately. These enzymes are part of the cellulase system of the fungus *Trichoderma Reesei* and will be separated into single components for the following investigations.

7.3 Cellobiohydrolase 1 (CBH 1)

The CBH 1 is an exo-glucanase and is able to release cellobiose from a cellulose chain (see chapter 2.1.2.1). For this the end has to be a reducing end to be accessible for CBH 1. If such an end is found by the enzyme, it binds to the chain via a binding domain and moves along the chain with the help of chemical energy coming from hydrolysis. For comparable results the experiment is done in the same way as for the supernatant. First we recorded an image as reference and then we added the enzyme and recorded a set of images. We added again 0.18 mg of enzyme solution per 5 µm substrate.

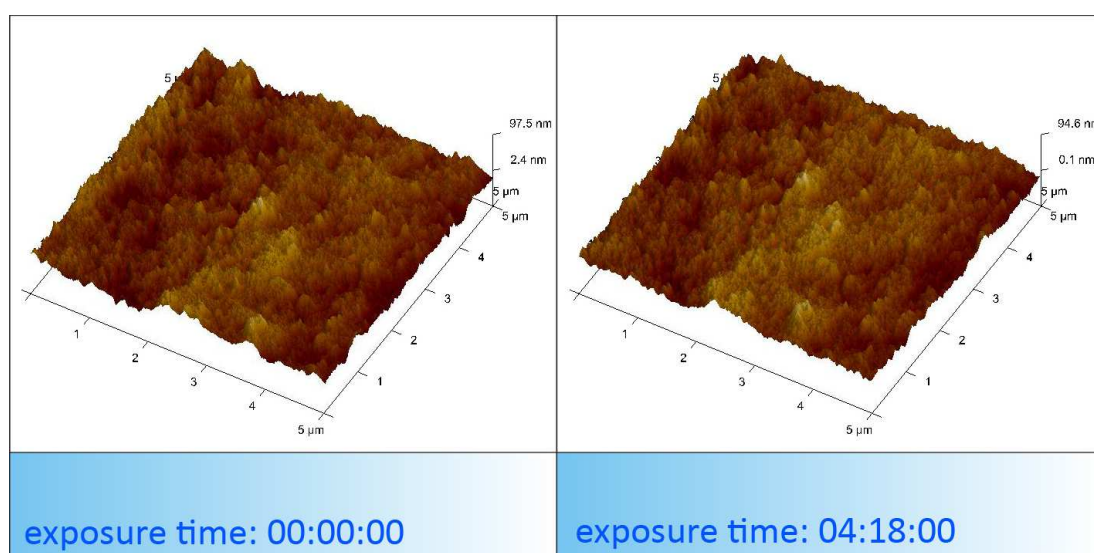


Figure 62: CBH1 activity on cellulose substrate for 4 hours.

There is almost no change in the topography of the substrate, even after 4 hours the substrate looks almost the same. An analysis of phase images revealed that there is activity on the substrate but with very slow progress. We observed that prior fibrillar structures, about 10 nm wide, vanish during hydrolysis as shown in Figure 63 and Figure 64.

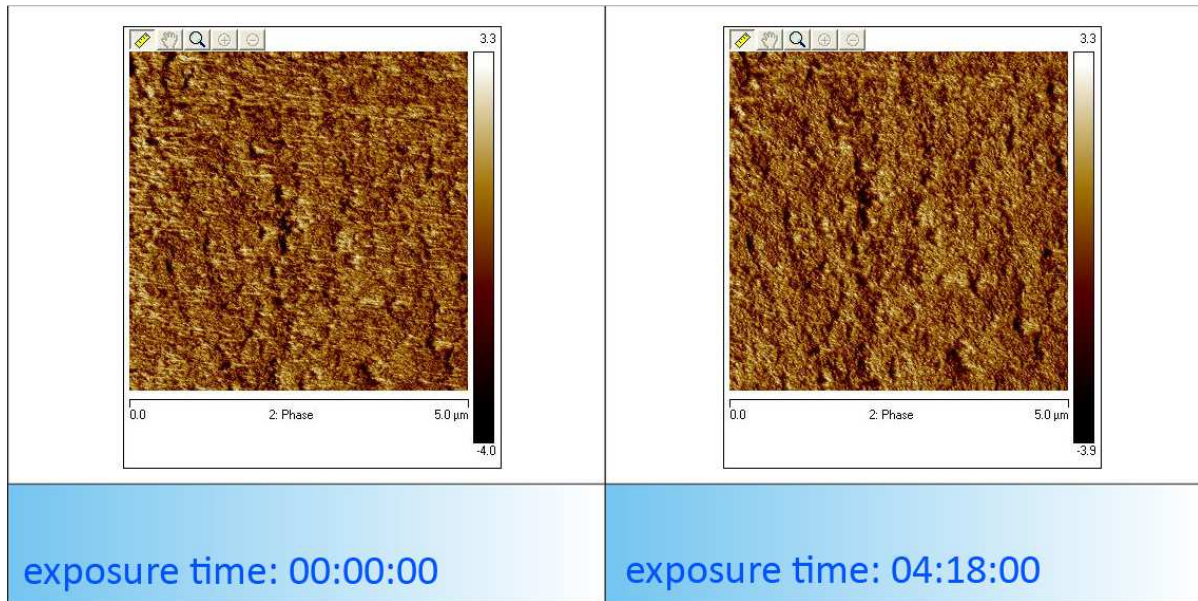


Figure 63: Phase images after 4 hours of exposure.

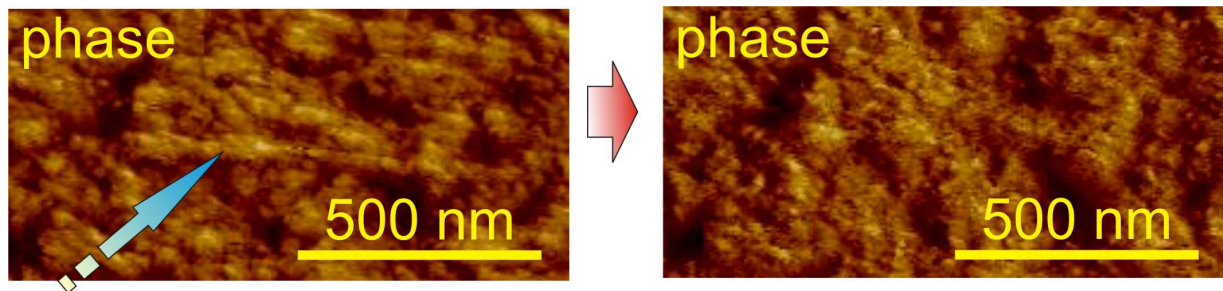


Figure 64: A magnified image from Figure 63 where the fiber is clearly visible indicated by the blue arrow.

In Figure 63 and Figure 64 the phase images show that elongated structures which are present at the beginning vanish over the time of 4 h. So there is a degrading action on the substrate but with magnitudes of order less velocity than by the supernatant. To support these findings, biochemical experiments on multiphase substrate have been performed (see Figure 65).

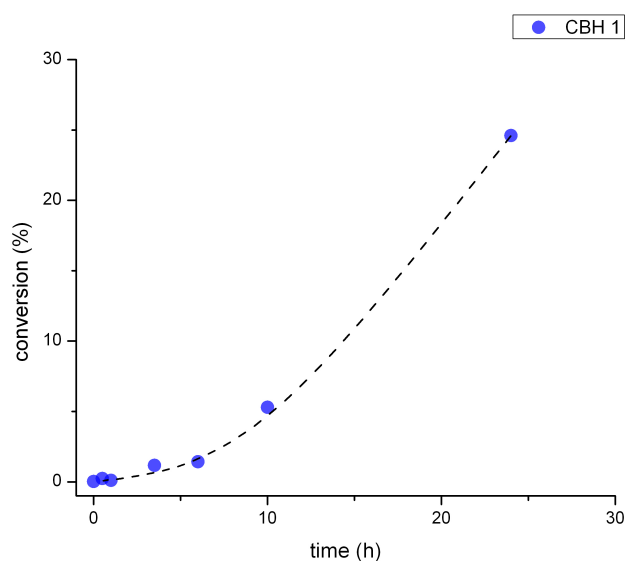


Figure 65: Biochemically determined CBH1 hydrolysis at 50 °C.

What's immediately standing out is that also at 50°, conversion is low especially in the first few hours. So also this correlates well with AFM data. The reason for low conversion at the beginning may be a result of preparation. We propose that due to the cutting procedure, a thin amorphous layer is formed on the top face of the substrate. This layer has only a few microfibers visible on the surface, as shown in Figure 63. With almost all crystalline structures covered with amorphous cellulose, hydrolysis activity of CBH 1 is low due to its nature as an exo-glucanase. The enzymes degrade the few crystalline cellulose particles (see Figure 64) but gets then stuck in the amorphous matrix. This elucidates the low conversion rate. Since the CBH 1 filtration process cannot be termed as perfect little amounts of other enzymes are present in the solution. In this case little amounts of endoglucanases are present in the enzyme solution, thus leading to a slow disintegration of the amorphous layer. It seems obvious that the endoglucanases start to decompose these amorphous layer thus exposing more crystalline areas. This then makes crystalline areas again available for CBH 1 hydrolysis, hence increasing the conversion rate after about 10 h of incubation at 50 °C. Unfortunately, the heating element of the liquid cell was not finished at this time, so an observation of this amorphous layer degradation couldn't be watched via AFM.

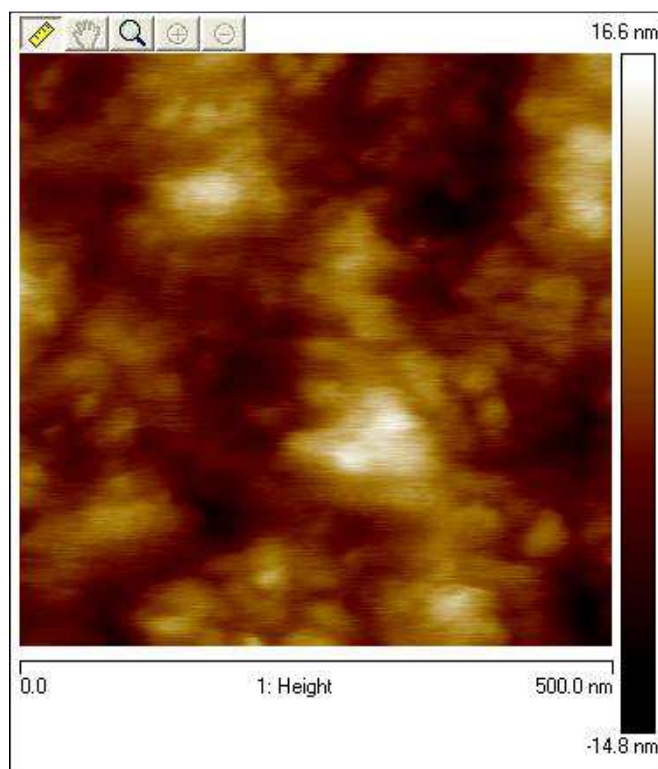


Figure 66: Height image at 500 nm scan range after incubation.

In Figure 66 the height image of a 500 nm scan is shown, with no fibrils visible in the picture. This may be a result of the missing or low degradation process. It may also be a result of the preparation where possibly a thin amorphous layer is created on the surface as described before. The phase and amplitude images are also not revealing any information about microfibrils.

7.4 Cellobiohydrolase 2 (CBH 2)

Cellobiohydrolase 2 (CBH 2) is an exo-glucanase and is working on a cellulose chain coming from the non-reducing end (see chapter 2.1.2.2). The experiment was done in the same manner as with CBH 1 with one exception: We used a different amount of enzymes for the experiment because we could see only low progress in the biochemical hydrolysis experiment. So we decided to use 2 mg of enzymes per 5 mg instead of 0.18 mg.

7.4.1 Overview Imaging

In this experiment we decided to use an image size of 5 μm to get an overview of the degradation process on the μm scale. Again a crystalline residue was found on the sample and taken as surface

reference since this particle is degraded way slower than the surrounding amorphous/crystalline sample. Figure 67 shows the reference picture of the sample with 10 μm image size.

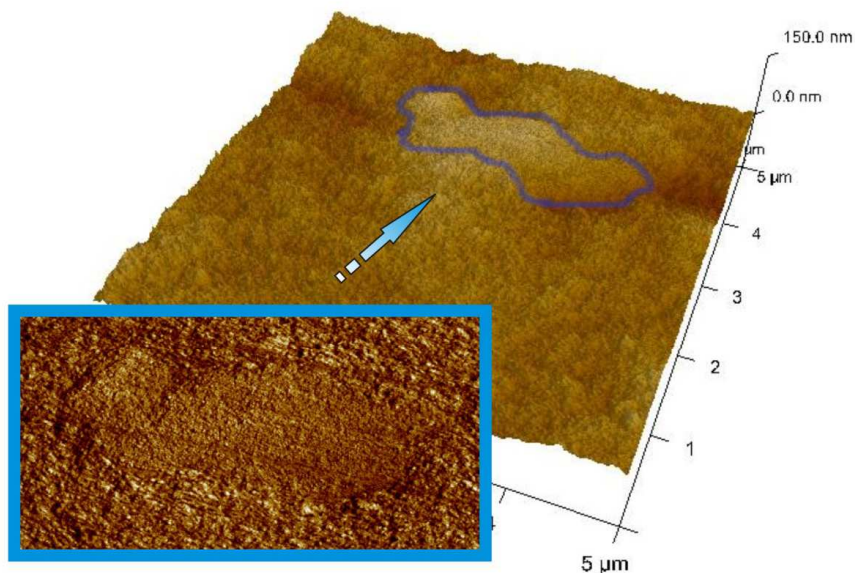


Figure 67: The measurement site with the crystalline residue (blue).

In Figure 68 the degradation process is again clearly visible during an exposure time of about 5 h. Since we didn't expect any noticeable progress with our normal enzyme concentration of about 0.18 mg enzyme per 5 mg substrate we decided to use 2 mg instead. This is definitely one reason why we see such remarkable process during this period. What we also observed is that the degradation profile of the surface looks a bit different in comparison to the supernatant. If we take into account that we used a 5 μm scan for the supernatant and a 5 μm scan for the CBH 2 enzyme it is immediately noticeable that the holes and trenches are much narrower for the CBH 2 enzymes (see Figure 53 and Figure 68). This can also be seen if Figure 54 and Figure 69 are compared.

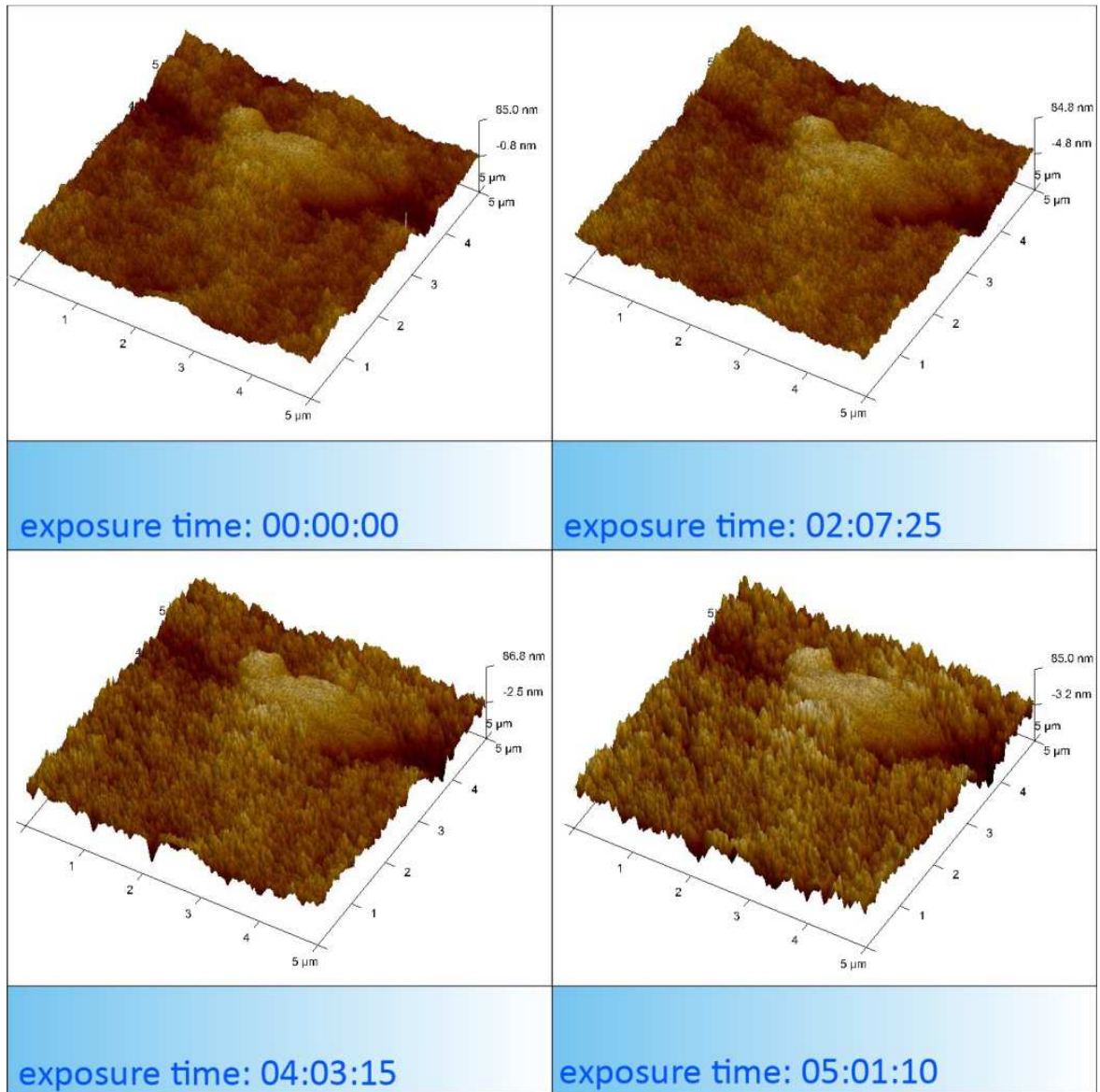


Figure 68: The results of the degradation process over a time of 5 hours with the enzyme CBH 2 of *Trichoderma Reesei*.

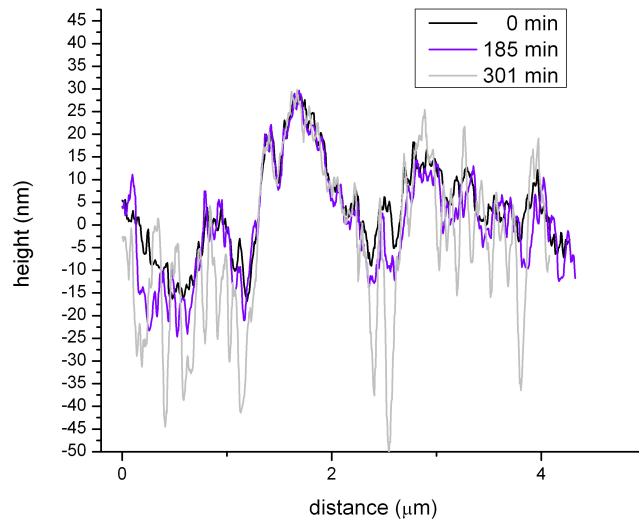


Figure 69: Chapter profiles from different times during degradation. In the middle a crystalline residue is present and not degraded.

Again an error of 10% was estimated for the RMS plot since the images showed an x-y drift and deep holes may be a problem for an accurate measuring of the deepness of a trench or hole.

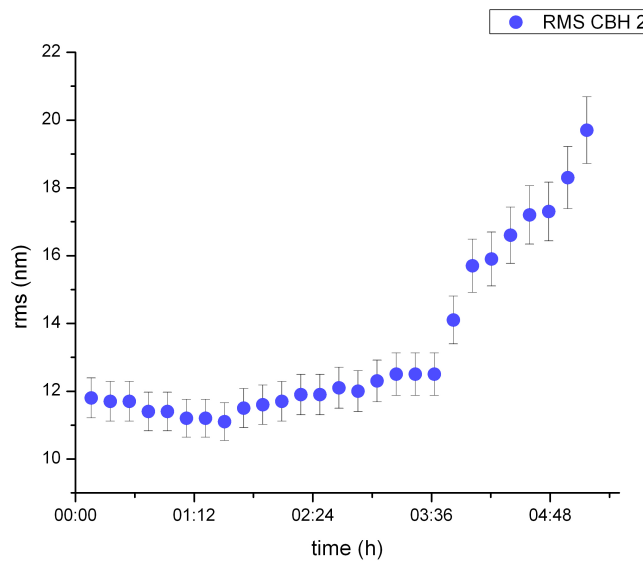


Figure 70: RMS evolution for CBH 2 exposure for more than 5 h.

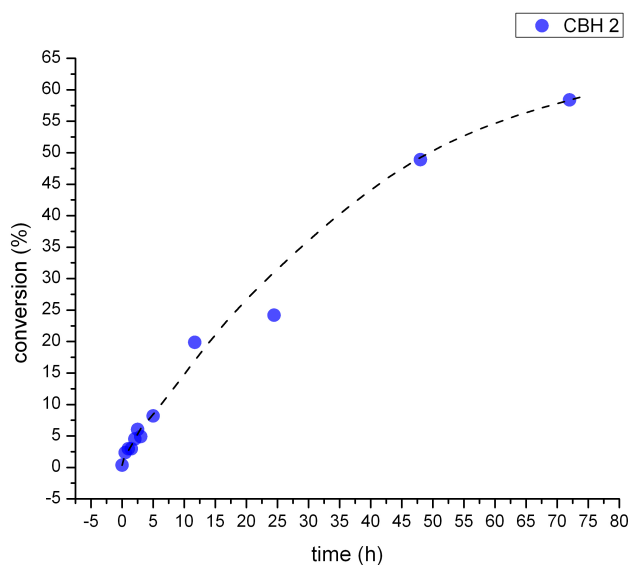


Figure 71: CBH2 hydrolysis at 50 °C.

In Figure 70 the degradation starts again after a delay time of about 1 hour which is not clearly pronounced in the RMS plot but visible by watching at the pictures or a video of the process. Here, progress is visible after one hour and the degradation starts at this point, gaining speed over the first few hours of the experiment. This may show how inadequate a RMS plot may be in referencing a conversion start. The delay time is again attributed to a diffusion time of the enzymes in the substrate. After this obligatory hour the substrate is degraded by the formation of deep and narrow trenches. The increase of the degradation speed may come again from an amorphous thin layer on top of the surface, coming from the cutting procedure. The narrow trenches and holes compared to the supernatant experiment are most likely the result of a substrate affinity of the CBH 2 molecule. This affinity allows the enzyme to attack only one phase efficiently, thus forming this trenches and holes where as peaks are coming from the less efficient degraded phase. This does also lead to a degradation where the top level of the substrate is preserved in these peaks and absolute surface lowering in respect to the crystalline particle is visible. Now to get an idea which phase is degraded more efficient by a nano-scale experiment has to be performed.

7.4.2 High Resolution Imaging

Again a crystalline residue was found which is shown in Figure 72 as the reference image. Here we want to investigate how the CBH 2 enzyme attacks the surface and if the enzyme prefers one type of substrate (amorphous or crystalline).

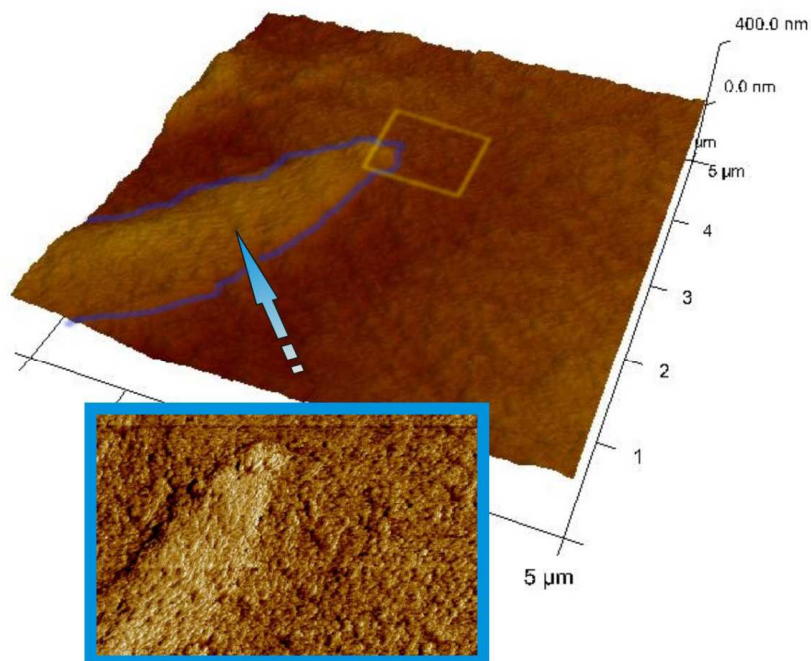


Figure 72: Crystalline residue (blue) and reference picture for the high resolution imaging. Yellow rectangle is the measurement spot with 1 μ m size.

Starting the measurement on 1 μ m scale, as indicated by the yellow rectangle in Figure 72, revealed an interesting and unseen behavior of the enzyme CBH 2. While it is believed to work as an exo-glucanase from the non-reducing end we observed that the enzyme shows affinity to amorphous areas. This was visible only after the complete measurement, where again a 5 μ m image was recorded and a cleaning effect became visible. The enzymes seemed to primarily attack amorphous and less crystalline regions resulting in deep trenches. These degradation spot became also visible in the phase images where at spots with high activity, dark cloud like structures appeared. These structures changed shapes during measurement, indicating a highly dynamic process. Since CBH 2 is the only component added to the buffer solution we attribute these clouds to agglomerations of CBH 2 particles. These clouds of enzymes attacked the surface, resulting in the deep trenches as shown in Figure 74. A close look on the angles in these trenches eliminated the possibility of tip artifacts with angles around 15°. So these clouds can be seen as a cluster of enzymes working together on the substrate. After the measurements, highly crystalline areas are visible, completely cleaned from any obvious amorphous material (see Figure 73). We also found, that the enzyme clouds seem to vanish again from the surface when their work is done.

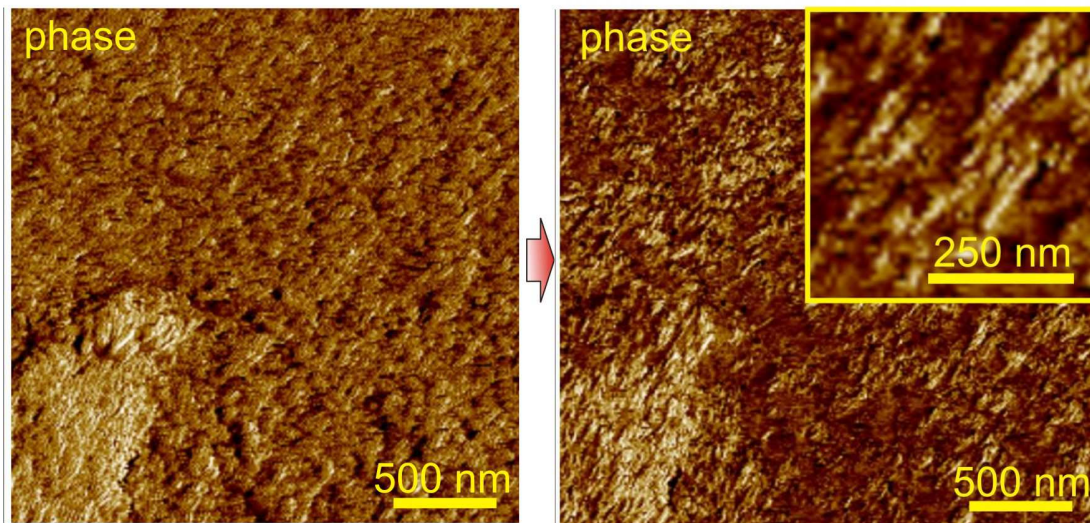


Figure 73: Cleaning effect of the enzyme CBH 2 on our multiphase substrate. In the left lower corner a crystalline residue is present.

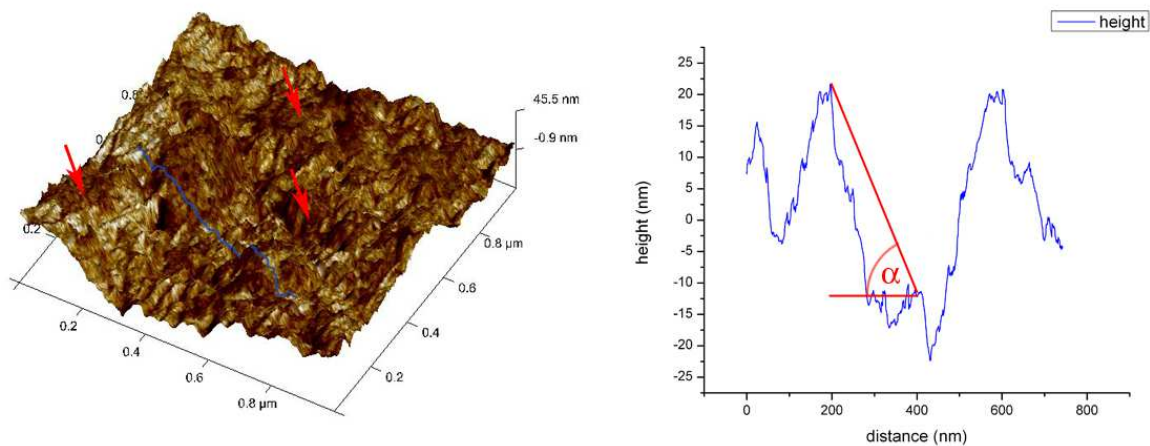


Figure 74: 3D image of the measured surface the crystalline residue is visible in the left lower corner (little bit brighter). The red arrows mark darker clouds on the surface and blue is the section (left). You can see also the section profile with the angle α which is in this case 10° . (The angle looks bigger because of units!).

We did measurements as illustrated in Figure 74 to see if the darker phase “clouds” are a measurement artifact, but we only found angles of about 10 to 20 degrees which are too broad to get near the tips surface which has an opening angle of 30° . If the darker phase areas would result from tip artifacts the angle must be at least 60° to get problems with our explanation. A schematic representation of the tip artifacts is shown in Figure 75.

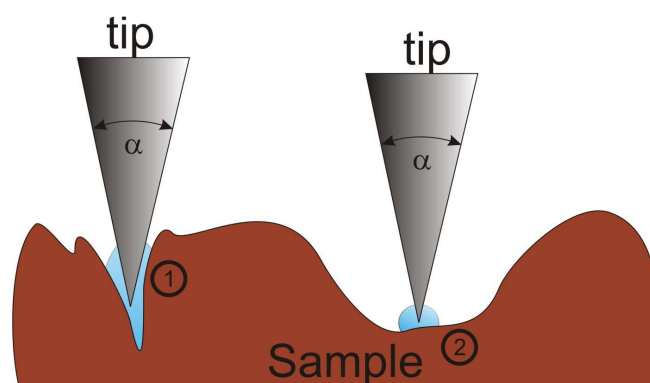


Figure 75: (1) narrow hole and broad hole (2). The force field is blue. In case of (1) predictions about enzymes being at work at the surface would be difficult. In case (2) no problems due to increased force fields occur.

Furthermore, these clouds seem to move and reshape during the experiment which is a strong indication that we are observing mobile particles on the surface which is a very strong indication that we are seeing enzyme clouds on the sample surface. Figure 76 shows a cloud reshaping during measurement.

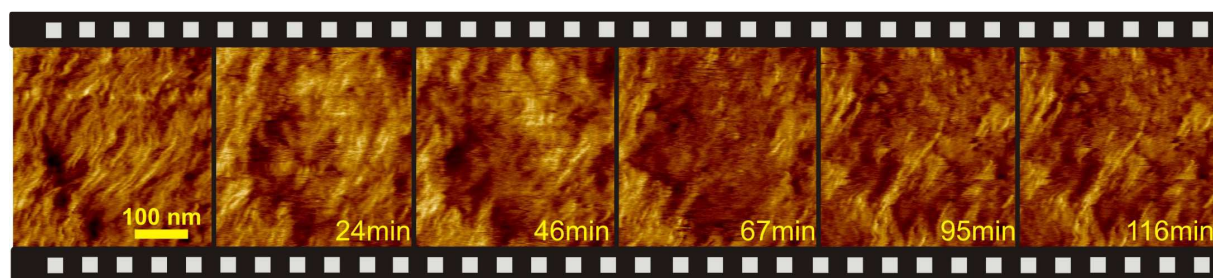


Figure 76: Phase images taken from the crystalline residue. The images go from left to right. These images show a dark cloud reshaping and moving during the measurement which is possibly an enzyme cluster.

This nano-investigation showed that the CBH 2 enzymes show strong affinity on amorphous cellulose. As shown in Figure 73 the enzymes attacked the amorphous areas, leading to deep and narrow holes with the peaks as crystalline fibers. These fibers are highly parallel and these are not attacked that much. However, we suggest that also these fibers suffer degradation with a lower velocity and less enzymes bound by these surfaces. Now we know that our holes in Figure 68 and Figure 69 are amorphous regions of the sample. With these conclusions the last enzyme to be investigated is the endoglucanase 1 or EG 1.

7.5 Endoglucanase 1 (EG 1)

Biochemical experiments showed low degradation for an enzyme content of 0.18 mg per 5 mg substrate as can be seen in Figure 78. This is completely understandable, when recalling the nature of this enzyme (see chapter 2.1.2.3) where it has the task to randomly cleave chains of cellulose, producing free ends for the exo-glucanases. This implies that no or just a low content of cellobiose and oligosaccharides are

released, when the endoglucanase coincidentally cleaves a few units before an existing chain end. This is at the beginning highly unlikely with rising likelihood with ongoing time, coming from increased number of new chain ends. Since we didn't expect strong effects, we decided to do a compromise with an image size of 2.5 μm , which is between high resolution imaging and overview imaging. Again a reference image was recorded and is shown below.

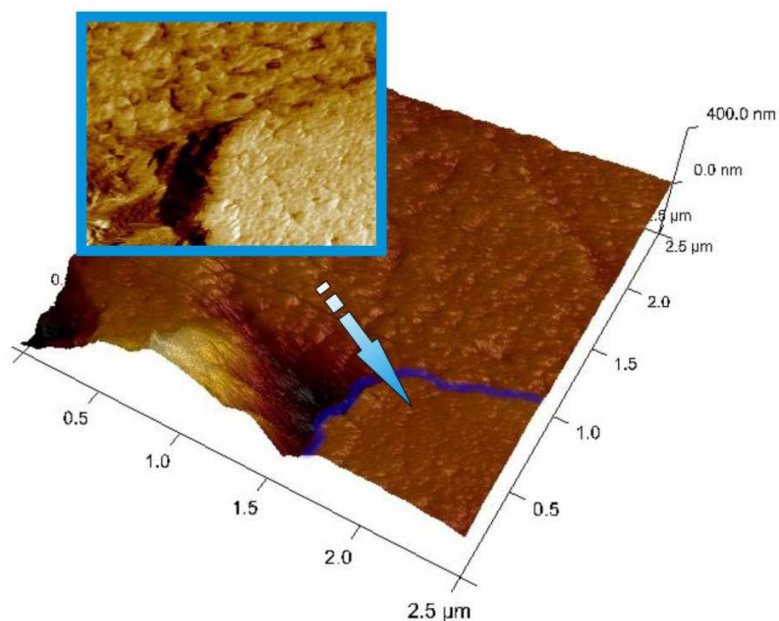


Figure 77: Reference image of the surface before EG 1 incubation.

Figure 77 shows a crystalline residue in the left lower corner with some unidentified structures in the right lower corner. We believe that here also a crystalline residue is present but with a different orientation in the substrate. Even if this is not perfect for an investigation we used this side for our experiment. Below the degradation is shown in 3D over a time of approximately 6 $\frac{1}{2}$ hours.

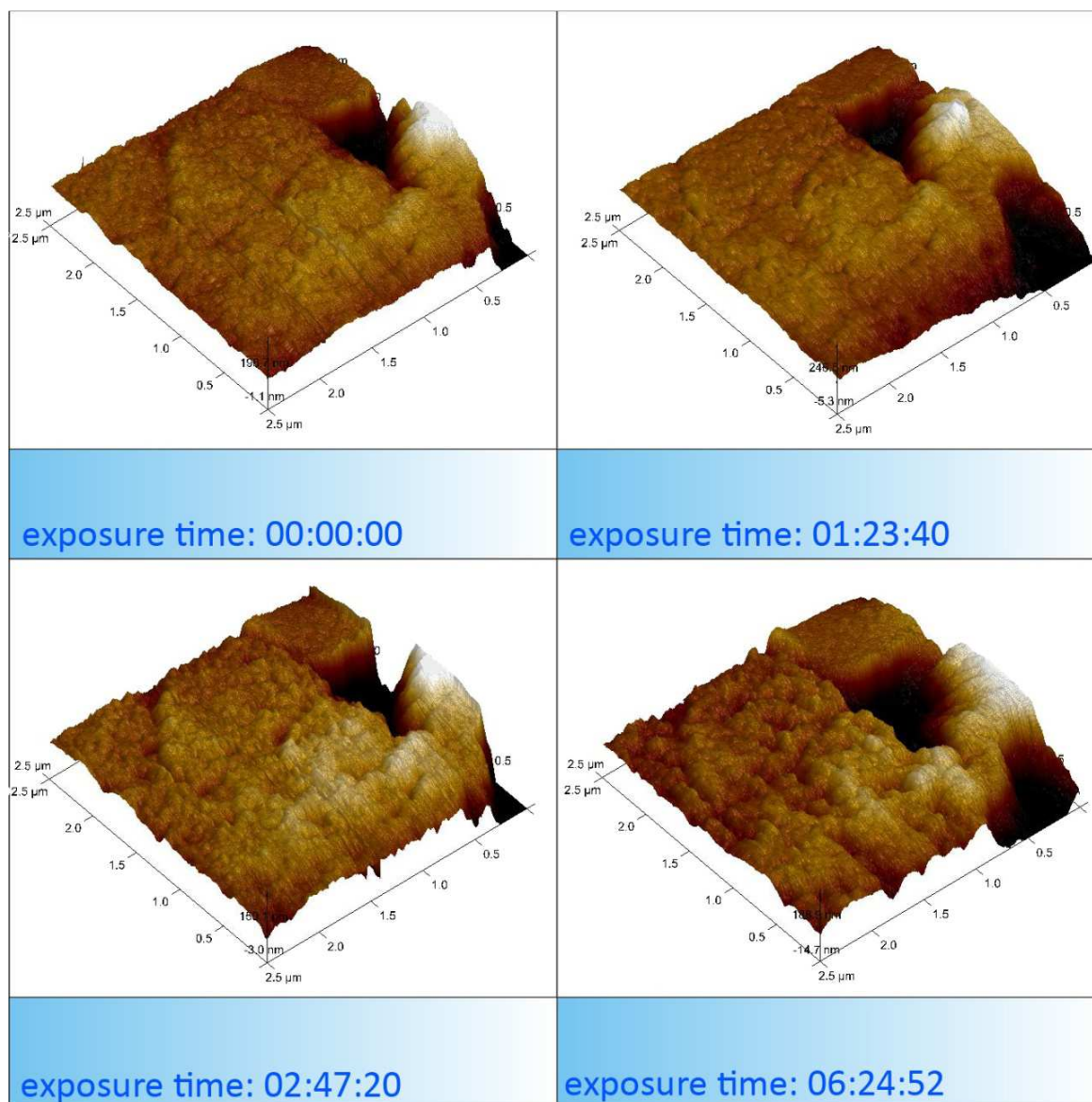


Figure 78: The results of the degradation process over a time of 6 1/2 hours with the enzyme EG 1 of *Trichoderma Reesei*.

It is visible that the surface suffers changes in the topography, where mostly little holes open up over a time of about 6 hours. This rather low degradation result is not surprising as described before. It is not the nature of the enzyme EG 1 to release cellobiose and other oligosaccharides. The enzyme cleaves randomly accessible chains, where cellobiose or other oligosaccharides are only released when this happens close to a chain end. Oligosaccharides up to a chain-length of about 6 sugar molecules are water soluble, thus dissolving in the buffer solution. Biochemical experiments showed a high content of glucose in the solution, coming from cleavage activity at the end of a chain as well as from oligosaccharides dissolved in the buffer. These oligosaccharides are attacked by EG 1 in solution, producing cellobiose and glucose. Furthermore, a widening of preexistent holes was observed. We

believe that at these holes the availability of free chains is higher thus leading to higher activity and degradation. In summary, we could show that EG 1 can slowly degrade our multiphase substrate.

We also looked at the RMS evolution of a rather small area of about $1.5 \times 1.5 \mu\text{m}$. Normally we looked at least over an area of 5×5 or $10 \times 10 \mu\text{m}^2$ but since we measured on a rather small scale we had no other possibility. So keep in mind that these results may not hold for the whole sample or better are statistically not as good as the RMS plots before. In Figure 79 the RMS evolution is shown, where we estimated the error with 20%, since the area is small and we also had an x-y drift during the measurement (see Figure 79).

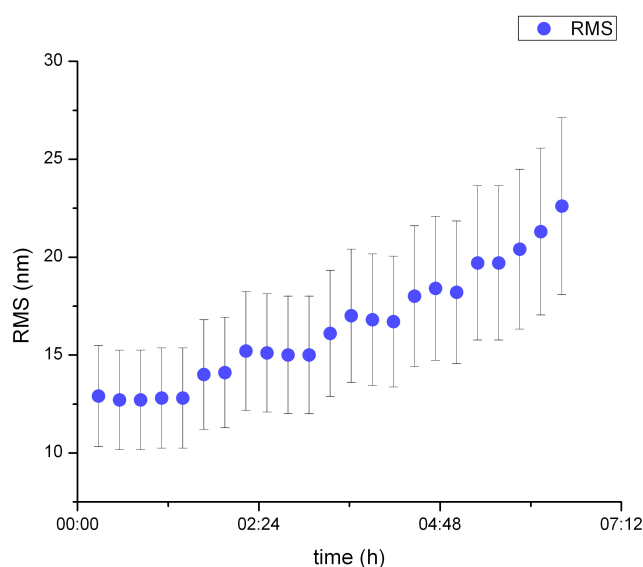


Figure 79: RMS evolution over incubation time. The error is estimated with 20%, coming from a small image area and x-y drift.

If these data is compared with biochemical analysis of hydrolysis the results match perfectly together. By taking a closer look on Figure 80 and Figure 81, one can see that there is about 1/2 hour low conversion until the degradation starts to rise and gain speed. This behavior is most likely coming from the fact that at the beginning only a few free chain ends are present, where water soluble oligosaccharides can be cleaved. Producing more and more chain ends with time the conversion gains speed, while saturation appears at 70 % after about 80 h. This and the diffusion delay may play also a role in our AFM experiment shown by the RMS plot in Figure 79.

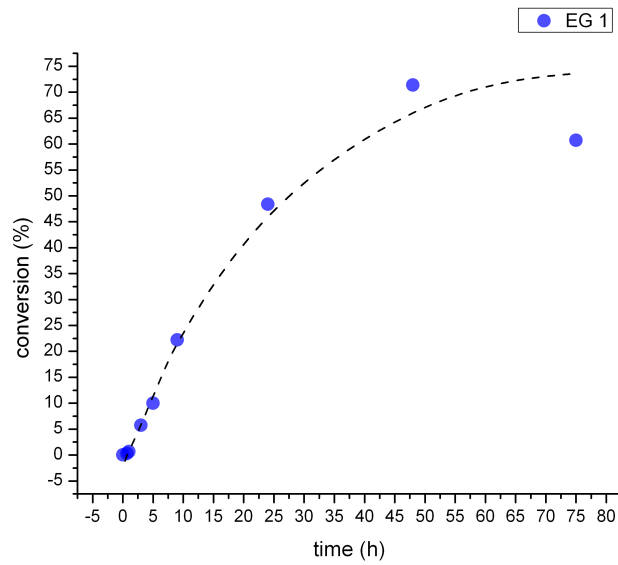


Figure 80: EG 1 hydrolysis at 50 °C.

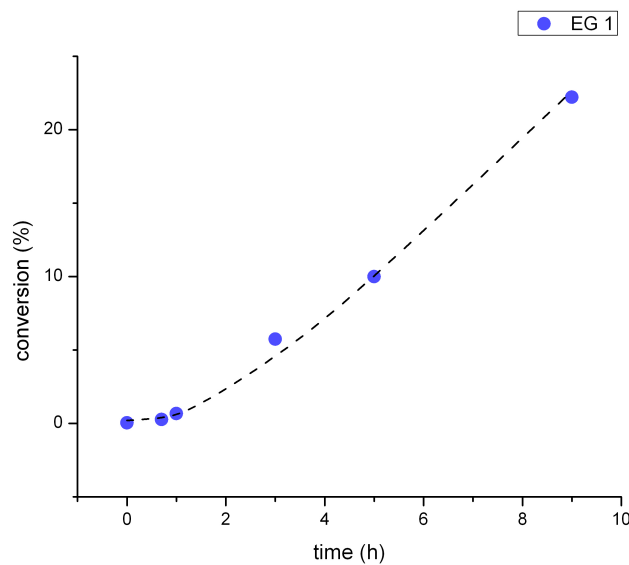


Figure 81: Looking at a smaller timescale from Figure 80. For the first hour conversion is low.

The biochemical experiments was done at 50° Celsius, which would mean a dead time in our experiment of about 3-4 hours which is in good comparison with our RMS measurement. Once again the RMS measurement shouldn't be taken as direct comparison to the biochemical experiment because the RMS is only a result of the hydrolysis and must not increase when the surface for example is degraded

homogeneously. Nevertheless, in this case the surface seems to be degraded again differently on different positions, which makes the RMS in this case a good alternative to the biochemical analysis.

7.6 Summary of Single Component Experiments

Now that all components are analyzed separately, a review on the supernatant experiments reveals magnificently how striking synergism is in cellulose hydrolysis. While we observed a local hydrolysis degradation of 300 nm in about 4 hours with the supernatant, we couldn't get even close to this rate with single enzyme components, although the concentration is raised massively (CBH 2). Therefore, interpreting the supernatant result has to be done carefully. Furthermore, we observed quite astonishing and interesting results for CBH 2. These enzymes were believed to work as exo-glucanase, with primary activity on crystalline chains. Our investigation revealed that primary activity was observed on amorphous areas. The degradation was way faster for amorphous cellulose than for crystalline areas. This may be quite surprising because X-ray investigations [1] revealed that the enzyme looks very similar to CBH 1 with an active site tunnel. So a tunnel is not quite appropriate for an endo-type activity of this enzyme, more seeming as impossible. But as recently suggested by Igarashi (2011) [27] an opening of the two surface loops building this tunnel could be possible. This would explain the observed behavior and furthermore the enzyme may be some kind of all-round talent, capable of cleaving chains in between as well as working processive on a chain, coming from the non-reducing end. As for the CBH 1 and EG 1 enzymes we found the same results as suggested by literature ([28] [29] [30]). Additionally we wanted to understand the synergism between the enzymes better, so we constructed a new experiment following in the next chapter.

7.7 Synergism

Now we know that the synergism in our cellulase mixture is quite striking for hydrolysis. To get a better view on the different interaction of the enzymes, we constructed a new experiment where we decided to use a stepwise incubation of different enzymes. We decided to start with EG 1 and continue by the addition of CBH 2 followed by the addition of CBH 1. Between each step we waited for any type of action. In this way we could observe the synergism of EG 1 and CBH 2 as well as the complete synergism. For this we again searched for a crystalline particle on our cellulose substrate which is shown in Figure 82.

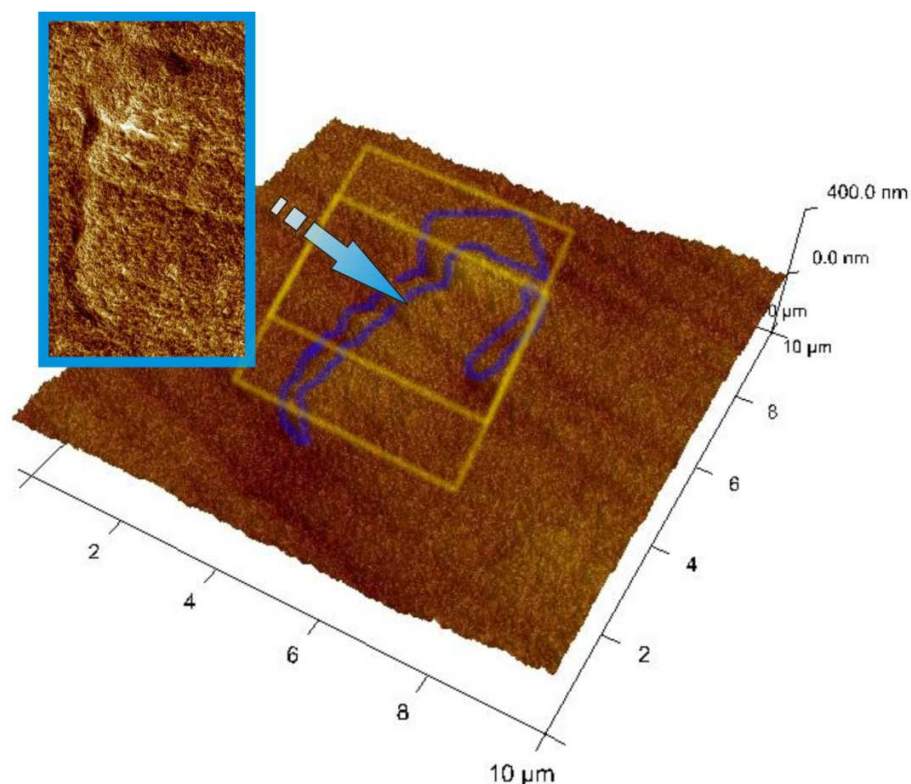


Figure 82: Reference image of the substrate for the synergy experiment. Blue is the crystalline residue with mostly parallel fibers indicating that the residue is lying parallel to the surface. Yellow rectangles indicate the measurement areas where the area below is for the EG 1 measurement and above for EG 1 + CBH2 and + CBH 1.

We started with EG 1 and the next enzyme solution was added after a progress on the surface was clearly visible. We used the following concentrations for the experiment: EG 1 0.09mg, CBH 2 0.5 mg and CBH 1 0.09 mg per 5 mg substrate. We choose this concentration based on our experience with the single component enzymes. This is the reason why we over concentrated CBH 2 in this experiment, to see the effect we observed in the single component experiment. We expected to see again the cloudlike structures in the experiment. To get maximum resolution we choose images of 1024x1024 pixels which will enhance analysis but hinder fast dynamic image recording, thus limiting the capability to form a good video.

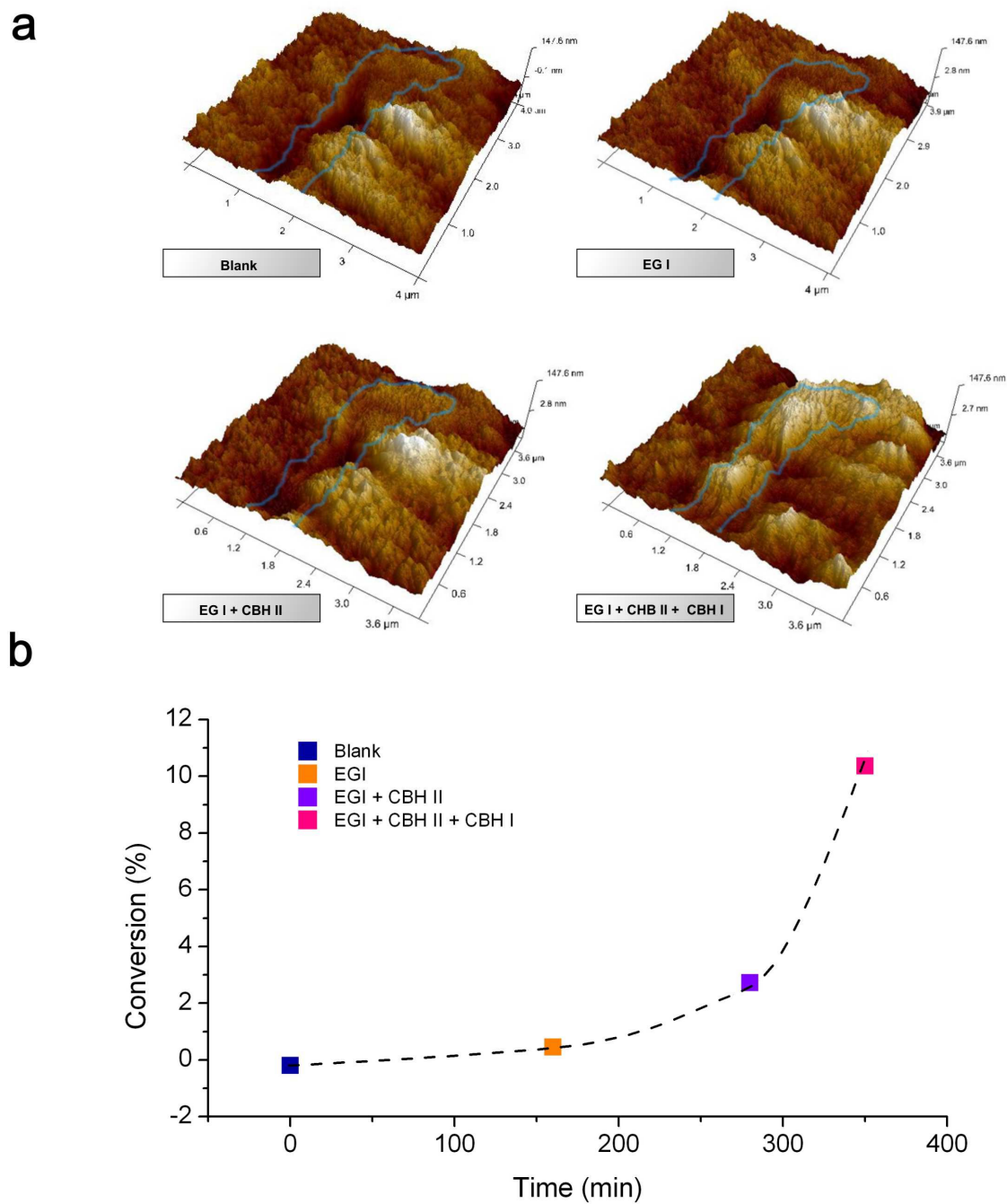


Figure 83: Surface topographies during our synergism experiment. Since it is difficult to see any changes during the EG 1 period a magnified image is shown in Figure 84.

In Figure 83 the process of degradation is shown for each incubation step and the corresponding biochemical data. After this experiment it is evident that synergism plays a major role during cellulose

hydrolysis. To understand the RMS plot, the diffusion has to be taken into account. Here we again are delayed by diffusion which is about ½ to 1 hour. After this the enzymes are uniquely immersed in the liquid. So at first the EG 1 addition brings a slight increase of the RMS because amorphous areas are removed. In Figure 84 this behavior is evident where the removal of amorphous layer material is observed. After the time of 1 hour the CBH 2 enzyme is added to the solution with almost no change in topography for the first hour. Then the degradation speed rises and stays in terms of RMS evolution at a linear rate. After a time of 1 ½ hours CBH 1 is added and again one hour passes before the reaction starts to increase in speed. This shows how perfect the cooperative action is between all 3 enzymes. We see also a synergism between CBH 2 and EG 1 but with less strong behavior. This is even the case when CBH 2 is over concentrated. We suggest that the addition of CBH 1 helps to degrade crystalline cellulose laying free amorphous cellulose which can then be again degraded efficiently by CBH 2 and EG 1. Additionally, EG 1 and CBH 2 help CBH 1 by producing more chain ends also on crystalline cellulose.

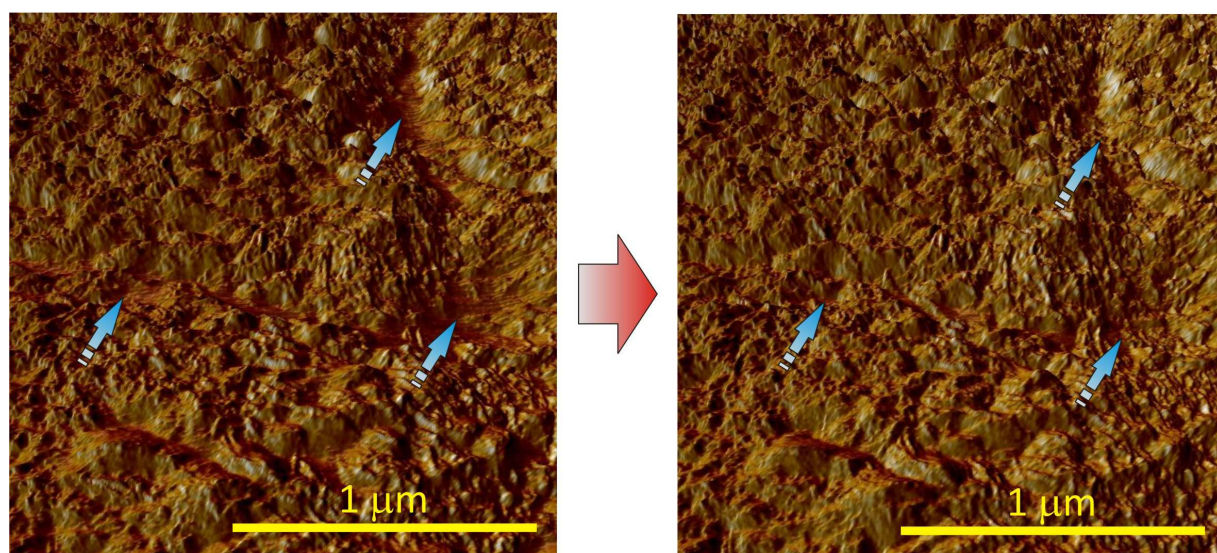


Figure 84: Magnified view of the first hour EG 1 incubation. Blue arrows indicate interesting regions. There we believe amorphous materials (darker smoother areas) are present which are missing after 1 hour of incubation. This shows the affinity of this enzyme for amorphous cellulose.

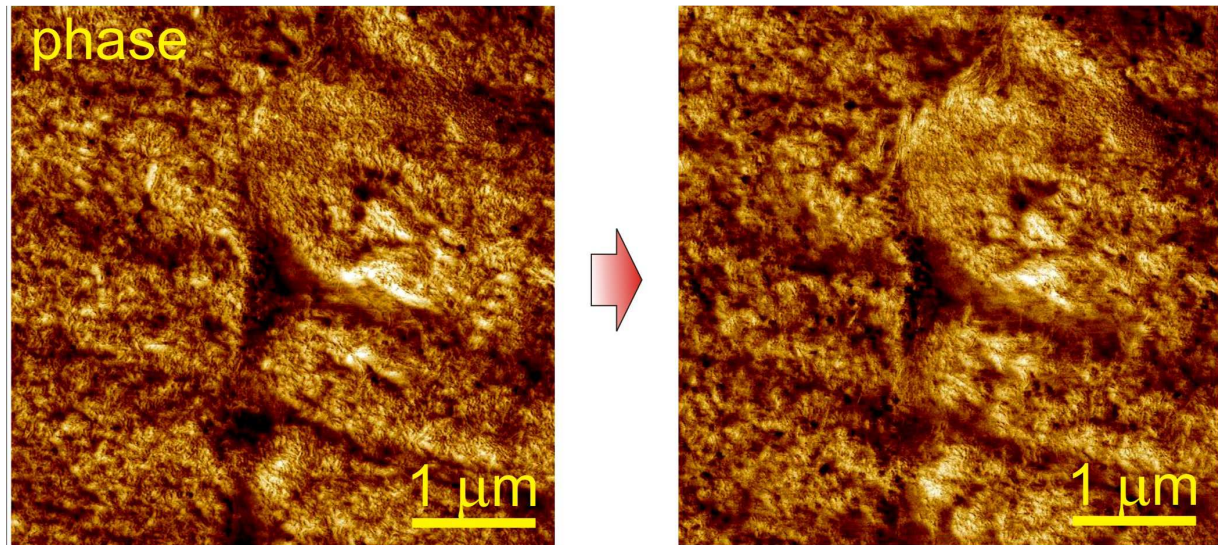


Figure 85: EG 1 + CBH 2 on the substrate. Images are in Phase mode and bright areas are crystalline cellulose fibers. It shows clearly the increase of large crystalline areas whereas small one vanishes.

EG 1 and CBH 2 are working together by removing mostly amorphous regions with small crystalline fibers in it. This suggests that CBH 2 is indeed an exo-glucanase but also an endo-glucanase, as we have seen in the single experiment. This results in an increase of large more dense crystalline areas whereas small crystallites are removed together with their amorphous matrix. This is shown by phase imaging in Figure 85.

8 Summary

In this thesis we showed that the complex process of enzymatic cellulose degradation can be observed in situ via liquid-cell AFM. Although it was not possible to observe the movements of single enzymes due to speed limitations, we succeeded in showing a new concept by designing a temperature controller for temperature controlled investigations. By going to lower temperatures the enzymes will get slower, thus allowing us to investigate them with our conventional AFM. The system has not been tested yet, but will follow this thesis. Nevertheless we could clearly observe how the cellulose surface is degraded by the enzymes of *Trichoderma Reesei*, this is shown in Figure 86.

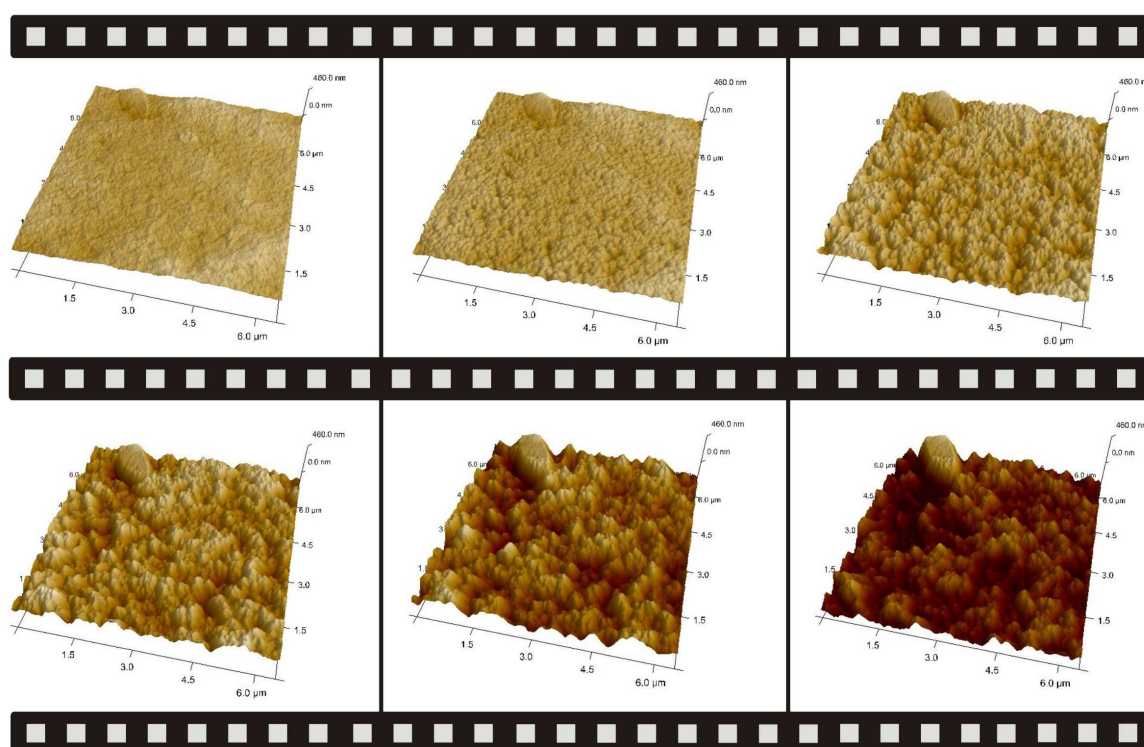


Figure 86: Movie sequence of cellulose degradation by *Trichoderma Reesei* supernatant over 4 h. In the left upper corner a crystalline Avicel residue is present.

While Figure 86 shows impressively how the cellulose surface suffers degradation, a precise understanding on the molecular level is not possible by overview imaging. Hence, we expanded the experiment to the nano-level, showing the precise structure of the cellulose substrate as can be seen in Figure 87. Here we show that the substrate is built of an amorphous matrix with crystalline cellulose fibers embedded. The cellulose fibers are about 7-13 nm wide (see chapter 7.2). These microfibrils are degraded as well as the surrounding matrix as can be seen in Figure 87.

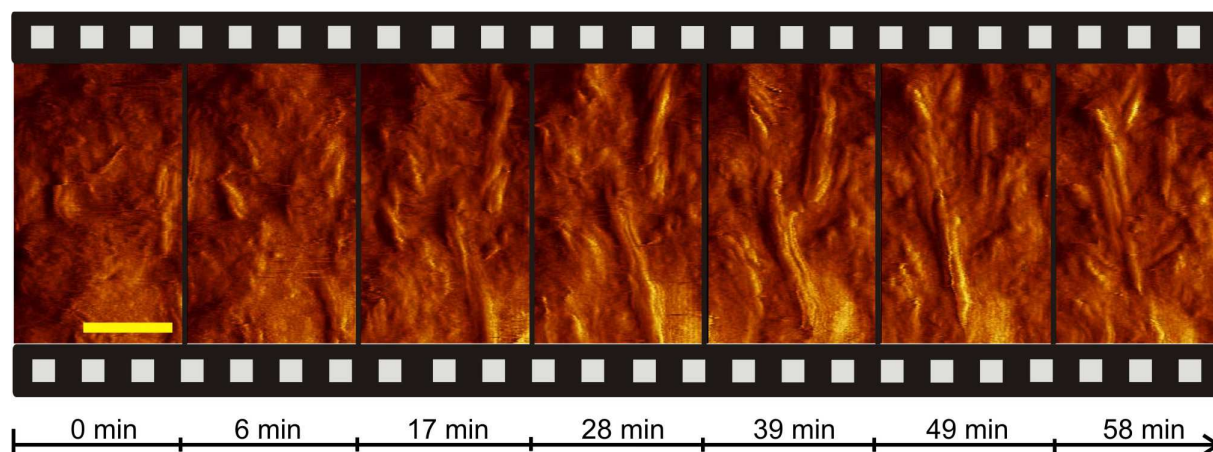


Figure 87: Hydrolysis on the nano-scale by the enzyme system of *Trichoderma Reesei*. Fibers are clearly visible and scale bar is 100nm. The fibers appear and vanish again after degradation.

However, while these results are quite impressive the precise mechanism behind this degradation cannot be deduced. This is because we are dealing with a system of enzymes, not knowing which one is responsible for distinctive effects. Systems of enzymes often show a so called synergism, being the cooperative activity of different enzymes. Hence, it is rather difficult to obtain a clear view from these experiments. By taking the single enzymes and repeating the same experiment a more precise understanding should be possible.

Thus, our next experiments aimed on the single component degradation of our cellulose substrate. The enzyme solution used as the supernatant includes CBH 1, CBH 2 and EG 1. We started by observing the behavior of CBH 1.

CBH 1 did not show any major effect on the substrate even on long timescales of about 4 h. Consideration of biochemical data (see Figure 65) showed that the system is nearly inactive in the first 10 h even at 50 °C. We propose that during cutting a thin amorphous layer is produced due to the stress. For efficient degradation of this layer an endo-type enzyme is needed which is not present. Furthermore the AFM data revealed that small fibers which sustained cutting stress are degraded quite well (see Figure 88 a). Therefore, the low activity of CBH 1 can be explained by this.

CBH 2 showed little activity in prior biochemical experiments, thus we increased the cellulase concentration by the factor 10 (0.18 mg to 2 mg/5 mg Substrate). The investigations with this cellulase content showed quite surprising effects during hydrolysis. First we observed that degradation is again quite strong over 4 h and that the surfaces seemed to be cleaned after this time in a way that crystalline areas were mostly not attacked while amorphous areas vanished completely (see Figure 88 b). This behavior is more typical for endo-glucanases as EG 1. Hence the understanding of CBH 2 as a exo-glucanase with affinity on crystalline cellulose has to be reconsidered. Furthermore, we observed a clouding effect (Figure 88 d) in a way that cloudlike structures appeared during hydrolysis. These clouds

were highly dynamic, changing shape and size over a timescale of 116 min. After this time the area below was of crystalline nature with closed packed fibers. We propose, that this is the mentioned cleaning effect, where CBH 2 removes amorphous residues on top of a crystalline particle (see Figure 88 b & d).

EG 1 as an endo-glucanase did the same as proposed for CBH 2 by cleaning the surface of amorphous residues (see Figure 88 c).

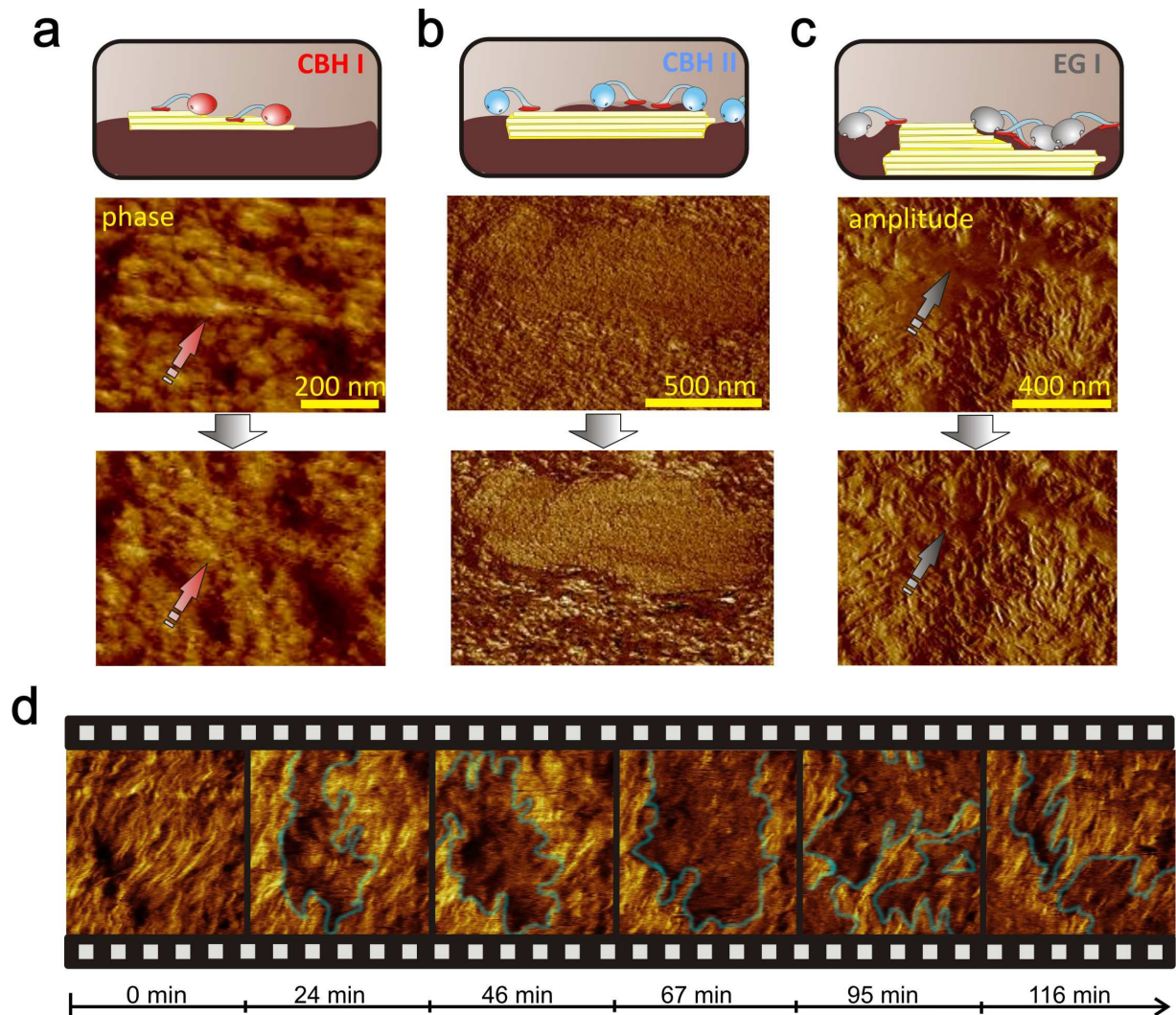


Figure 88: AMF investigations of single enzymes on the cellulose substrate. a: CBH 1 only hydrolyzed crystalline small fibers on the substrate without changing the surface around it. b: CBH 2 showed a cleaning effect where amorphous areas (dark) were removed after 4h from the top surface leaving behind crystalline small particles (bright). b: EG 1 removed amorphous material as indicated by gray arrows, thus resulting in a surface with more visible cellulose fibers. d: Phase image of the cleaning effect by CBH 2 on the nano-scale with clearly visible clouds in the phase image (blue envelope). The clouds were highly dynamic, vanishing almost completely after the cleaning (last picture).

In addition to this we also performed biochemical analysis, which correlated well with the AFM investigations (Figure 89). For the supernatant (Figure 89 a) a conversion of 80% is reached after 50 h, while no single enzyme component could compete with this value for the same timescale. CBH 1 (Figure 89 b) showed, as in the AFM experiment, little activity with saturation of about 13 % conversion after 80 h. CBH 2 (Figure 89 c) in the higher concentration showed activity with a still rising character after 80 h. EG 1 showed 55 % conversion after 50 h with saturation at about 60 % at 80 h. Comparing this with AFM data confirms our results with low CBH 1 activity and high CBH 2 activity, as well as medium activity of EG 1. The supernatant showed how remarkable the effect of synergism is during hydrolysis even when the concentration (0.18 mg /5 mg with 60% CBH 1 5-10 % CBH & EG 1 and EG 2 & EG 3 & beta-glucosidase as the rest) of the single enzymes in the solution is way below the single component experiments.

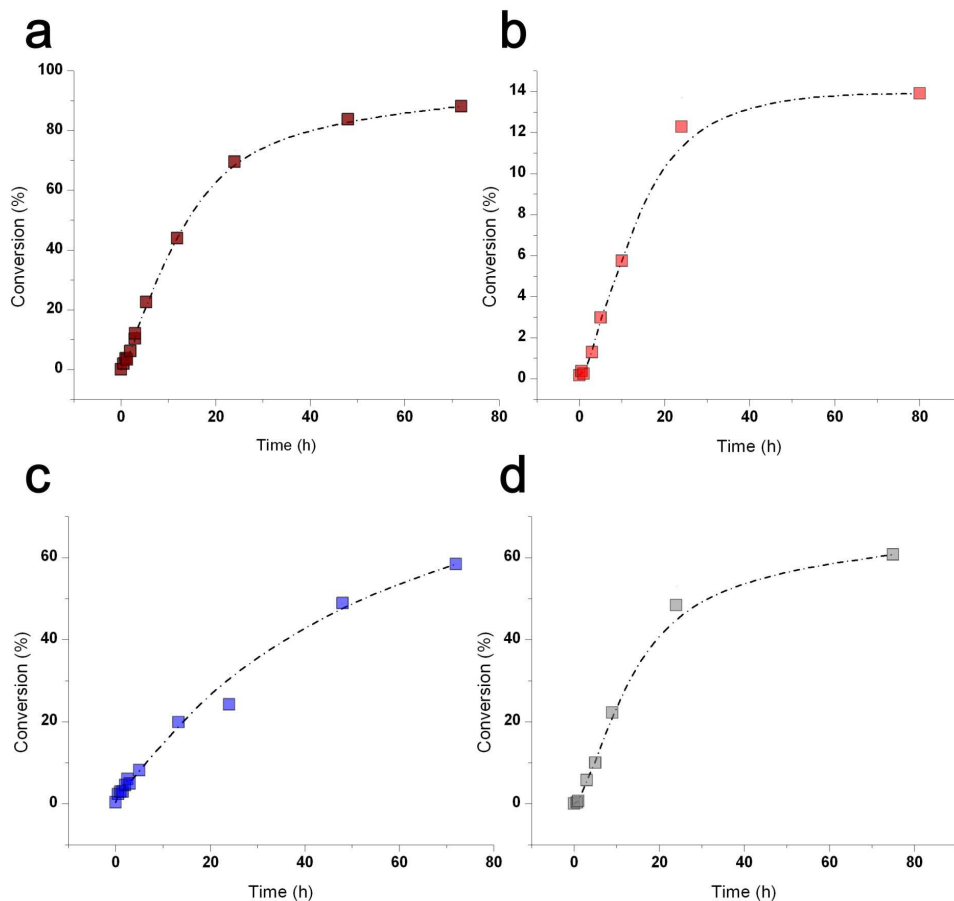


Figure 89: Biochemical analysis of a: supernatant b: CBH 1 c: CBH 2 d: EG 1.

Synergism or cooperative activity is a major component of a cellulase system, so the effect behind it has to be analyzed. We succeeded in separating the single components in respective experiments and showed which behavior certain enzymes display. Nevertheless, the precise mechanism is still not quite

clear. From now we can propose that the enzyme CBH 1 will be mostly active on crystalline cellulose as well as CBH 2, but with lower activity. So these two enzymes have the possibility to attack crystalline fibers. EG 1 and CBH 2 will also degrade amorphous cellulose, as we observed in the single component experiments, with CBH 2 showing higher affinity on amorphous cellulose as on crystalline cellulose. CBH 2 showed little activity on crystalline cellulose by small fiber shortening. This may be the same as proposed by Igarashi et. al. (2011) [27], where CBH 2 performs tip sharpening of crystalline fibers with low processive movement on the fiber. However, with these results as background we analyzed the supernatant experiment more precisely and found some interesting behavior as shown in Figure 90.

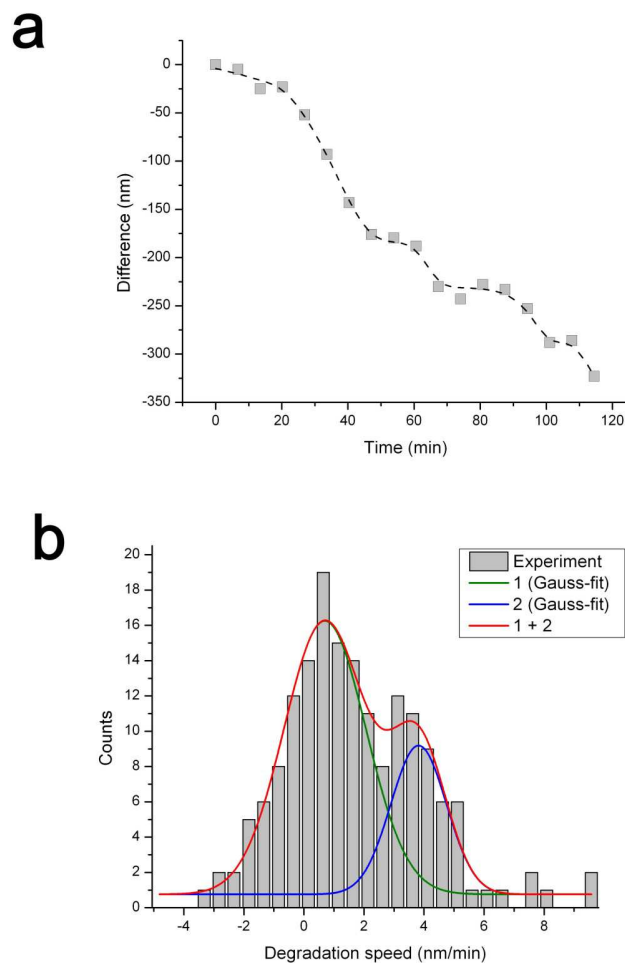


Figure 90: Statistical analysis of 10 points in a series of subsequent 18 pictures. a: A representative point showing two different degradation speeds. b: statistical analysis of all 180 points showing two velocities of degradation with $v_1 = 0.7 \pm 0.1$ nm/min and $v_2 = 3.8 \pm 0.2$ nm/min (see also Figure 61).

Figure 90 shows a representative point where the two velocities are clearly visible. Firstly we only saw a constant degradation rate of 300 nm / 4 h which corresponds to 1.25 nm/ min which can be elucidated

by the fact that v_1 seems so be more present (as seen in Figure 90 b). The peak of v_1 is about 2 times higher as the peak of v_2 . By weighting the velocity v_2 with the factor $\frac{1}{2}$ the arithmetic mean yields 1.3 nm / min, which is in good agreement of 1.25 nm / min. This is just a rough approximation but shows that the analysis seems to be correct. However, in our substrate the amorphous matrix is the major component, thus v_1 has to be associated to this type of cellulose and v_2 to crystalline cellulose. Normally amorphous cellulose should be degraded faster but this can be elucidated well with the fact that crystalline particles are very small. So CBH 1, 2 and EG 1 can work efficiently on these particles with CBH 1 degrading chains, while CBH 2 and EG 1 are producing new chain ends by endo-activity, thus accelerating CBH 1 degradation. The small size and thus big surface to volume ratio helps EG 1 to efficiently grab chains. The amorphous substrate is just attacked by EG 1 and CBH 2, thus synergism can only be present between these two components. This leads to the following degradation model: While small crystalline particles are degraded very fast by synergistic action between CBH 1, 2 and EG 1, amorphous areas are only attacked by EG 1 and CBH 2. This doesn't hold for big crystallites where EG 1 and CBH 2 cannot work as efficient, so big crystal hydrolysis by all enzymes should be slower. The model can be summed up in the following schematic (Figure 91).

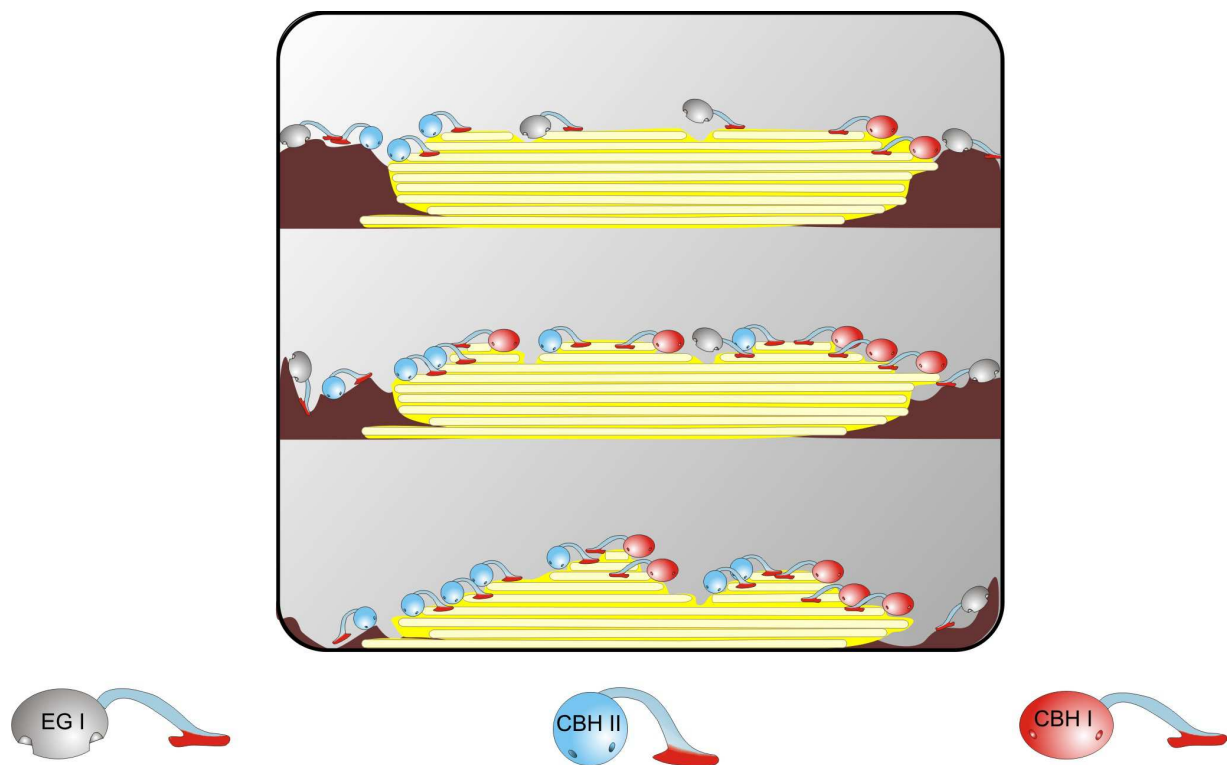


Figure 91: Schematic representation of our degradation model. The crystalline particle is yellow and the surrounding brown area is amorphous cellulose. This illustrates how a small crystalline particle is degraded by three enzymes.

Summing up the results leaves us with a new model on the molecular level for our substrate with new proposed mechanisms for small crystalline particles as well as new properties for the enzyme CBH 2.

Normally, one would only see what we observed first, the degradation of the surface with a speed of approximately 75 – 100 nm / h but by advanced nano-imaging in liquid, a more detailed image of this process is revealed. Two velocities could be identified, coming from different synergisms on different substrate parts. This leads to a new model on a close to nature substrate which will hopefully help in future applications to improve the technique of Second Generation biofuel fabrication.

9 Outlook

With a new model and interesting effects regarding special enzymes (CBH 2) cellulose degradation is still a field with many open questions. There is more work to do on synergistic effects like exo-endo or exo-exo synergism as well as on new or different substrates. Nevertheless, progress was remarkable in our work and we will continue to improve the experiments and our research.

Further improvements will be done in the substrate preparation to control the content of crystallinity as well as the crystal size. Visualization of single enzymes is another goal of future research as well as the ability to hold the sample at a controlled temperature. New enzymes and organisms are going to be investigated about their ability to degrade cellulose. All mentioned points are currently under progress by a collaboration of the FELMI and the Institute for Biotechnology and Bioprocess-Technology within the framework of a FWF Project.

With this approach we want to help to improve the technique of Second Generation biofuel fabrication. It is clear that these investigations are fundamental and not industry-based, but a precise understanding of all the processes involved during degradation can definitely help to find strategies to improve industrial biofuel fabrication.

10 List of Figures

Figure 2: Microfiber [7].	4
Figure 3: Scheme of the morphological architecture of a delignified wood fiber. W – wart layer; T – tertiary wall; S2-secondary wall (main body); S1 – secondary wall (winding layer); P – primary wall.	5
Figure 4: Left: Catalytic CBH 1 core in a side view, loaded with a cellulose chain (red) in the 50 Å long tunnel. Right: Schematic shape of the whole CBH 1 enzyme with the binding domain (A), linker region (B) and the CBD (C) [1].	7
Figure 5: Left: catalytic domain of CBH 2 in front view with tunnel, where the cellulose is transported and cleaved. Right: schematic shape of the whole enzyme with the binding domain (A), linker region (B) and CBD (C) [1].	7
Figure 6: Endo-glucanase 3 (EG 3) from <i>Trichoderma Reesei</i> . The enzyme is shown from the side and from below, which reveals clearly the grabbing trench.	8
Figure 7: Schematic representation of the hydrolysis of amorphous and microcrystalline cellulose [9].	8
Figure 9: The inverting mechanism of glycosidic hydrolysis.	9
Figure 11: Typical cantilever shapes. Triangular (top) and rectangular cantilever (bottom).	12
Figure 13: Principle of an AFM System: The laser is reflected at the tips backside into the four segment phototetector (PSD).	13
Figure 14: A: basic behavior of a piezoelectric material. B: tube scanner with the electrodes and the piezoelectric material. C: (x,y) Axis movement of the tube scanner. A contrary voltage is applied to the two electrode pairs.	14
Figure 15: The principle of contact mode AFM operation. The tip is scanned over the surface while the deflection of the cantilever is kept constant.	16
Figure 17: The assumption that the cantilever-tip shape can be simplified by a rectangular beam.	21
Figure 18: Amplitude resonance and phase shift diagram for a harmonic oscillator.	22
Figure 19: The weakly perturbed Harmonic Oscillator depending on the force regime.	23
Figure 21: Schematic of the cantilever deflection waveform in aqueous conditions.	25
Figure 22: The Ultramicrotome.	26
Figure 23: 3 Types of the diamond knives from left to right 35° knife with trench, 35° knife without a trench, 45° knife with trench and a glass knife.	26
Figure 25: Typically used sample holder. (1): fixation screw, (2): sample, (3): fixation rod for ultramicrotomy & measurement.	29
Figure 27: Fixation part for ultramicrotome use. Left: 3D drawing. (1) is the hole for stick holders, (2) is the drilling for the fixation screw. Right: after fabrication.	30
Figure 28: The Ultramicrotome with the special sample fixation tool for nano-flat preparation of the sample.	30
Figure 29: Right: Liquid Cell in 3D drawing. (1): Drilling for Injection system. (2): Drilling for Temperature sensor. Left: LC basin in its fabricated form with injection tube (red) and temperature sensor (black).	31
Figure 30: AFM Stage where the LC had to be mounted. Since the total height is too big for direct mounting an adapter for side mounting had to be constructed (see Figure 31).	32
Figure 31: The stage fixation (4) with the setup needed for cooling. (1) Separation plate between LC and Peltier element. (2) Peltier element. (3) Cooling body for as a heat sink.	32
Figure 33: Block diagram of the Controller circuit.	34
Figure 34: LC Amplifier with Weatson bridge.	35
Figure 35: The microcontroller unit with RS 232 port (Description of blocks is below).	36
Figure 36: HC amplifier with a high power n-MOS-FET.	37

List of Figures

Figure 37: Main routine.	39
Figure 39: The get temperature routine	40
Figure 40: GL between glass plates.	42
Figure 41: Dried cellulose fragments.	43
Figure 42: Results of the simultaneous thermal analysis. Left: Thermogravimetric analysis TGA. Right: Differential scanning calorimetry	44
Figure 43: Preparation procedure of the cellulose sample.	45
Figure 44: Cross-section of a typical sample. (1) Avicel residues which haven't been dissolved completely. (2) knife striations (knife is damaged and produces striations and scratches). (3) knife shatter (appearing on hard samples when the knife doesn't move smoothly).	45
Figure 45: AFM Image of a CS cross-section. The root mean square is about 15 nm excluding the crystalline Avicel residue (2). (1) Knife marks.	46
Figure 46: The probe holder for liquid applications. (1) The fixation and trench for the probe. (2) Fixation spring. (3) Electronic circuit and fixation contacts. (4) Glass window for the optical laser. The shiny red rectangle is the build in piezo for cantilever oscillation.	47
Figure 47: The scan head with the mounted liquid probe holder (right) and a schematic side view (left).	48
Figure 48: Glass surface of a standard petrie dish under a droplet of liquid.	49
Figure 49: Phase image of the glass surface with a slightly increasing phase signal from top to bottom.	49
Figure 50: Sections from a standard sample. Slight differences are due to solvent residues and the different measuring positions.	50
Figure 51: Standard sample in dry (right) and fluid (left) conditions. The height image is colored with phase information.	51
Figure 52: The substrate in 3D and the corresponding phase image. The blue arrow and blue border indicates the crystalline residue. It is clearly visible in the phase image (inset).	54
Figure 53: The results of the degradation process over a time of 4 hours with the supernatant of the fungus <i>Trichoderma Reesei</i> .	55
Figure 54: Chapter profiles after certain incubation time. It shows that after about 4 hours 300-400 nm substrate is degraded by the enzymes.	56
Figure 55: Biochemical hydrolysis experiment with the supernatant on the cellulose substrate. The supernatant is refereed as mg 2279.	57
Figure 56: RMS evolution. Hydrolysis seems to start at about 1 hour after incubation rising constantly. Deep trenches and holes are formed during this period as a result of different degradation velocities. The error was estimated with 10% coming from drift problems and flattening errors.	57
Figure 57: 3D Image of the substrate surface with clearly resolved microfibrils. The picture is colored with amplitude information to enhance contrast.	58
Figure 58: Picture series over about 45 min of degradation. Clearly visible are two microfibrillar structures which first appear and vanish after some time again.	59
Figure 59: Chapter over two arbitrary chosen microfibrils. Fiber 2 has a height offset for better visualization.	59
Figure 60: Depth evolution of two points on the substrate.	60
Figure 61: Statistical analysis of degradation rates per minute. Two distinct velocities are visible and fit results give $v_1 = 0.7 \pm 0.1$ nm/min and $v_2 = 3.8 \pm 0.2$ nm/min with a fit quality of $R^2 = 96\%$.	60
Figure 62: CBH1 activity on cellulose substrate for 4 hours.	61

List of Figures

Figure 64: A magnified image from Figure 63 where the fiber is clearly visible indicated by the blue arrow. _____	62
Figure 65: Biochemically determined CBH1 hydrolysis at 50 °C. _____	63
Figure 66: Height image at 500 nm scan range after incubation. _____	64
Figure 67: The measurement site with the crystalline residue (blue). _____	65
Figure 68: The results of the degradation process over a time of 5 hours with the enzyme CBH 2 of <i>Trichoderma Reesei</i> . _____	66
Figure 70: RMS evolution for CBH 2 exposure for more than 5 h. _____	67
Figure 72: Crystalline residue (blue) and reference picture for the high resolution imaging. Yellow rectangle is the measurement spot with 1 μ m size. _____	69
Figure 73: Cleaning effect of the enzyme CBH 2 on our multiphase substrate. In the left lower corner a crystalline residue is present. _____	70
Figure 74: 3D image of the measured surface the crystalline residue is visible in the left lower corner (little bit brighter). The red arrows mark darker clouds on the surface and blue is the section (left). You can see also the section profile with the angle α which is in this case 10°. (The angle looks bigger because of units!). _____	70
Figure 75: (1) narrow hole and broad hole (2). The force field is blue. In case of (1) predictions about enzymes being at work at the surface would be difficult. In case (2) no problems due to increased force fields occur. _____	71
Figure 76: Phase images taken from the crystalline residue. The images go from left to right. These images show a dark cloud reshaping and moving during the measurement which is possibly an enzyme cluster. _____	71
Figure 78: The results of the degradation process over a time of 6 1/2 hours with the enzyme EG 1 of <i>Trichoderma Reesei</i> . _____	73
Figure 79: RMS evolution over incubation time. The error is estimated with 20%, coming from a small image area and x-y drift. _____	74
Figure 80: EG 1 hydrolysis at 50 °C. _____	75
Figure 81: Looking at a smaller timescale from Figure 80. For the first hour conversion is low. _____	75
Figure 82: Reference image of the substrate for the synergy experiment. Blue is the crystalline residue with mostly parallel fibers indicating that the residue is lying parallel to the surface. Yellow rectangles indicate the measurement areas where the area below is for the EG 1 measurement and above for EG 1 + CBH2 and + CBH 1. _____	77
Figure 83: Surface topographies during our synergism experiment. Since it is difficult to see any changes during the EG 1 period a magnified image is shown in Figure 84. _____	78
Figure 84: Magnified view of the first hour EG 1 incubation. Blue arrows indicate interesting regions. There we believe amorphous materials (darker smother areas) are present which are missing after 1 hour of incubation. This shows the affinity of this enzyme for amorphous cellulose. _____	79
Figure 85: EG 1 + CBH 2 on the substrate. Images are in Phase mode and bright areas are crystalline cellulose fibers. It shows clearly the increase of large crystalline areas whereas small one vanishes. _____	80
Figure 86: Movie sequence of cellulose degradation by <i>Trichoderma Reesei</i> supernatant over 4 h. In the left upper corner a crystalline Avicel residue is present. _____	81
Figure 87: Hydrolysis on the nano-scale by the enzyme system of <i>Trichoderma Reesei</i> . Fibers are clearly visible and scale bar is 100nm. The fibers appear and vanish again after degradation. _____	82
Figure 88: AMF investigations of single enzymes on the cellulose substrate. a: CBH 1 only hydrolyzed crystalline small fibers on the substrate without changing the surface around it. b: CBH 2 showed a cleaning effect where amorphous areas (dark) were removed after 4h from the top surface leaving behind crystalline small particles (bright). b: EG 1 removed amorphous material as indicated by gray arrows, thus resulting in a surface with more	

List of Figures

<i>visible cellulose fibers. d: Phase image of the cleaning effect by CBH 2 on the nano-scale with clearly visible clouds in the phase image (blue envelope). The clouds were highly dynamic, vanishing almost completely after the cleaning (last picture).</i>	83
<i>Figure 89: Biochemical analysis of a: supernatant b: CBH 1 c: CBH 2 d: EG 1.</i>	84
<i>Figure 90: Statistical analysis of 10 points in a series of subsequent 18 pictures. a: A representative point showing two different degradation speeds. b: statistical analysis of all 180 points showing two velocities of degradation with $v_1 = 0.7 \pm 0.1$ nm/min and $v_2 = 3.8 \pm 0.2$ nm/min (see also Figure 61).</i>	85
<i>Figure 91: Schematic representation of our degradation model. The crystalline particle is yellow and the surrounding brown area is amorphous cellulose. This illustrates how a small crystalline particle is degraded by three enzymes.</i>	86
<i>Figure 92: Sample holder in its final form with stage fixation as well as cooling body.</i>	96
<i>Figure 93: New sample holder with sample and liquid cell (1), water cooling box (2), peltier cooling stage (3) as well as the stage fixation (4).</i>	96

11 Bibliography

- [1] M. K. Bath and S. Bhat, "Cellulose degrading enzymes and their potential industrial applications," *Biotechnology Advances*, pp. 583-620, 1997.
- [2] S.-Y. Ding and et.al., "A biophysical perspective on the cellulosome: new opportunities for biomass conversion," *Current Opinion in Biotechnology*, pp. 218-227, 2008.
- [3] J. Dohr, Enzymatic degradation of superfalt cellulose substrates, Graz, 2011.
- [4] D. Klemm, H. P. Schmauder and T. Heinze, "Cellulose," *Biopolymers Online*, pp. 275-287, 2005.
- [5] J.-L. Wertz, O. Bédué and J. P. Mercier, Cellulose Science and Technology, Lausanne, Switzerland: EPFL Press, 2010.
- [6] I. Lee, B. Evans and J. Woodward, "The mechanism of cellulase action on cotton fibers: evidence from atomic force microscopy," *Ultramicroscopy*, pp. 213-281, 1999.
- [7] Genomics, "Systems Biology for Energy and Environment," *GTL Roadmap*, August 2005.
- [8] V. Kocherbitov and et.al., "Hydration of Microcrystalline Cellulose and Milled Cellulose Studied by Sorption Calorimetry," *The Journal of Physical Chemistry*, p. 3728–3734, 2008.
- [9] L. R. Lynd and et.al., "Microbial Cellulose Utilization: Fundamentals and Biotechnology," *Mircobiology and Molecular Biology Reviews*, pp. 506-577, 2002.
- [10] S. Hunklinger, Festkörperphysik, München: Oldenbourg Wissenschaftsverlag GmbH, 2007.
- [11] E. Riedel and C. Janiak, Anorganische Chemie, Berlin: Walter de Gruyter GmbH & Co. Kg, 2011.
- [12] "Wikipedia," 1 September 2011. [Online]. Available: http://de.wikipedia.org/w/index.php?title=Chemische_Bindung&oldid=93118199. [Accessed 13 September 2011].
- [13] S. Zhu and et.al., "Dissolution of cellulose with ionic liquids and its application: a mini review," *Green Chemistry*, pp. 325-327, 2006.
- [14] R. P. Swatloski and et.al., "Dissolution of Cellulose with ionic liquids," *JACS Communications*, pp. 4974-4975, 2004.

- [15] R. Garcia, *Amplitude Modulation Atomic Force Microscopy*, Weinheim: Wiley-VCH GmbH & Co. KGaA, 2010.
- [16] G. Binnig, C. Quate and C. Gerber, "Atomic Force Microscopy," *Phys. Rev. Lett.* 56, p. 930–933, 1986.
- [17] G. Fantner and et.al., "Use of self-actuating and self-sensing cantilevers for imaging biological samples in fluid," *Nanotechnology* 20 (43), 2009.
- [18] N. B. Matsko and et.al., "Self-Sensing and -Actuating Probes for Tapping Mode AFM Measurements of Soft Polymers at a Wide Range of Temperatures," *Journal of Modern Physics* 2, pp. 72-78, 2011.
- [19] D. Müller and et.al., "Electrostatically balanced subnanometer imaging of biological specimens by atomic force microscope," *Biophys. J.*, pp. 1101-1111, 1999.
- [20] T. Uchiasi and et.al., "Quantitative measurement of solvation shells using frequency modulated atomic force microscopy," *Nanotechnology*, p. S49, 2005.
- [21] Y. Wu, C. Gupta and M. Shannon, "Effect of solution concentration, surface bias and protonation on the dynamic response of amplitude modulated atomic force microscopy in water," *Langmuir*, p. 10817–10824, 2008.
- [22] P. Bubner and et.al., "Cellulases dig deep," *JBC*, 2011.
- [23] "Regelungstechnik," [Online]. Available: <http://www.rn-wissen.de/index.php/Regelungstechnik>. [Accessed 30 August 2011].
- [24] J.-i. Kadokawa, M.-a. Murakami and Y. Kaneko, "A facile preparation of gel materials from a solution of cellulose and ionic liquid," *ScienceDirect*, pp. 769-772, 2008.
- [25] K. Prasad, Y. Kaneko and J.-i. Kadokawa, "Novel Gelling Systems of kappa-,iota- and lambda-carrageenans and their Composite Gels with Cellulose Using Ionic Liquid," *Macromolecular Bioscience*, pp. 367-382, 2008.
- [26] G. Mantanis, R. Young and R. Rowell, "Swelling of compressed cellulose fiber webs in organic liquids," *cellulose*, pp. 1-22, 1995.
- [27] K. Igarashi and et.al., "Traffic Jams Reduce Hydrolytic Efficiency of Cellulase on Cellulose Surface," *Science*, pp. 1279-1282, 2011.

- [28] H. Chanzy and et.al., "The action of 1,4-beta-D-glucan cellobiohydrolase on Valonia cellulose microcrystals," *FEBS Letters* 153(1), pp. 113-118, 1982.
- [29] H. Chanzy, H. B. and R. Vuong, "Colloidal gold labelling of 1,4-beta-D-glucan cellobiohydrolase adsorbed on cellulose substrates," *FEBS letters* 172(2), pp. 193-197, 1984.
- [30] A. N. Rafael and et.al., "Visualization of Trichoderma reesei Cellobiohydrolase 1 and Endoglucanase 1 on Aspen Cellulose by Using Monoclonal Antibody-Colloidal Gold Conjugates," *Applied and Environmental Microbiology* 57(11), pp. 3163-3170, 1991.
- [31] G. Binnig, H. Rohrer and C. Gerber, "Surface Studies by scanning tunneling microscopy," *Physical Review Letters* 49, p. 57-61, 1982.
- [32] G. Binnig, C. F. Quate and C. Gerber, "Atomic force microscope," *Physical Review Letters* , p. 930-933, 1986.
- [33] S. Elazzouzi-Hafraoui and et.al, "The Shape and Size Distribution of Crystalline Nanoparticles Prepared by Acid Hydrolysis of Native Cellulose," *Biomarcomolecules*, pp. 57-65, 2008.
- [34] C. C. Geddes, I. U. Nieves and L. O. Ingram, "Advances in ethanol production," *Current Opinion in Biotechnology*, pp. 312-319, 2011.
- [35] G. I. Mantanis, R. A. Young and R. M. Rowell, "Swelling of compressed cellulose fiber webs in organic liquids," *Cellulose*, pp. 1-22, 1995.
- [36] A. Qirk and et.al., "Direct Visualization of the Enzymatic Digestion of a Single Fiber of Native Cellulose in an Aqueous Environment by Atomic Force Microscopy," *Langmuir*, pp. 5007-5013, 2010.
- [37] X. Chen, "Optimizing phase imaging via dynamic force curves," *Surface Science*, pp. 292-300, 2000.
- [38] A. S. P. Ricard Garcia, "Attractive and repulsive tip-sample interaction regimes in tapping mode atomic force microscopy," *Physical Review B*, pp. 4961-4967, 1999.
- [39] K. Igarashi, "High-Speed Atomic Force Microscopy Visualizes Processive Movement of Trichoderma Reesei Cellobiohydrolase 1 on crystalline cellulose," *jsc The Journal of Biological Chemistry*, pp. 36186-36190, 2009.
- [40] Y. Seo and W. Jhe, "Atomic force microscopy and spectroscopy," *Reports on Progress in Physics* , p. 22, 2007.

- [41] J. Loos, "The Art of SPM: Scanning Probe Microscopy in Material Science," *Advanced Materials*, pp. 1821-1833, 2005.
- [42] S. Magonov, V. Elings and M.-H. Whangbo, "Phase imaging and stiffness in tapping-mode atomic force microscopy," *Surface Science*, pp. L385-L391, 1996.
- [43] S. E. Levine and et.al, "A Mechanistic Model of the Enzymatic Hydrolysis of Cellulose," *Biotechnology and Bioengineering*, pp. 37-51, 2010.
- [44] D. P. Allison and et.al., "Atomic force microscopy of biological samples," *Advanced Review*, pp. 618-634, 2010.

I. Appendix A

In this section all drawings of the mechanical design are added. For further informations please contact: Thomas Ganner, Felmi-ZFE, Steyrergasse 17, 8010 Graz or thomas.ganner@felmi-zfe.at

Complete sample holder:

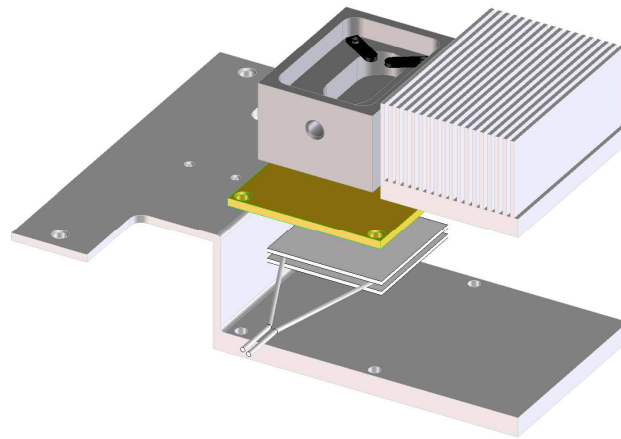


Figure 92: Sample holder in its final form with stage fixation as well as cooling body.

As a result of extensive testing of the design from Figure 92 a new design had to be made, since the stage fixation acts like a tuning fork inducing vibrations in the AFM which prevents high resolution imaging. Hence, this design is added to the appendix, although it is not part of this thesis. This design is will be used in the following doctor thesis in a FWF Projekt (Grant P 24156-B21).

New design:

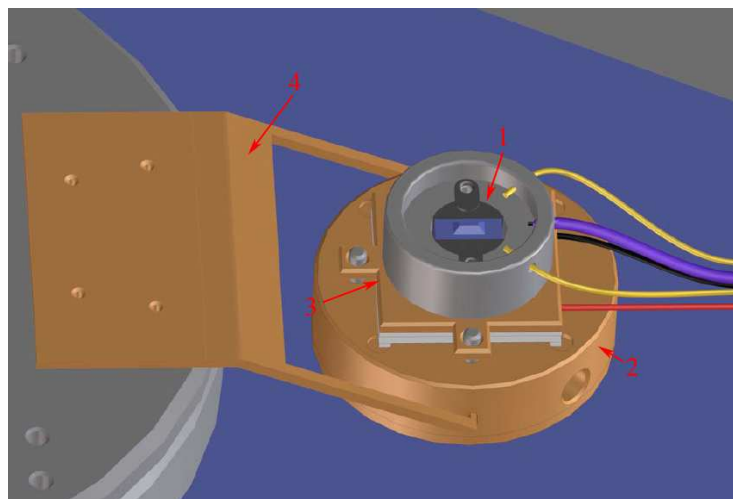
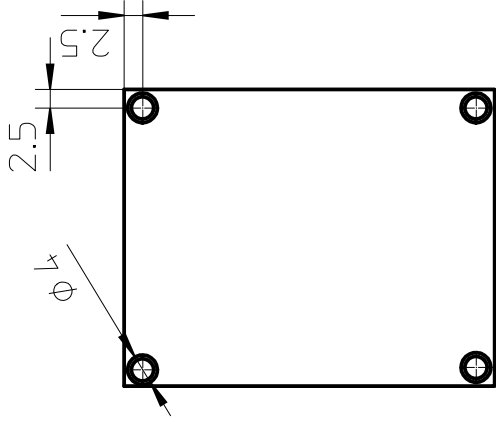
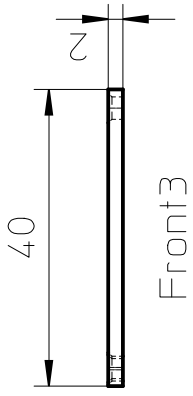
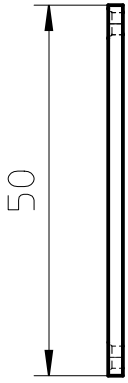


Figure 93: New sample holder with sample and liquid cell (1), water cooling box (2), peltier cooling stage (3) as well as the stage fixation (4).



USE RANGE	TOLERANCE	SURFACE	ARCHIVE	SCALE
			MATERIAL: Messing	1:1
			DESCRIPTION: Separation plate to peltier element	
	DRAWN	DATE	DRAWING-NUMBER	
	APPR.	25/5/2012	1	
	RLS.	T. G.	DRAWING-NUMBER	
			1	
			DRAWING-NUMBER	
			1	
INDEX	DESCRIPTION	DATE	NAME	ORIGINAL
				I.EXCH.F.
				I.EXCH.TH.
				SHEET
				2
				OF 2

